universität
wien

DISSERTATION / DOCTORAL THESIS

Titel der Dissertation /Title of the Doctoral Thesis

„Ultrafast Intersystem Crossing Dynamics In Organic Molecules“

verfasst von / submitted by

Jan Patrick Zobel, MSc

angestrebter akademischer Grad / in partial fulfilment of the requirements for the degree of

Doktor der Naturwissenschaften (Dr. rer. nat.)

Wien, 2018 / Vienna 2018

Studienkennzahl lt. Studienblatt / degree programme code as it appears on the student record sheet:	A 796 605 419
Dissertationsgebiet lt. Studienblatt / field of study as it appears on the student record sheet:	Chemie
Betreut von / Supervisor:	Univ.-Prof. Dr. Leticia González

Abstract

Ultrafast intersystem crossing in organic molecules is an intriguing phenomenon. Its experimental observation contradicts the long-hold belief that intersystem crossing can occur on an ultrafast time scale solely through large spin-orbit couplings of the size only found in the presence of heavy atoms such as metal complexes. Ultrafast intersystem crossing is the key to the efficient population of electronic triplet states for certain molecules such as nitro polycyclic aromatic hydrocarbons, where it unlocks the phototoxic potential in these widespread environmental pollutants. Thus, the photodynamics of three nitronaphthalene derivatives, i.e., 2-nitronaphthalene, 1-nitronaphthalene, and 2-methyl-1-nitronaphthalene, were investigated in this work using the SHARC method in order to gain insights on the ultrafast nature of their intersystem crossing. In these molecules, intersystem crossing proceeds mainly via two electronic pathways. The electronic transition in the most important pathway can be described simply by a single-electron $\pi \rightarrow n$ transition corresponding to a small charge redistribution which is completely localized at the nitro group. Due to this localization, the $\pi \rightarrow n$ transition will be influenced only weakly by the aromatic ring system so that the corresponding intersystem crossing channel can be a common feature that is present also in the excited-state dynamics of other nitro aromatic compounds, which may explain the ultrafast character of intersystem crossing observed in these compounds.

Further work of this thesis comprised two additional topics related to the study of excited states of organic molecules in general. One dealt with vibrational sampling of molecular conformations and its effects on the description of and dynamics in electronically excited states of nitroaromatic molecules. For nitrobenzene, it was found that neglecting vibrational sampling leads to an erroneous interpretation of its absorption spectrum. For 2-nitronaphthalene, the performance of different common vibrational sampling approaches, i.e., zero-temperature Wigner sampling or thermal molecular-dynamics-based sampling, was evaluated. Neither of these approaches provides the correct energy which molecules possesses under experimental conditions. The correct energy can be accounted for by simply extending the Wigner sampling to the finite-temperature formalism. In the excited-state dynamics simulations, using initial conditions from different vibrational sampling approaches had a significant effect on the reaction rates and contributions from the different intersystem crossing channels, thus, highlighting the importance of appropriate vibrational sampling. Finally, the performance of the CASPT2 method in the description of the excited states of organic molecules was investigated. The CASPT2 method is frequently applied in its IPEA-modified version, however, extended benchmark calculations could demonstrate that at least for excited states of organic molecules this modification deteriorates the performance of CASPT2 and should be abandoned.

Zusammenfassung

Ultraschnelle Interkombination in organischen Molekülen ist ein faszinierendes Phänomen. Ihre experiementelle Beobachtung steht der lange vertretenen Überzeugung entgegen, dass Interkombination nur mit Spin-Bahn-Kopplungen von einer Größenordnung, die nur in der Gegenwart von schweren Atomen, z.B. in Metallkomplexen, gefunden werden, auf dieser ultraschnellen Zeitskala möglich ist. Ultraschnelle Interkombination ist der Schlüssel zur effizienten Besetzung elektronischer Triplettzustände in bestimmten Molekülen wie etwa den polyzyklischen nitroaromatischen Kohlenwasserstoffen, was das phototoxische Potenzial dieser weit verbreiteten Umweltschadstoffe verwirklicht. Aus diesem Grund wurden die Photodynamiken der drei Nitronaphthalin-Derivate 2-Nitronaphthalin, 1-Nitronaphthalin und 2-Methyl-1-Nitronaphthalin in dieser Arbeit mit Hilfe der SHARC-Methode untersucht, um Einblicke in die ultraschnelle Natur ihrer Interkombination zu erlangen. In den untersuchten Molekülen findet Interkombination hauptsächlich in zwei Kanälen statt, wobei die elektronischen Übergänge im wichtigsten Kanal einfach durch einen Einelektronen-$\pi \rightarrow n$-Übergang beschrieben werden können, der einer Ladungsumverteilung entspricht, die vollständig in der Nitrogruppe der Moleküle lokalisiert ist. Aufgrund dieser Lokalisierung ist der $\pi \rightarrow n$-Übergang weitgehend unabhängig vom Rest des aromatischen Ringsystems. Daher ist es möglich, dass auch die Dynamiken angeregter Zustände der anderen Nitro-Verbindungen diesen Interkombinations-Kanal aufweisen können, was das Auftreten der ultraschnellen Interkombination in diesen Verbindungen erklären kann.

Die weiteren Arbeiten dieser Dissertation beschäftigen sich mit zwei der Studie von angeregten Zuständen organischer Moleküle verwandten Themen. Einer dieser Teile betrachtet das schwingungsbasierte Sampling von Molekülkonformationen und dessen Einfluss auf die Beschreibung von und die Dynamik in elektronisch angeregten Zuständen. So wurde herausgefunden, dass die Interpretation des Absorptionsspektrums von Nitrobenzol fehlerhaft ist, wenn kein schwingungsbasiertes Sampling verwendet wird. Für 2-Nitronaphthalin wurde das Verhalten von den gebräuchlichen schwingungsbasierten Null-Temperatur-Wigner-Sampling und thermischem Sampling basierend auf Moleküldynamiken untersucht. Keine dieser Method beschreibt die Energie, die Moleküle unter experimentellen Bedingungen besitzen, korrekt. Dieses Verhalten kann jedoch einfach erzielt werden, wenn das Wigner-Sampling auf endliche Temperaturen erweitert wird. Für die Verwendung von Anfangsbedingungen in Dynamiksimulation angeregter Zustände aus verschiedenen schwingungsbasierten Sampling-Methoden wurde ein beträchtlicher Effekt auf die Reaktionsgeschwindigkeiten und die Beiträge der verschiedenen Interkombinations-Kanälen festgestellt, was die Bedeutung, eine angemessene Sampling-Methode zu benutzen, hervorhebt. Im letzten Teil dieser Dissertation wurde der Verhalten der CASPT2-Methode bei der Beschreibung von angeregten Zuständen von organischen Molekülen untersucht. Die CASPT2-Methode wird oft in ihrer IPEA-modifizierten Variante benutzt. Es konnte jedoch durch umfassenden Vergleichsrechnungen gezeigt werden, dass diese Modifikation zumindest für angeregete Zustände von organischen Molekülen zu schlechteren Ergebnissen führt und daher aufgegeben werden sollte.

Frequently Used Acronyms

1NN	1-nitronaphthalene
2NN	2-nitronaphthalene
2M1NN	2-methyl-1-nitronaphthalene
AIMD	ab initio molecular dynamics
BOA	Born-Oppenheimer approximation
CASPT2	complete-active-space second order perturbation theory
CASSCF	complete-active-space self-consistent field
CI	conical intersection
COSMO	conductor-like screening model
CT	charge-transfer
DE	delocalized-excitation
DFT	density-functional theory
F	fluorescence
FC	Franck-Condon
FCI	full configuration interaction
HF	Hartree-Fock
IC	internal conversion
IPEA	ionization-potential electron-affinity
ISC	intersystem crossing
KS	Kohn-Sham
LE	localized-excitation
MCH	molecular Coulomb Hamiltonian
MD	molecular dynamics
MeCN	acetonitrile

MeOH	methanol
MM	molecular mechanics
MSEE	mean signed error of excitation energies
MSET	meas signed error of total energies
MUEE	mean unsigned error of excitation energies
NAC	non-adiabatic couplings
NMA	normal-mode analysis
NN	nitronaphthalene
NPAH	nitro polycyclic aromatic hydrocarbons
NTO	natural-transition orbitals
P	phosphorescence
PCM	polarizable continuum model
PES	potential-energy surface
QM	quantum mechanics
QM/MM	quantum mechanics/molecular mechanics
RMSD	root-mean-square displacement
SHARC	surface hopping including arbitrary couplings
s-MM/QM	sequential molecular mechanics/quantum mechanics
SOC	spin-orbit coupling
TDA	Tamm-Dancoff approximation
TDDFT	time-dependent density-functional theory
UV	ultra-violet
ZPE	zero-point energy

Contents

1 Introduction 1

1.1 The Ultrafast Intersystem Crossing Controversy 1
1.2 Nitro Polycyclic Aromatic Hydrocarbons 2
1.3 Understanding Excited-State Dynamics 3
1.4 The Challenges Tackled in This Work 4

2 Theory, Methods, and Approximations 5

2.1 The Schrödinger Equation 5
2.2 The Born-Oppenheimer Approximation 6
2.3 Electronic Structure Theory 7
  2.3.1 The Hartree-Fock Approximation 7
  2.3.2 Multi-Configurational Methods 9
  2.3.3 Density-Functional Theory 12
  2.3.4 Time-Dependent Density-Functional Theory 14
  2.3.5 Transition-Density Matrix Description of Excited States . 15
  2.3.6 Spin and Spin-Orbit Coupling 17
  2.3.7 Molecules in Solution 18
2.4 Transitions Between Electronic States 19
  2.4.1 Absorption and Transition-Dipole Moments 19
  2.4.2 Radiative and Nonradiative Relaxation Pathways 21
2.5 Nuclear Motion 22
  2.5.1 Surface Hopping 22
  2.5.2 Prerequisites for Surface Hopping Studies 25

3 Vibrational Sampling 26

3.1 The Effects of Vibrational Sampling on Excited States 26
  3.1.1 The Character of the Excited States of Nitrobenzene . . . 26
  3.1.2 Quenching of Charge Transfer by Vibrational Motion . . 28
3.2 Quantum and Classical Phase-Space Sampling 32
3.3 Performance of Different Sampling Models 34
  3.3.1 The Absorption Spectrum of 2-Nitronaphthalene 34
  3.3.2 Influence of Vibrational Motion 36
  3.3.3 Influence of the Solvent Model 40
3.4 Including Temperature in Quantum Phase-Space Sampling . . . 42
  3.4.1 Finite-Temperature Wigner Phase-Space Sampling 42
  3.4.2 Zero-Point Energy and Thermal-Energy Contributions . . 44
3.5 Conclusions on Vibrational Sampling 48

4 The CASPT2 Method and Excited States of Organic Molecules 50

4.1 The Study of Nitrobenzene and 2-Nitronaphthalene 50

4.2 The IPEA Dilemma in CASPT2 53
4.2.1 Introduction of the IPEA Shift 53
4.2.2 Literature Survey of CASPT2 Excitation Energies 55
4.2.3 FCI-CASPT2 Benchmark Study of Small Molecules . . . 58
4.2.4 CASPT2 Benchmark of Thiel's Set of Organic Molecules . 60
4.3 Conclusions on the IPEA Shift in CASPT2 64

5 Excited-State Dynamics Simulations of Nitronaphthalene Derivatives 66
5.1 Previous Studies on Nitronaphthalene Derivatives 66
5.2 The Mechanism of Ultrafast ISC in 2-Nitronaphthalene 68
5.2.1 Excited-State Relaxation Mechanism 68
5.2.2 Electronic Structure in the ISC Pathways 72
5.2.3 Nuclear Motion Towards ISC 73
5.3 Effects of Different Initial Conditions 75
5.3.1 Absorption Spectra and Initially Excited States 76
5.3.2 Excited-State Dynamics 78
5.3.3 Intersystem Crossing Pathways 78
5.4 Studies of 1NN and 2M1NN 80
5.4.1 Absorption Spectra and Initially Excited States 80
5.4.2 Excited-State Dynamics 80
5.4.3 Intersystem Crossing Pathways 83
5.5 Conclusions from the Dynamics Simulations 85

6 Summary 86

Bibliography 88

List of Publications 109

Acknowledgments 110

Curriculum Vitae 112

1 Introduction

1.1 The Ultrafast Intersystem Crossing Controversy

When a molecule absorbs ultraviolet (UV) or visible light, it is usually transferred into an excited electronic state. Through this absorption, the molecule receives additional energy, making the excited electronic state unstable, and it is forced to leave the excited state to return to the stable electronic ground state again. To achieve this, it can emit light through stochastic processes, but at the same time the molecule also moves in the potential of the electronically excited states. While moving, the molecule can visit different electronic states which can lead it back to the electronic ground state. These dynamical relaxation processes, involving the motion of the nuclei of the molecule, compete with the process of light emission. The winner of this competition is decided simply by which process is faster, but the rate at which either process occurs depends intimately on the electronic structure of the molecule itself as well as the energy of the absorbed light. Using ultrafast time-resolved spectroscopy techniques, it was observed that the dynamical electronic relaxation processes can occur on the (ultrafast) time scale of femtoseconds which is as fast as the nuclear motion of the molecule itself.

In organic molecules, the ultrafast relaxation dynamics observed usually connect only electronic states of the same spin multiplicity through a process called internal conversion (IC). Over time, however, a growing number of organic molecules was reported that exhibited a different relaxation process at the same ultrafast time scale as IC. This process, called intersystem crossing (ISC), connects electronic states of different spin multiplicity. ISC can occur when the states of different spin multiplicits experience so-called spin-orbit coupling (SOC), which is a relativistic effect that scales with the charge Z of the nuclei of the molecule. Accordingly, molecules with heavy atoms carrying large nuclear charges Z such as metal complexes exhibit large SOCs and ISC can proceed effectively on a femtosecond time scale. Contrary, for organic molecules composed solely of light nuclei, i.e., nuclei with small Z, SOCs are small and ISC was assumed to be slow. This made the observation of ultrafast ISC in organic molecules very unexpected and difficult to rationalize.

An illustrative example of unexpectedly ultrafast ISC is given by a study from 1986 of Warren and Bernstein that represented one of the first examples indicating that ISC indeed can take place on a femtosecond timescale in organic molecules.[1] The authors investigated the excited-state dynamics of jet-cooled acetophenone starting in the S_2 electronic state, and found that the relaxation dynamics from the S_2 state occurred with a time constant of $\tau = 260$ fs. After ruling out IC, the unfortunate Warren and Bernstein were "forced to conclude, with trepidation," that the ultrafast decay represented ISC to a triplet

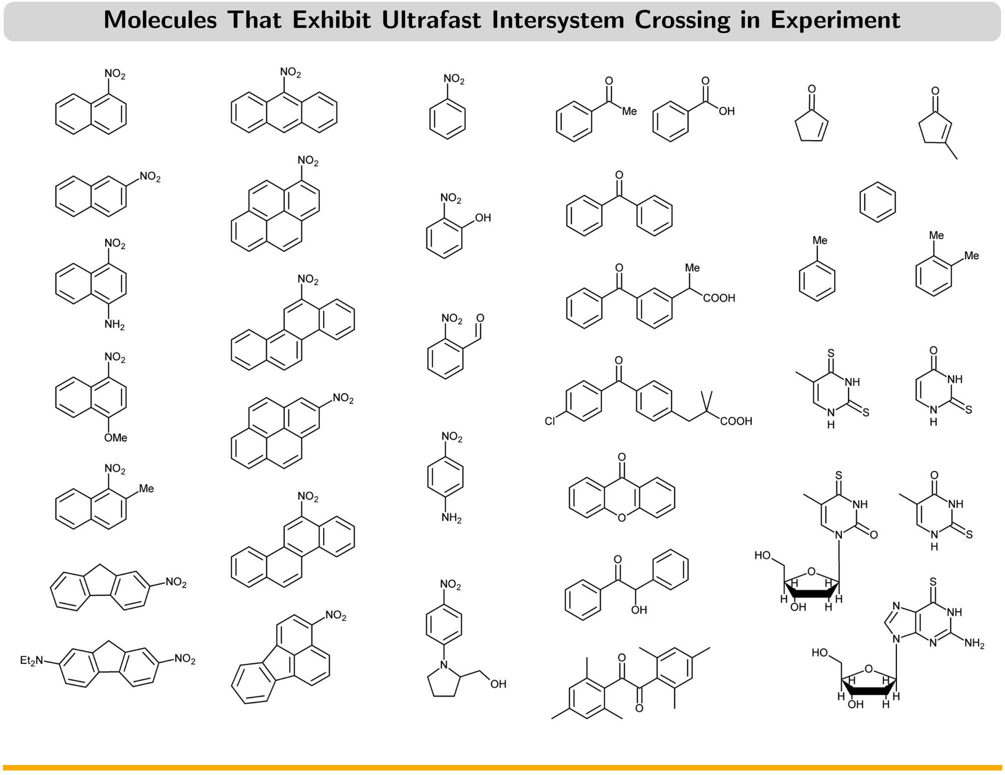
Molecules That Exhibit Ultrafast Intersystem Crossing in Experiment

Figure 1.1: Molecules that exhibit ultrafast intersystem crossing in experiment.

state. Nowadays, however, a considerable number of organic molecules are known to exhibit ultrafast ISC. These molecules comprise aromatic nitro compounds,[2–27]aromatic carbonyl compounds,[1,28–46] and few simple aromatic hydrocarbons such toluene[47], xylene[47,48], and possibly benzene.[49–51] Additionally, ultrafast ISC has been observed, e.g., in a number of thiosubstituted nucleobases.[52–58] However, for these molecules ultrafast ISC has been attributed to the presence of the sulfur as a heavy atom, inducing large SOCs.[59–61]

1.2 Nitro Polycyclic Aromatic Hydrocarbons

The increasing number of organic molecules where ultrafast ISC has been observed (see Figure 1.1) raises the question whether ultrafast ISC may be a commonly overlooked phenomenon in certain classes of organic molecules. Thus, this work set out to study excited-state dynamics of one the these classes, the aromatic nitro compounds, in order to understand the factors that make ultrafast ISC possible in organic molecules. These aromatic nitro compounds comprise nitro polycyclic aromatic hydrocarbons (NPAHs) and nitrobenzene derivatives, and the choice to study this class of compounds was motivated by the biological relevance of NPAHs.

NPAHs are widespread environmental pollutants that are suspected to induce carcinogenesis and mutagenesis.[62,63] For example, dermal exposure to NPAHs

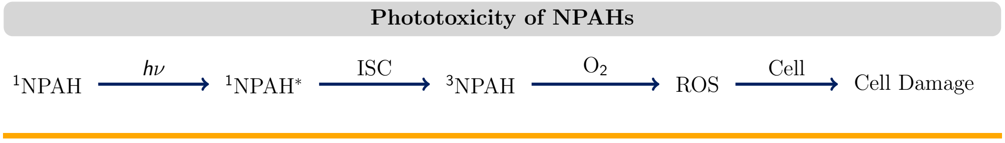

$$^{1}\text{NPAH} \xrightarrow{h\nu} {}^{1}\text{NPAH}^{*} \xrightarrow{\text{ISC}} {}^{3}\text{NPAH} \xrightarrow{\text{O}_2} \text{ROS} \xrightarrow{\text{Cell}} \text{Cell Damage}$$

Figure 1.2: Phototoxicity of NPAHs exerted by production of reactive oxygen species (ROS).

increases the risk of skin cancer, and inhalation leads to increased risk of lung and bladder cancer.[64] NPAHs are produced mainly from incomplete combustion of organic materials, such as the burning of fossil fuels, but are also emitted to the atmosphere naturally, e.g., through volcanic eruptions. Because of their ubiquitous presence in the environment, many of these compounds represent a health risk to humans. NPAHs themselves are biologically inert and require either metabolic activation or photoactivation to exert their toxicity.[63] Upon UVA irradation, they have been shown to induce DNA cleavage[63] and lipid peroxidation mediated by reactive intermediates including reactive oxygen species.[65] Radical oxygen speciies can be produced through the reaction of compounds in electronic triplet states with molecular oxygen, and since NPAHs can undergo ISC efficiently, they can effectively produce radical oxygen species after photoexcitation (see Figure 1.2). Thus, a key factor in understanding the phototoxicity of NPAHs is to understand the reasons that enable ISC to take place on an ultrafast time scale making it so efficient for these molecules.

1.3 Understanding Excited-State Dynamics

The systematic study of ultrafast electronic relaxation processes has became possible only a few decades ago with both, the advent of spectroscopic methods possessing femtosecond resolution[66] and developments in the field of computational chemistry allowing for an accurate quantum chemical treatment of molecules comprising more than a few atoms.[67] Time-resolved spectroscopic methods such as transient absorption or photoelectron spectroscopy can nowadays provide a real-time monitoring of selected electronic-state properties, and, thus, can give indirect access on what is happening during the ultrafast reaction dynamics. However, establishing reaction mechanisms of these dynamics solely based on interpretation of experimental results is no trivial task. Thus, spectroscopic studies of excited-state dynamics are routinely supported by quantum chemical calculations. These calculations focus mainly on static excited-state properties such as excited-state energies or transition probabilities at selected nuclear conformations, which are assumed to be critical in the description of the excited-state dynamics mechanism.

Still, a complete picture of the relaxation processes after photoexcitation can only be obtained when the molecular excited-state dynamics are simulated explicitely. Such simulations can become very time consuming when reliable, accurate computational methods are employed. Thus, they are still the exception in studies of excited-state dynamics, especially when investigating ISC processes that require the inclusion of spin-orbit couplings. One particular useful computational method for simulating the dynamical processes in the electronically excited states of a molecule is the surface-hopping approach.[68–70] Surface hopping has been applied routinely in studies of IC processes before, but only recently a generalized surface-hopping formalism, named SHARC, has been implemented.[71,72] This method is able to describe ISC on the same footing as IC, thus opening the door to the study of general excited-state processes.

1.4 The Challenges Tackled in This Work

Equipped with the recently developed SHARC approach, this thesis set out in 2014 to study the excited states of nitro aromatic compounds to gain insight into the nature of their ultrafast ISC dynamics. In particular, the excited-state dynamics of three nitronaphthalene derivatives were simulated in this thesis. The simulations allowed to propose new mechanisms that could describe in detail the photorelaxation of the nitronaphthalene derivatives and these insights may also extend to other NPAHs. The knowledge gained in these simulations, however, are only one of the three main advancements achieved in this work.

Similar to chemical reactions, scientific studies are often presented in a clean, linear way, describing only the direct pathways that lead from the discovery of one key aspect of the study to the discovery of the next. However, like the real dynamics in chemical systems, the work flow in scientific studies is nonlinear and rich of obstacles and barriers. Two of these unforeseen challenges represented the realization of the importance of vibrational sampling on the description of electronically excited states, and the problems of the CASPT2 method in describing electronic states. Through much effort, these challenges turned into valuable learning experiences, and the insights gained on vibrational sampling and the CASPT2 method represent the other two main advancements achieved in this work.

The rest of this thesis is structured as follows. Chapter 2 gives an overview of the theories, methods, and approximations used in the calculations conducted in this work. Chapter 3 presents the studies of the absorption spectra of nitrobenzene and 2-nitronaphthalene. It highlights the importance of vibrational sampling on the correct description of electronically excited states and discusses different vibrational sampling methods. Chapter 4 explains in more detail the theory of the CASPT2 method and discusses its performance in describing electronically excited states of a large number of organic molecules. Chapter 5 then returns to the original topic of this thesis, presenting the results of the excited-state dynamics simulations of the nitronaphthalene derivatives. The order of the topics in Chapters 3-5 roughly follows the timeline in which the topics were studied durint this thesis. However, the topics are also presented in this order as each part of this work built up on the insights gained in the previous parts, i.e., making the work in the latter chapters easier accessible after having understood the former chapters. Each of the Chapters 3-5 contains a short concluding section on its corresponding topic, while Chapter 6 closes this thesis with a complete summary of all results.

2 Theory, Methods, and Approximations

This chapter presents an overview of the theories, methods, and approximations employed in this work. Starting from the time-dependent Schrödinger equation, the Born-Oppenheimer approximation will be introduced, which decouples the motion of the electrons and nuclei in a molecule. Several methods treating the electronic part of the Schrödinger equation are presented and the principal transitions between different electronic states are described. At last, the surface-hopping method, an approach to describe the nuclear motion in different electronic states, is explained.

2.1 The Schrödinger Equation

The fundamental equation-of-motion for a non-relativistic quantum mechanical system is the time-dependent Schrödinger equation. In atomic units ($\hbar = e = m_e = 4\pi\epsilon_0 = 1$), it reads

$$\hat{\mathcal{H}}(\mathbf{x}, t) \left|\Psi(\mathbf{x}, t)\right\rangle = \mathrm{i}\frac{\partial \left|\Psi(\mathbf{x}, t)\right\rangle}{\partial t}, \tag{2.1}$$

where $\hat{\mathcal{H}}$ and $|\Psi\rangle$ are the Hamiltonian and wave function of the system, respectively. $\mathbf{x}$ denotes the coordinates of all the particles in the system. All information about the quantum-mechanical state of the system is encoded in the wave function Ψ, and it is the central aim of quantum chemistry to calculate Ψ as accurately as possible. The Hamiltonian $\hat{\mathcal{H}}$ is the operator describing the energies and interactions between all particles of the system. When the Hamiltonian does not depend on time t, then the wave function can be written as a product of a time-independent part and a time-dependent phase factor

$$\left|\Psi(\mathbf{x}, t)\right\rangle = \left|\Psi(\mathbf{x})\right\rangle \cdot \mathrm{e}^{-\mathrm{i}Et}, \tag{2.2}$$

Inserting this ansatz in eq. (2.1) and multiplying the result by the complex number $\mathrm{e}^{\mathrm{i}Et}$ yields the time-independent form of the Schrödinger equation

$$\hat{\mathcal{H}}(\mathbf{x}) \left|\Psi(\mathbf{x})\right\rangle = E \cdot \left|\Psi(\mathbf{x})\right\rangle, \tag{2.3}$$

where E is the total energy of the system.

For a molecule containing N electrons at coordinates $\mathbf{r}_i$ and K nuclei of charges Z_A and masses M_A at coordinates $\mathbf{R}_A$, the Hamiltonian $\hat{\mathcal{H}}$ reads

$$\hat{\mathcal{H}}(\mathbf{r},\mathbf{R}) = \underbrace{-\sum_{i}^{N}\frac{1}{2}\nabla_i^2}_{\hat{\mathcal{T}}^{el}} + \underbrace{\sum_{i<j}^{N}\frac{1}{|\mathbf{r}_i-\mathbf{r}_j|}}_{\hat{\mathcal{V}}^{ee}} \underbrace{-\sum_{i}^{N}\sum_{A}^{K}\frac{Z_A}{|\mathbf{r}_i-\mathbf{R}_A|}}_{\hat{\mathcal{V}}^{ne}}$$

$$\underbrace{-\sum_{A}^{K}\frac{1}{2M_A}\nabla_A^2}_{\hat{\mathcal{T}}^{n}} + \underbrace{\sum_{A<B}^{K}\frac{Z_A Z_B}{|\mathbf{R}_A-\mathbf{R}_B|}}_{\hat{\mathcal{V}}^{nn}}\,. \tag{2.4}$$

The Hamiltonian $\hat{\mathcal{H}}$ is the sum of the kinetic energies of the electrons ($\hat{\mathcal{T}}^{el}$) and nuclei ($\hat{\mathcal{T}}^{n}$), and the Coulomb interactions among the electrons ($\hat{\mathcal{V}}^{ee}$), among the nuclei ($\hat{\mathcal{V}}^{nn}$), and between both types of particles ($\hat{\mathcal{V}}^{ne}$). As the Hamiltonian depends on the coordinates of all electrons and nuclei as in eq. (2.4), so does the wave function, i.e., $|\Psi\rangle = |\Psi(\mathbf{r},\mathbf{R})\rangle$, which makes eq. (2.3) very difficult to solve. For this reason, subsequently a hierarchy of approximations is introduced. These approximations take away complexity from the task of solving the Schrödinger equation, however, they also can introduce unknown errors in the solutions obtained in this way. Since the actual calculations involved in solving the Schrödinger equation are performed on computers nowadays, it is the responsibility and main task of the theoretical chemist to know when and know how to apply these approximations when performing theoretical studies.

2.2 The Born-Oppenheimer Approximation

The most fundamental approximation in quantum chemistry is the Born-Oppenheimer approximation (BOA).[73] It decouples the motion of the electrons from the motion of the nuclei, which allows one to solve the electronic part of the Schrödinger equation separately from the nuclear part. In the BOA, one considers that the motion of the electrons is much faster than that of the heavier atomic nuclei, and extends this observation to the limit where the nuclei are assumed static in the context of the motion of the electrons. Then, the positions of the nuclei $\mathbf{R}$ are fixed, the Coulomb interaction between them becomes constant, and their kinetic energy becomes $\hat{\mathcal{T}}^n = 0$. For this case, only the electronic part of the Schrödinger equation

$$\hat{\mathcal{H}}^{el}\left|\Psi^{el}(\mathbf{r};\mathbf{R})\right\rangle = E^{el}(\mathbf{R})\cdot\left|\Psi^{el}(\mathbf{r};\mathbf{R})\right\rangle, \tag{2.5}$$

where $\hat{\mathcal{H}}^{el} = \hat{\mathcal{H}} - \hat{\mathcal{T}}^n$, remains to be solved. Solution of the electronic Schrödinger equation yields the electronic wave functions $\left|\Psi^{el}(\mathbf{r};\mathbf{R})\right\rangle$ and electronic energies $E^{el}(\mathbf{R})$. Both, $\left|\Psi^{el}(\mathbf{r};\mathbf{R})\right\rangle$ and $E^{el}(\mathbf{R})$ depend parametrically on the nuclear coordinates $\mathbf{R}$. $E^{el}(\mathbf{R})$ is a multidimensional function that is usually called potential-energy surface (PES), and is lateron used to model the motion of the nuclei.

Formally, the BOA can be derived by writing the total wave function as a linear combination of electronic wave functions

$$|\Psi(\mathbf{r},\mathbf{R})\rangle = \sum_i \left|\Psi_i^{el}(\mathbf{r};\mathbf{R})\right\rangle \cdot |\Theta_i^n(\mathbf{R})\rangle \,. \tag{2.6}$$

Inserting this form of the total wave function into eq. (2.3) and projection onto a specific electronic state $\left\langle \Psi_j^{el}(\mathbf{r};\mathbf{R})\right|$ yields

$$\left(\hat{\mathcal{T}}^n + E_j^{el}\right) \left|\Theta_j^n(\mathbf{R})\right\rangle + \sum_i \hat{\mathcal{T}}_{ij}^{NAC} \left|\Theta_i^n(\mathbf{R})\right\rangle = E \cdot \left|\Theta_j^n(\mathbf{R})\right\rangle , \tag{2.7}$$

where the expansion coefficients $|\Theta_i^n\rangle$ of eq. (2.6) take the role of the nuclear wave functions. The operator

$$\hat{\mathcal{T}}_{ij}^{NAC} = -\sum_A \frac{1}{2M_A}\left[\left\langle \Psi_j^{el}\middle|\nabla_A^2\middle|\Psi_i^{el}\right\rangle + \left\langle \Psi_j^{el}\middle|\nabla_A\middle|\Psi_i^{el}\right\rangle \nabla_A\right] \tag{2.8}$$

contains the so-called nonadiabatic couplings (NACs) that couple the electronic wave functions with the nuclear motion. In the BOA, one simply neglects the NACs, which simplyfies eq. (2.7) to the nuclear Schrödinger equation for a single electronic PES:

$$\left(\hat{\mathcal{T}}^n + E_j^{el}\right) \left|\Theta_j^n(\mathbf{R})\right\rangle = E \cdot \left|\Theta_j(\mathbf{R})\right\rangle . \tag{2.9}$$

Therefore, the BOA is an adequate approximation, if the NACs between the different electronic states are small. This is often the case when the electronic states are far away in energy. In practice, the BOA is, thus, often a good approximation when one deals only with the lowest-energy electronic state (electronic ground state) as it is often well separated in energy from the excited electronic states. In general, however, when two electronic states come close in energy, their NACs increase, becoming no longer negligible, and the BOA breaks down. This scenario is frequently encountered when the nuclei move in the potential of electronically excited states, and it is mandatory, then, to include the NACs when describing the nuclear motion of a molecule.

2.3 Electronic Structure Theory

In the framework of the BOA, one is left with the problem to solve the electronic Schrödinger equation [eq. (2.5)], which in itself is a difficult task for atoms and molecules with more than a few electrons. For this task, there exist two families of methods: wave-function based methods and (electron) density based methods; both will be introduced briefly in the following. Since this section deals only with the electronic part of the Schrödinger equation, the superscript "*el*" will be dropped hereafter.

2.3.1 The Hartree-Fock Approximation

The starting point of wave-function based methods is usually the Hartree-Fock (HF) approximation[74], which is based on the variational principle of quantum mechanics. The variational principle states that for any test function $\left|\Psi^{\text{test}}\right\rangle$ that is used as an approximation of the exact solution of the Schrödinger equation ($\left|\Psi^{\text{exact}}\right\rangle$), its energy expectation value will be

$$\left\langle E^{\text{test}}\right\rangle = \frac{\left\langle \Psi^{\text{test}} \middle| \hat{\mathcal{H}} \middle| \Psi^{\text{test}} \right\rangle}{\left\langle \Psi^{\text{test}} \mid \Psi^{\text{test}} \right\rangle} \geq \frac{\left\langle \Psi^{\text{exact}} \middle| \hat{\mathcal{H}} \middle| \Psi^{\text{exact}} \right\rangle}{\left\langle \Psi^{\text{exact}} \mid \Psi^{\text{exact}} \right\rangle} = E^{\text{exact}}, \tag{2.10}$$

where the equation only holds in the case of $\left|\Psi^{\text{test}}\right\rangle = \left|\Psi^{\text{exact}}\right\rangle$. Following the variational principle, one can choose a test function of a certain form and systematically vary its parameters to minimize the energy, arriving at the best approximation to the exact wave function when the energy is minimized.

In the HF approximation, one uses a so-called Slater determinant to describe an N-electron wave function, i.e.,

$$\left|\Psi^{\text{test}}\right\rangle = \left|\psi_{\text{HF}}\right\rangle = \frac{1}{\sqrt{N!}} \begin{vmatrix} \varphi_1(\mathbf{r}_1) & \varphi_1(\mathbf{r}_2) & \cdots & \varphi_1(\mathbf{r}_N) \\ \varphi_2(\mathbf{r}_1) & \varphi_2(\mathbf{r}_2) & \cdots & \varphi_2(\mathbf{r}_N) \\ \vdots & \vdots & \ddots & \vdots \\ \varphi_N(\mathbf{r}_1) & \varphi_N(\mathbf{r}_2) & \cdots & \varphi_N(\mathbf{r}_N) \end{vmatrix}, \tag{2.11}$$

$\left|\psi_{\text{HF}}\right\rangle$ is a product of N single-electron wave functions φ_i, so-called orbitals. The determinant form of the wave function follows from the Pauli principle, which states that the total wave function $\left|\psi_{\text{HF}}\right\rangle$ has to change its sign when the coordinates of the electrons, say $\mathbf{r}_i$ and $\mathbf{r}_j$, are interchanged. Inserting $\left|\psi_{\text{HF}}\right\rangle$ into the electronic Schrödinger equation and applying the variational principle yields the HF equations,

$$\hat{\mathcal{F}} \left|\varphi_i(\mathbf{r}_i)\right\rangle = \epsilon_i \left|\varphi_i(\mathbf{r}_i)\right\rangle, \tag{2.12}$$

which determine the HF orbitals $\left|\varphi_i(\mathbf{r}_i)\right\rangle$. $\hat{\mathcal{F}}$ is the Fock operator which is an effective one-electron operator, i.e., it acts only on the coordinates of one electron. In this form, the difficult task of solving an N-dimensional problem is transformed into the much easier task of solving N one-dimensional problems. The Fock operator $\hat{\mathcal{F}}$ contains the kinetic energy of the electron, the interaction to the nuclei, and the averaged interaction to all other electrons. Through the latter term, the Fock operator $\hat{\mathcal{F}}$ depends on the orbitals $\left|\varphi_i(\mathbf{r_i})\right\rangle$, i.e., its own eigenfunctions. Therefore, eq. (2.12) has to be solved iteratively until self-consistency is achieved, i.e., until eq. (2.12) holds.

To apply the HF approximation in practice, one still needs to choose an explicit form for the orbitals $\left|\varphi_i(\mathbf{r}_i)\right\rangle$. In general, this is done by writing the orbitals $\left|\varphi_i(\mathbf{r}_i)\right\rangle$ in terms of a linear combination of atomic basis functions $\left|\chi_a(\mathbf{r}_i)\right\rangle$, i.e.,

$$\left|\varphi_i(\mathbf{r}_i)\right\rangle = \sum_a c_{ia} \left|\chi_a(\mathbf{r}_i)\right\rangle. \tag{2.13}$$

For practical applications, there exist a large number of sets of pre-determined atomic basis functions $\left|\chi_a(\mathbf{r}_i)\right\rangle$, so-called basis sets, to choose from. These basis sets vary, e.g., in size –through the number of functions they contain for each element – and different quantum chemical methods display a different dependence of their performance when varying the basis set. Therefore, choosing an appropriate basis set generally depends on the molecule and property that is to be investigated. However, in every case, using a larger basis set will result in longer computing times, increasing the so-called computational cost of a calculation.

Even in the limit of an infinetly large basis set, the HF wave function will differ from the exact wave function and, thus, its energy will be larger than the exact energy. The difference between the HF energy and the exact energy is called correlation energy,

$$E^{\text{corr}} = E^{\text{HF}} - E^{\text{exact}}. \tag{2.14}$$

This difference is due to the fact that in the HF approximation, each electron only experiences an averaged interaction with the other electrons; no explicit interaction between the individual electrons is taken into account. E^{corr} is usually only a small fraction of the exact energy, however, it is the fraction that varies the most when comparing different isomers or different electronic states of a molecule. As, in practice, one is usually interested more in relative than in total energies, the HF approximation, thus, is rarely applied on its own. Rather, it is used as a starting point in combination with so-called post-HF methods, which aim at calculating the correlation energy which is missing in the HF approximation.

2.3.2 Multi-Configurational Methods

The basic assumption in the HF approximation consists of using a single Slater determinant for the wave function of the system. The Slater determinant is built from orbitals that are either occupied by an electron or not, establishing a specific electronic configuration. Thus, the natural extension in all post-HF methods is to consider more than one configuration for the wave function, e.g.,

$$|\Psi\rangle = |\psi_{\text{HF}}\rangle + \sum_r C_r \, |\psi_r\rangle \tag{2.15}$$

The additional configurations $|\psi_r\rangle$, called excited configurations, can be constructed by replacing one or more orbitals that are occupied (φ_i) in the HF wave function with orbitals that are unoccupied (φ_a). The coefficients C_r in the expansion are determined either by applying the variational principle or by using perturbation theory.

In principle, one can construct a wave function including all possible configurations from the available orbitals, i.e., all singly-excited configurations, doubly-excited configurations, …, up to N-times excited configurations. This

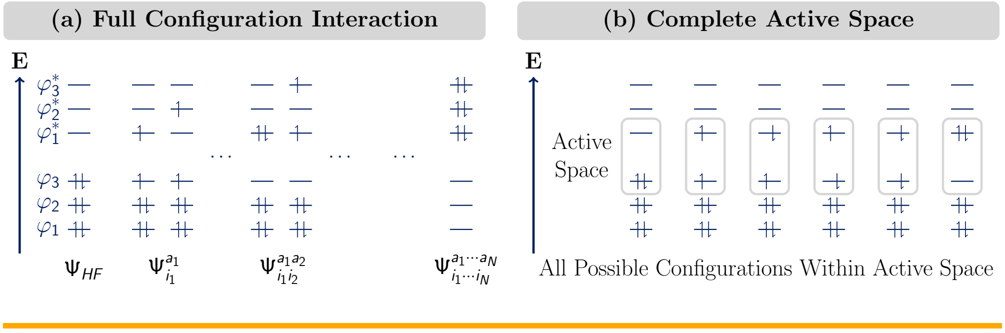
(a) Full Configuration Interaction
(b) Complete Active Space
E
φ_3^*
φ_2^*
φ_1^*
φ_3
φ_2
φ_1
Ψ_{HF}
$\Psi_{i_1}^{a_1}$
$\Psi_{i_1 i_2}^{a_1 a_2}$
$\Psi_{i_1 \cdots i_N}^{a_1 \cdots a_N}$
Active Space
All Possible Configurations Within Active Space

Figure 2.1: Pictorial representation of all configurations considered in (a) full configuration interaction and (b) complete-active-space method.

full configuration interaction (FCI) wave function [see Figure 2.1(a)]

$$
\begin{aligned}
|\Psi_{\mathrm{FCI}}\rangle = |\psi_{\mathrm{HF}}\rangle + \sum_{i_1,a_1} C_{i_1}^{a_1} \left|\psi_{i_1}^{a_1}\right\rangle + \sum_{i_1 i_2, a_1 a_2} C_{i_1 i_2}^{a_1 a_2} \left|\psi_{i_1 i_2}^{a_1 a_2}\right\rangle + \dots \\
\dots + \sum_{i_1 \dots i_N, a_1 \dots a_N} C_{i_1 \dots i_N}^{a_1 \dots a_N} \left|\psi_{i_1 \dots i_N}^{a_1 \dots a_N}\right\rangle
\end{aligned}
\tag{2.16}
$$

gives the exact solution of the electronic Schrödinger equation in the representation of the basis set that is used. However, due to the large number of configurations, calculation of $|\Psi_{\mathrm{FCI}}\rangle$ usually comes with prohibitively large computational costs, so that FCI calculations are limited to small molecules and the usage of small basis sets, e.g., systems with no more than 10 electrons and 30 basis functions.

In practical applications, the number of configurations has to be restricted. One popular approach to include only the most important configurations in the expansion of the wave function is the complete-active-space (CAS) method. In CAS, a small number of orbitals are selected and a FCI calculation is performed only in the subspace of these orbitals –the active space –while all other orbitals are either occupied or unoccupied [see Figure 2.1(b)]. The orbitals in the active space have to be chosen manually. For certain classes of molecules and problems that are regularly studied, there exist a number of guidelines on how to properly select these orbitals. However, in general finding an appropriate active space is an intricate problem that is normally only solved by trial and error –aided by "chemical intuition", i.e., experience.[75] As CAS is a variational method, in principle, the CAS wave function can be improved systematically by enlarging the active space. However, since the number of configurations scales factorially with the number of orbitals and electrons included in the active space, calculations are usually restricted, e.g., to 18 orbitals and 18 electrons. In practice, typically the self-consistent field CAS variant (CASSCF) is used[76], where not only the coefficents of the configurations C_r from eq. (2.15) but also the coeffients of the orbitals c_r from eq. (2.13) are determined variationally.

While CASSCF usually gives a qualitatively correct description of electronic states that require a multi-configurational wave function, its relative energies are typically not very accurate. One way to improve the CASSCF results is to use perturbation theory and employ the CASSCF wave function as the zeroth-order reference wave function. In perturbation theory, the Hamiltonian is partitioned into a part $\hat{\mathcal{H}}_0$ with a known solution ($\left|\Psi_i^{(0)}\right\rangle$), and a part $\hat{\mathcal{H}}'$ that acts as a perturbation on $\left|\Psi_i^{(0)}\right\rangle$, i.e.,

$$\left(\hat{\mathcal{H}}_0 + \lambda\hat{\mathcal{H}}'\right)|\Psi_i\rangle = E_i\,|\Psi_i\rangle \tag{2.17}$$

$$\hat{\mathcal{H}}_0\left|\Psi_i^{(0)}\right\rangle = E_i^{(0)}\left|\Psi_i^{(0)}\right\rangle \tag{2.18}$$

By expanding both the wave function $|\Psi_i\rangle$ and the energy E_i in powers of a parameter λ

$$|\Psi_i\rangle = \left|\Psi_i^{(0)}\right\rangle + \lambda\left|\Psi_i^{(1)}\right\rangle + \lambda^2\left|\Psi_i^{(2)}\right\rangle + \ldots \tag{2.19}$$

$$E_i = E_i^{(0)} + \lambda E_i^{(1)} + \lambda^2 E_i^{(2)} + \ldots \tag{2.20}$$

and insertion in eq. (2.17), one arrives at a system of equations that allows the determination of the contributions $\left|\Psi_i^{(n)}\right\rangle$ and $E_i^{(n)}$ order by order.

$$\lambda^0: \qquad \hat{\mathcal{H}}_0\left|\Psi_i^{(0)}\right\rangle = E_i^{(0)}\left|\Psi_i^{(0)}\right\rangle \tag{2.21}$$

$$\lambda^1: \qquad \hat{\mathcal{H}}_0\left|\Psi_i^{(1)}\right\rangle + \hat{\mathcal{H}}'\left|\Psi_i^{(0)}\right\rangle = E_i^{(0)}\left|\Psi_i^{(1)}\right\rangle + E_i^{(1)}\left|\Psi_i^{(0)}\right\rangle \tag{2.22}$$

$$\cdots$$

$$\lambda^n: \qquad \hat{\mathcal{H}}_0\left|\Psi_i^{(n)}\right\rangle + \hat{\mathcal{H}}'\left|\Psi_i^{(n-1)}\right\rangle = \sum_{m=0}^{n} E_i^{(n)}\left|\Psi_i^{(n-m)}\right\rangle \tag{2.23}$$

The energy contribution up to second-order can be computed by knowledge of the eigenfunctions $\left|\Psi_j^{(0)}\right\rangle$ of the zeroth-order Hamiltonian $\hat{\mathcal{H}}_0$ alone, i.e.,

$$E_i^{(0)} = \left\langle\Psi_i^{(0)}\middle|\hat{\mathcal{H}}_0\middle|\Psi_i^{(0)}\right\rangle \tag{2.24}$$

$$E_i^{(1)} = \left\langle\Psi_i^{(0)}\middle|\hat{\mathcal{H}}'\middle|\Psi_i^{(0)}\right\rangle \tag{2.25}$$

$$E_i^{(2)} = -\sum_{j\neq i}\frac{\left|\left\langle\Psi_i^{(0)}\middle|\hat{\mathcal{H}}'\middle|\Psi_j^{(0)}\right\rangle\right|^2}{E_j^{(0)} - E_i^{(0)}}. \tag{2.26}$$

There exist different approaches on how to define the zeroth-order Hamiltonian $\hat{\mathcal{H}}_0$ when using a CASSCF wave function as the reference function $\left|\Psi^{(0)}\right\rangle$. The most popular formulation is probably the second-order treatment called CASPT2[77,78], where a combination of projection operators $\hat{\mathcal{P}}_i$ and an effective one-electron operator, the generalized Fock operator $\hat{\mathcal{F}}$, is used in the zeroth-order Hamiltonian

$$\hat{\mathcal{H}}_0 = \hat{\mathcal{P}}_0\hat{\mathcal{F}}\hat{\mathcal{P}}_0 + \hat{\mathcal{P}}_{\mathrm{K}}\hat{\mathcal{F}}\hat{\mathcal{P}}_{\mathrm{K}} + \hat{\mathcal{P}}_{\mathrm{SD}}\hat{\mathcal{F}}\hat{\mathcal{P}}_{\mathrm{SD}}. \tag{2.27}$$

The projection operators project on the CASSCF reference wave function ($\hat{\mathcal{P}}_0$) and all single and double excitations inside ($\hat{\mathcal{P}}_K$) as well as outside ($\hat{\mathcal{P}}_{\mathrm{SD}}$) of the active space. In matrix form, $\hat{\mathcal{F}}$ possesses the elements

$$f_{pq} = h_{pq} + \sum_{rs} N_{rs} \left[\left\langle \varphi_p \varphi_r \left| \frac{1}{r_{12}} \right| \varphi_q \varphi_s \right\rangle - \frac{1}{2} \left\langle \varphi_p \varphi_q \left| \frac{1}{r_{12}} \right| \varphi_r \varphi_s \right\rangle \right] \tag{2.28}$$

where h_{pq} collects all one-electron terms and N_{rs} denotes the matrix elements of the one-electron density matrix. The generalized Fock matrix $\mathbf{f}$ consists of 3×3 blocks corresponding to the three orbital subspaces of inactive ($N_{pp} = 2$), active ($0 \leq N_{pp} \leq 2$), and secondary ($N_{pp} = 0$) orbitals. The coupling between the inactive and secondary blocks is zero according to the generalized Brillouin theorem. The inactive-inactive, active-active, and secondary-secondary blocks may be diagonalized; in general, however, $\mathbf{f}$ is non-diagonal.

As an extension to CASPT2, there exist also CASSCF-based perturbation theory methods such as the second-order n-electron valence state perturbation theory (NEVPT2), where two-electron terms are included in the reference Hamiltonian.[79–81] In principle, NEVPT2 should be more accurate than CASPT2. However, due to the increased computational costs that come with evaluating the two-electron parts of the Hamiltonian, in practice one uses smaller, contracted sets of configurations in NEVPT2 compared to CASPT2, thus, loosing the advantage in accuracy that non-contracted NEVPT2 has over CASPT2. Further features of CASPT2 will be discussed later on in Chapter 4.

2.3.3 Density-Functional Theory

A complementary approach to wave-function-based electron-structure theory is given by density-functional theory (DFT).[82] DFT uses the fact that a quantum system can be described entirely by its electron density $\rho(\mathbf{r})$. Therefore, the central idea of DFT is to determine the electron density instead of the wave function of the system. For an N-electron system, the electron density can be written in terms of the wave function as

$$\rho(\mathbf{r}) = N \cdot \int \mathrm{d}\mathbf{r}_2 \cdots \mathrm{d}\mathbf{r}_N \big| \Psi(\mathbf{r}, \mathbf{r}_2, \ldots, \mathbf{r}_N) \big|^2. \tag{2.29}$$

Thus, through their dependence on the wave function, the energy can be expressed as a functional of the density

$$E = E[\rho] = T[\rho] + V_{ne}[\rho] + V_{ee}[\rho], \tag{2.30}$$

where $T[\rho]$ is the kinetic energy of the electrons, $V_{ne}[\rho]$ is the interaction between the electrons and the nuclei, and $V_{ee}[\rho]$ describes the interaction between the electrons.

The theoretical foundations of DFT lie in the two Hohenberg-Kohn theorems. The first Hohenberg-Kohn theorem states that the ground-state electron density $\rho(\mathbf{r})$ uniquely determines the Hamiltonian of the system, and, therefore also the ground-state energy E_0. The second Hohenberg-Kohn theorem states that the density obeys the variational principle, i.e., assuming a specific functional form one can systematically optimize the density by minimizing its energy. In practice, this variational procedure is usually done in the Kohn-Sham (KS) formalism. In this approach, one assumes a fictitous system of non-interacting electrons with a density $\widetilde{\rho}(\mathbf{r})$ that is the same as the density $\rho(\mathbf{r})$ of the real system of interacting electrons. For the non-interacting system, the Hamiltonian $\hat{\mathcal{H}}^{ni}$ is a sum of one-particle operators accounting for the kinetic energy of the non-interacting electrons and their repulsion to the nuclei, i.e., $\hat{\mathcal{H}}^{ni} = \hat{\mathcal{T}}^{ni} + \hat{\mathcal{V}}^{ne}$. The eigenfunction of this Hamiltonian is just a single Slater determinant composed of orbitals $|\varphi_i\rangle$ [eq. (2.11)], so that the densities of both the real and the fictitous system can be expressed as

$$\rho(\mathbf{r}) = \widetilde{\rho}(\mathbf{r}) = \sum_{i=1}^{N} \langle \varphi_i \,|\, \varphi_i \rangle \,. \tag{2.31}$$

Using this expression for density, the energy for the real system of interacting electrons is given by

$$\begin{aligned} E[\rho(\mathbf{r})] = & \underbrace{-\sum_{i=1}^{N} \left\langle \varphi_i \left| \frac{\nabla_i^2}{2} \right| \varphi_i \right\rangle}_{T^{ni}} \underbrace{- \sum_{i=1}^{N} \sum_{A=1}^{K} \left\langle \varphi_i \left| \frac{Z_A}{|\mathbf{r}_i - \mathbf{R}_A|} \right| \varphi_i \right\rangle}_{V^{ne}} \\ & \underbrace{+ \sum_{i=1}^{N} \left\langle \varphi_i \left| \frac{1}{2} \int \mathrm{d}\mathbf{r}' \frac{\rho(\mathbf{r}')}{|\mathbf{r}_i - \mathbf{r}'|} \right| \varphi_i \right\rangle}_{J} \quad + \quad E^{xc}[\rho], \end{aligned} \tag{2.32}$$

where $\mathbf{r}'$ is a dummy variable used for the integration over the electronic coordinates. T^{ni} is the kinetic energy of the non-interacting electrons, that differs, however, from the kinetic energy of the system of interacting electrons. V^{ne} is the interaction between the electrons and the nuclei that is the same for both the fictitous and the real system. J captures the part of V^{ee} representing the classical Coulomb repulsion between the electrons. $E^{xc}[\rho]$ is called the exchange-correlation energy functional and it accounts for all non-classical interactions between the electrons as well as the difference between the kinetic energies of the real and the fictitous system of electrons. The orbitals $|\varphi_i\rangle$ are calculated as eigenfunctions of the Kohn-Sham operator $\hat{h}^{KS}$

$$\hat{h}^{KS} |\varphi_i\rangle = \left(-\frac{\nabla_i^2}{2} - \sum_{A=1}^{K} \frac{Z_A}{|\mathbf{r}_i - \mathbf{R}_A|} + \int \mathrm{d}\mathbf{r}' \frac{\rho(\mathbf{r}')}{|\mathbf{r}_i - \mathbf{r}'|} + V^{xc}[\rho] \right) |\varphi_i\rangle = \varepsilon_i \, |\varphi_i\rangle \,. \tag{2.33}$$

$V^{xc}[\rho]$ is the exchange-correlation potential that is given by the functional derivative of $E^{xc}[\rho]$, i.e., $V^{xc}[\rho] = \partial E^{xc}[\rho]/\partial \rho$. Its form is not known and, thus, in every DFT calculation, an approximate form of the $V^{xc}[\rho]$ (or $E^{xc}[\rho]$) functional has to be postulated ad hoc. The approximated functionals may depend solely on the electron density or additional quantities such as the gradient of the density, the Laplacian, etc., and they are classified accordingly as local-density approximation (LDA) functionals, generalized-gradient approximation (GGA) functionals, or meta-GGA functionals, respectively. Sadly, there is no systematic improvement of the accuracy of the functionals when including higher-order derivatives of the density or other terms.[83] Thus, it falls again into the responsibility of the theoretical chemist to carefully select an appropriate functional.

2.3.4 Time-Dependent Density-Functional Theory

In standard DFT, only the ground-state density and its corresponding energy are computed. To calculate electronically excited states, one has to use the time-dependent DFT (TDDFT) formalism.[83,84] In place of the Hohenberg-Kohn theorems for the time-independent DFT, the formal foundations of TDDFT rely on the Runge-Gross theorem –connecting the time-dependent density $\rho(\mathbf{r},t)$ and the time-dependent wave function $|\Psi(\mathbf{r},t)\rangle = |\Psi[\rho(\mathbf{r},t)]\rangle$ –and the action integral

$$A[\rho] = \int_{t_1}^{t_2} \mathrm{d}t \left\langle \Psi[\rho(\mathbf{r},t)] \middle| \mathrm{i}\frac{\partial}{\partial t} - \hat{\mathcal{H}}(\mathbf{r},t) \middle| \Psi[\rho(\mathbf{r},t)] \right\rangle , \tag{2.34}$$

that determines the exact time-dependent density via the Euler equation

$$\frac{\delta A[\rho]}{\delta \rho(\mathbf{r},t)} = 0. \tag{2.35}$$

TDDFT is usually applied in the time-dependent Kohn-Sham formalism, where again a single-configurational wave function is assumed. The time-dependent Kohn-Sham equations read

$$\hat{h}^{KS}[\rho(\mathbf{r},t)]\,|\varphi_i(\mathbf{r},t)\rangle = \mathrm{i}\frac{\partial\,|\varphi_i(\mathbf{r},t)\rangle}{\partial t}, \tag{2.36}$$

where the time-dependent Kohn-Sham operator is given by

$$\hat{h}^{KS}[\rho(\mathbf{r},t)] = -\frac{\nabla^2}{2} - \sum_{A}^{K} \frac{Z_A}{|\mathbf{r}-\mathbf{R}_A|} + \int \mathrm{d}\mathbf{r}' \frac{\rho(\mathbf{r}',t)}{|\mathbf{r}-\mathbf{r}'|} + V^{xc}[\rho(\mathbf{r},t)]. \tag{2.37}$$

The exchange-correlation functional $V^{xc}[\rho(\mathbf{r},t)]$ depends on the time-dependent density, and its exact functional form is not known. This problem is usually dealt with assuming that the exchange-correlation functional is local in time, i.e., $V^{xc} = V^{xc}[\rho_t(\mathbf{r})]$ is a function of an electron density $\rho_t(\mathbf{r})$ that depends only parametrically on time t and is a different function $\rho_t(\mathbf{r})$ for each value of t. Then, in this so-called adiabatic approximation of TDDFT, one can simply employ the approximate exchange-correlation functionals from (time-independent) DFT.

In principle, TDDFT calculations can be performed by propagating the time-dependent Kohn-Sham orbitals using the the time-dependent Kohn-Sham equation (2.36). A more common approach, however, is to calculate the reponse of the density to a time-dependent perturbation, where, for simplicity, one includes only the first (linear) term.[85] For an excited state $|\Psi_I\rangle$ with excitation energy $\omega_I = E_I - E_0$, this linear response problem can be formulated in terms of a matrix pseudo-eigenvalue problem as

$$\begin{bmatrix} \mathbf{A} & \mathbf{B} \\ \mathbf{B}^* & \mathbf{A}^* \end{bmatrix} \begin{pmatrix} \mathbf{X}_I \\ \mathbf{Y}_I \end{pmatrix} = \omega_I \begin{bmatrix} \mathbf{1} & \mathbf{0} \\ \mathbf{0} & \mathbf{-1} \end{bmatrix} \begin{pmatrix} \mathbf{X}_I \\ \mathbf{Y}_I \end{pmatrix}. \tag{2.38}$$

where the matrix elements of $\mathbf{A}$ and $\mathbf{B}$ are given by

$$A_{ia,jb} = \delta_{ij}\delta_{ab}(\varepsilon_a - \varepsilon_i) + \left\langle \varphi_i\varphi_j \,\middle|\, r_{12}^{-1} \,\middle|\, \varphi_a\varphi_b \right\rangle + \left\langle \varphi_i\varphi_j \,\middle|\, f^{xc} \,\middle|\, \varphi_a\varphi_b \right\rangle, \tag{2.39}$$

$$B_{ia,jb} = \left\langle \varphi_i\varphi_b \,\middle|\, r_{12}^{-1} \,\middle|\, \varphi_a\varphi_j \right\rangle + \left\langle \varphi_i\varphi_b \,\middle|\, f^{xc} \,\middle|\, \varphi_a\varphi_j \right\rangle, \tag{2.40}$$

f^{xc} is the exchange-correlation kernel, that in the adiabatic approximation is defined via

$$\left\langle \varphi_i\varphi_j \,\middle|\, f^{xc} \,\middle|\, \varphi_a\varphi_b \right\rangle = \left\langle \varphi_i(\mathbf{r})\varphi_j(\mathbf{r}') \,\middle|\, \frac{\delta^2 E^{xc}}{\delta\rho(\mathbf{r})\delta\rho(\mathbf{r}')} \,\middle|\, \varphi_a(\mathbf{r})\varphi_b(\mathbf{r}') \right\rangle. \tag{2.41}$$

and $\mathbf{X}_I$ and $\mathbf{Y}_I$ are the vectors of particle-hole and hole-particle excitations with respect to the ground state, respectively. TDDFT is often applied in the Tamm-Dancoff approximation (TDA)[86] by setting $\mathbf{Y}_I = 0$ so that only the particle-hole excitations ($\mathbf{X}_I$) are considered. This simplies eq. (2.38) to

$$\mathbf{A}\mathbf{X}_I = \omega_I \mathbf{X}_I. \tag{2.42}$$

In TDA-TDDFT, the wave function of the excited state $|\Psi_I\rangle$ is simply a linear combination of singly-excited configurations with expansion coefficients $X_{i,a}^I$,

$$|\Psi_I\rangle = \sum_{i,a} X_{i,a}^I \left|\psi_i^a\right\rangle. \tag{2.43}$$

Additionally, TDA-TDDFT can, in certain cases, improve the description of excited-state PES by alleviating problems that are introduced due to the usage of approximate exchange-correlation functionals.[83]

2.3.5 Transition-Density Matrix Description of Excited States

While the electronic ground state of many molecules can often be described reasonably by single-configurational wave functions, the electronic structure of excited states is usually more complicated and requires a large number of configurations. This multi-configurational nature complicates the characterization of the excited states, and a simple visual analysis of the orbital and configurations contributing to their wave functions is tedious and prone to be incomplete. Instead, a more convenient approach to describe excited-state properties in great detail is to analyze the one-particle transition density matrix.[87–90] For a transition from the ground state $|\Psi_0\rangle$ to the excited state $|\Psi_I\rangle$, it reads

$$\gamma_{0I}(r_h, r_e) = N \int \mathrm{d}r_2 \cdots \int \mathrm{d}r_N \, \Psi_0(r_h, r_2, \ldots, r_N)\Psi_I(r_e, r_2, \ldots, r_N), \tag{2.44}$$

where r_h and r_e are the coordinates of the hole in the ground-state wave function and the electron in the excited-state wave function, respectively, that describe the transition. In second quantization, the transition-density matrix can also be written as

$$\gamma_{0I}(r_h, r_e) = \sum_{pq} \varphi_p^*(r_h) \underbrace{\left\langle \Psi_0 \,\middle|\, \hat{a}_p^\dagger \hat{a}_q \,\middle|\, \Psi_I \right\rangle}_{D_{pq}^{0I}} \varphi_q(r_e), \tag{2.45}$$

where $\hat{a}_q$ annihilates an electron in orbital φ_q, while $\hat{a}_p^\dagger$ creates a hole in orbital φ_p.

The transition-density matrix has no intuitive interpretation but allows the calculation of many properties that are useful for the description of the excited states. By a singular-value decomposition, $\mathbf{D}^{0I}$ can be written as

$$\mathbf{D}^{0I} = \mathbf{U} \times \mathrm{diag}(\sqrt{\lambda_1}, \sqrt{\lambda_2}, \ldots) \times \mathbf{V}^T. \tag{2.46}$$

where the unitary matrices $\mathbf{U}$ and $\mathbf{V}$ contain the coefficients of the hole and electron parts of the natural-transition orbitals, respectively. These orbitals allow for a compact representation of an electronic excited state by reducing the numbers of configurations needed to describe its wave function. λ_i are the transition amplitudes for each pair of hole and electron natural-transition orbitals.

From $\gamma_{0I}(r_h, r_e)$, the hole density $\rho_h(r_h)$ and the electron density $\rho_e(r_e)$ can be computed simply by

$$\rho_h(r_h) = \int \mathrm{d}r_e \, \gamma_{0I}(r_h, r_e) \tag{2.47}$$

$$\rho_e(r_e) = \int \mathrm{d}r_h \, \gamma_{0I}(r_h, r_e). \tag{2.48}$$

$\rho_h(r_h)$ and $\rho_e(r_e)$ describe the spatial distribution of the hole and electron, respectively. As a measure to quantify the average separation of the hole and electron positions during the transition, the exciton size (ES) can be computed as the root-mean-square separation of the electron and hole positions, i.e.,

$$\mathrm{ES} = \left\langle (r_h - r_e)^2 \right\rangle = \frac{1}{\Omega} \int \mathrm{d}r_h \int \mathrm{d}r_e \, \gamma_{0I}(r_h, r_e)(r_h - r_e)^2 \gamma_{0I}(r_h, r_e) \tag{2.49}$$

where $\Omega = \int \mathrm{d}r_h \int \mathrm{d}r_e \, \gamma_{0I}(r_h, r_e)^2$. The ES serves as an estimate of the spatial extent of the parts of the molecule that are involved in the transition. If the hole and the electron parts are localized on distinct regions in the molecul, it can be useful to divide the molecule into fragments, say A and B, and to calculate the charge-transfer (CT) number from $\gamma_{0I}(r_h, r_e)$ as

$$\mathrm{CT}_{AB} = \int_A \mathrm{d}r_e \int_B \mathrm{d}r_h \, \gamma_{0I}(r_h, r_e)^2. \tag{2.50}$$

CT_{AB} gives the probability of finding the hole on fragment A and the electron on fragment B, and ranges it ranges between $\mathrm{CT} = 0$ for transitions completely localized in one fragment and $\mathrm{CT} = 1$ for pure charge-transfer transitions.

2.3.6 Spin and Spin-Orbit Coupling

In quantum theory, particles can possess an intrinsic non-zero angular momentum, called spin s, that is unconnected to their motion in space. For electrons, this spin can take the values $s = \pm 1/2$, and it represents a fourth degree of freedom in addition to the three spatial degrees of freedom. The spin does not appear in the Schrödinger equation, and, thus, it has to be introduced ad hoc in non-relativistic quantum mechanics. This is usually done by defining a spin operator $\hat{\mathbf{s}} = (\hat{s}_x, \hat{s}_y, \hat{s}_z)$ that acts only on the spin coordinates s of the electrons, and restricting the solutions of the Schrödinger equation to wave functions $|\Psi(\mathbf{r}, s)\rangle$ that are simultaneous eigenfunctions of the Hamiltonian $\hat{\mathcal{H}}$ as well as of the operators $\hat{s}^2$ and $\hat{s}_z$. Since $\hat{s}^2$ and $\hat{s}_z$ do not act on the spatial coordinates of the electrons, $|\Psi(\mathbf{r}, s)\rangle$ can be written simply as a product of a spatial function $|\Psi(\mathbf{r})\rangle$ and a spin-dependent function $|\Sigma(s)\rangle$,

$$|\Psi(\mathbf{r}, s)\rangle = |\Psi(\mathbf{r})\rangle \cdot |\Sigma(s)\rangle \,. \tag{2.51}$$

The spin-dependent functions $|\Sigma(s)\rangle$ are orthogonal for different spins s, i.e., $\langle \Sigma(s) \,|\, \Sigma(s')\rangle = \delta_{ss'}$. Thus, all couplings of electronic wave functions of different spin value are zero, and, as a consequence, transitions between electronic states of different spin value are forbidden.

The situation changes when SOC is taken into account.[91] SOC introduces an interaction between states of different spin multiplicity that mixes these states. The resulting states are not eigenfunctions of the operators $\hat{s}^2$ and $\hat{s}_z$ anymore, so that transition between states, that are formally of different spin multiplicity, become allowed. SOC is a relativistic effect, i.e., it occurs naturally in a formulation of quantum mechanics that includes the principles of the theory of special relativity. Phenomenologically, SOC is explained as the interaction of the magnetic moment of the spin angular momentum with the magnetic field that is induced by the the electron orbiting around the nuclei as well as in the field of the other electrons.[92] This interaction can be computed, e.g., by using the Breit-Pauli Hamiltonian $\hat{\mathcal{H}}^{BP}$,

$$\hat{\mathcal{H}}^{BP} = \frac{1}{2c^2} \sum_{i}^{N} \left[\sum_{A}^{K} Z_A \left(\frac{\hat{\mathbf{r}}_{iA}}{\hat{r}_{iA}^3} \times \hat{\mathbf{p}}_i \right) \cdot \hat{\mathbf{s}}_i + \sum_{j \neq i}^{N} \left(\frac{\hat{\mathbf{r}}_{ij}}{\hat{r}_{ij}^3} \times \hat{\mathbf{p}}_i \right) \cdot (\hat{\mathbf{s}}_i + 2\hat{\mathbf{s}}_j) \right] , \tag{2.52}$$

where $\hat{\mathbf{p}}_i$ is the electronic momentum operator and $c \approx 1/137$ is the speed of light. Through the first term in eq. (2.52), SOCs scale with the charges of the nuclei Z_A. Thus, for molecules containing only light atoms, e.g., organic molecules, SOCs are typically only very small, being of the order of a few or tens of wave numbers, while for molecules containing heavy atoms such as transition metal complexes, SOCs are typically larger, ranging between hundreds and thousands of wave numbers. Furthermore, the size of SOC between different electronic states depends strongly on their symmetry due to the mathematical structure of the SOC operator.[93] For organic molecules, this symmetry dependence is usually expressed by El-Sayed's rules stating that SOCs are larger between states of different excitation character, e.g., between $\pi\pi^*$ and $n\pi^*$ states, than between states of the same character.[94]

2.3.7 Molecules in Solution

The computational costs of solving the electronic Schrödinger equation scale with the number of electrons and basis functions. The explicit scaling differs for different computational methods and is typically correlated to the levels of approximations that have been introduced, i.e., more accurate methods demand a higher scaling factor. For example, when performing excited-state calculations using TDDFT, systems up to ca. 100 atoms can be treated routinely. Using CASPT2 and active spaces of reasonable sizes, the system size shrinks to a (few) dozen(s) of atoms, while for FCI, this number drops to 1-3 atoms. Thus, using this set of methods, a large number of molecules can be investigated computationally when they occur as isolated systems, i.e., having no environment to interact with.

Treating molecules as isolated units is certainly a good approximation, when the molecules are in the gas phase, where encounters with other molecules are comparatively rare events. The situation is different, however, when the molecule is transferred into solution. The solute molecule is then surrounded by and interacts with a number of solvent molecules that is prohibitively large for any quantum chemical calculation. Therefore, for practical studies of molecules in solution, there exist a number of approximate methods such as the cluster model, continuum models, or other mixed quantum-classical methods, that are used instead of a full quantum-mechanical treatment.

In solution, a solute molecule will interact most strongly with the solvent molecules that are located in the immediate vicinity. Thus, in a cluster model, a small number of solvent molecules are included in the quantum system in addition to the solute, trusting that these few solvent molecules sufficiently account for the full solute-solvent interactions. A larger number of solvent molecules can be included in mixed quantum mechanics/molecular mechanics (QM/MM) calculations.[95] Then, the complete system is divided into two regions: a small region A, that is treated at the quantum-mechanical (QM) level, and a large region B, that is treated using classical molecular mechanics (MM), where the atoms are treated as point charges and their interactions are described by empirically parametrized force fields. Region A contains the solute –and possibly a small number of solvent molecules –while the the bulk of the solvent occupies region B. The energy of the complete system E_S can then be written as the sum of the energies of the two subparts, plus an interaction term:

$$E_S = E_A(QM) + E_B(MM) + E_{AB}(QM/MM). \tag{2.53}$$

The energy E_A of the QM region A is evaluated at the QM level while the energy E_B of the MM region B is evaluated at the MM level. To account for the interaction E_{AB} of the QM part (solute) and the MM part (bulk solvent), different approaches exists. The most commonly employed method is the electrostatic-embedding approach, where the charges of the MM atoms are simply included as additional “nuclei” in the Hamiltonian of the QM part to account for their electrostatic interaction with the electrons and nuclei of the QM region. In this way, the MM charges are able to polarize the electron density in the QM region, but the MM charges remain fixed, not being polarized by the QM electron density themselves.

The drawback of the missing polarization of the MM region due to the QM region of the electostatic embedding approach can be remedied by using a polarizable embedding scheme; however, usage of a polarizable force field again comes with an increase of computational cost and, so far, there exist only a small number of parametrized polarizable force fields for specific applications. A general way to account for the mutual polarization of solute and solvent is to use continuum models.[96,97] There, the bulk solvent is modeled by a set of polarizable point charges that are placed on the surface of a cavity that surrounds the solute molecule. The interaction between the solvent and the solute is described by the electrostatic potential between both charge distributions, and as the solvent point charges are polarizable, the solute electron density can also polarize the solvent charge distribution. Thus, a better description of the electrostatic interaction is usually achieved with polarizable continuum models compared to the usage of electrostatic-embedding QM/MM schemes. However, as continuum models do not include any explicit solvent molecules, they cannot describe specific solute-solvent interactions.

2.4 Transitions Between Electronic States

2.4.1 Absorption and Transition-Dipole Moments

In the framework of the BOA, the molecular system occupies vibronic states $|\Psi(\mathbf{r};\mathbf{R})\Theta(\mathbf{R})\rangle$, i.e., vibrational states $|\Theta(\mathbf{R})\rangle$ describing the internal motion of the molecule in the potential of certain electronic states $|\Psi(\mathbf{r};\mathbf{R})\rangle$. The system is stable, i.e., will not change its state in time, when it occupies the lowest-energy state, the ground state, but it can be brought temporarily into an excited state by absorption of light. For this process to occur, the energy of the light must equal the energy difference of the initial (ground) state and final (excited) state, and the transition probability between both states must be non-zero. For electronic transition in molecules, this difference usually lies in the range of a few electron volts, while the difference between vibrational states is much smaller, being of the order of 0.01-0.05 eV. Due to the magnitude of these energy differences, vibronic transitions typically are encountered upon absorption of UV or visible light (200-800 nm or 1.55-6.20 eV).

The probability for a light-induced transition from the vibronic state $|\Psi_p\Theta_p\rangle$ with energy E_p to the vibronic state $|\Psi_q\Theta_q\rangle$ with energy E_q is given by the oscillator strength,

$$f_{p\to q} = \frac{2}{3}\left|\left\langle \Psi_p\Theta_p \middle| \hat{\mathcal{D}} \middle| \Psi_q\Theta_q \right\rangle\right|^2 (E_q - E_p) = \frac{2}{3}\left|D_{pq}\right|^2 \omega_{pq}, \tag{2.54}$$

where $\hat{\mathcal{D}}$ is the transition operator. If the spatial dimensions of the molecule are smaller than the wave length of the light, the transition operator can be approximated by the dipole moment operator $\hat{\boldsymbol{\mu}}$, which depends on the charges and positions of the electrons and nuclei of the molecule

$$\hat{\mathcal{D}} = \hat{\boldsymbol{\mu}} = \hat{\boldsymbol{\mu}}_e(\mathbf{r}) + \hat{\boldsymbol{\mu}}_N(\mathbf{R}) = -\sum_i \mathbf{r}_i + \sum_A Z_A \mathbf{R}_A. \tag{2.55}$$

The transition between the vibronic states in the absorption process occurs much faster than the motion of the nuclei, so that the nuclei are treated static during the transition, and the transitions occur vertically between different vibronic states. For vertical excitations and the dipole approximation, the transition dipole moment $\boldsymbol{\mu}_{pq}$, that replaces D_{pq} in eq. (2.54), becomes

$$\boldsymbol{\mu}_{pq} = \langle\Theta_p|\,[\langle\Psi_p\,|\,\hat{\boldsymbol{\mu}}_e\,|\,\Psi_q\rangle]\,|\Theta_q\rangle + \langle\Theta_p|\hat{\boldsymbol{\mu}}_N[\langle\Psi_p\,|\,\Psi_q\rangle]|\Theta_q\rangle. \tag{2.56}$$

The second term, the nuclear part of the transition dipole moment, is zero due the orthogonality of the electronic states $|\Psi_p\rangle$ and $|\Psi_q\rangle$ for all nuclear positions $\mathbf{R}$. The first term that contains the electronic transition dipole moment $\boldsymbol{\mu}_e^{pq} = \left\langle\Psi_p\,\middle|\,\boldsymbol{\mu}_q\,\middle|\,\Psi_q\right\rangle$ is usually evaluated in the Franck-Condon approximation, where it is assumed to be independent of the position of the nuclei, so that

$$\boldsymbol{\mu}_{pq} = \langle\Theta_p\,|\,\boldsymbol{\mu}_e^{pq}\,|\,\Theta_q\rangle \approx \boldsymbol{\mu}_e^{pq}\,\langle\Theta_p\,|\,\Theta_q\rangle = \boldsymbol{\mu}_e^{pq} S^{pq}, \tag{2.57}$$

where S^{pq} and their squares $|S^{pq}|^2$ are called FC overlap integrals and FC factors, respectively.

Experimentally, the transitions between different electronic states in a substance can be studied by recording an absorption spectrum. The substance is irradiated by light of different wave lengths and its absorbance –the amount of light absorbed –is measured at each wave length, thus giving information about the transition energies and probabilities from the molecule's ground state to its excited states. States that have large absorbance, i.e., possess a large transition probabiltiy, are usually called bright states, while states that absorb only weakly are refered to as dark states. When performing theoretical studies of absorption spectra, usually a number of further approximations are introduced. Although transitions in BO approximation are naturally of vibronic nature, in practice often only the electronic part of the transition is considered when investigating UV-VIS absorption processes. Then, the energy difference $\omega_{pq} = E_q - E_p$ in eq. (2.54) is only the difference between the energies of the potentials of the electronic states, and the FC factors are not taken into account in the calculation of the transition dipole moments in eq. (2.57). Furthermore, for simplification, often only the electronic transitions at the ground-state minimum-energy geometry [Franck-Condon (FC) geometry] are considered, neglecting the vibrational motion of the nuclei.

Finally, since the dipole moment operator $\hat{\boldsymbol{\mu}}_e$ does not depend on the spin [see eq. (2.55)], the transition dipole momemts between electronic states of different spin multiplicity are formally zero, as the overlap of their spin parts is zero. Thus, only excited electronic states that possess the same spin multiplicity as the (initial) ground state can be accessed through absorption. This restriction is lifted when spin-orbit coupling is taken into account (see section 2.3.6). Then,

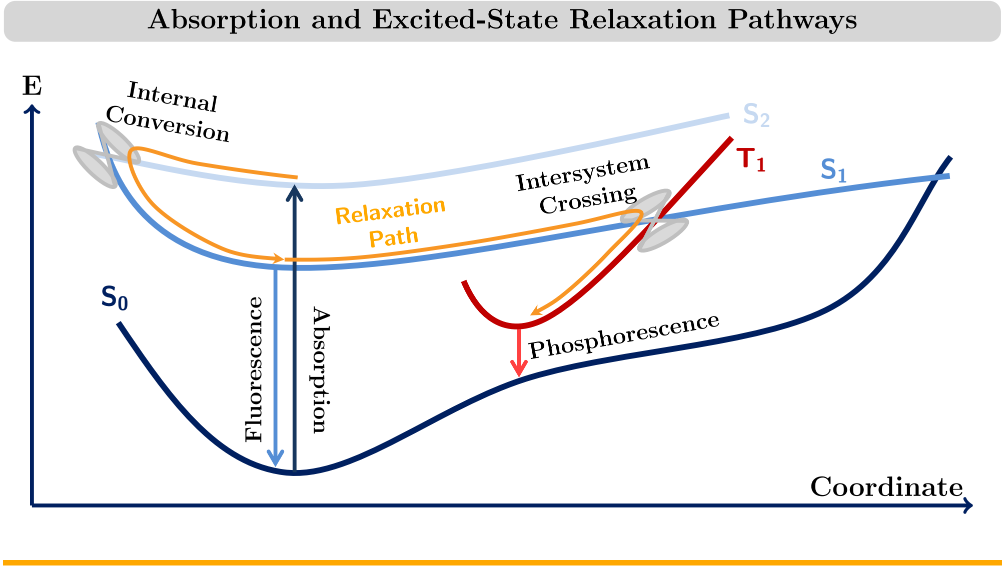

Figure 2.2: Overview over electronic relaxation processes.

also transitions between states that formally possess different spin multiplicity can have non-zero probabilities. For organic molecules, however, where spin-orbit couplings are small, such transition dipole moments are small, so that the absorbance of electronic states of the same spin multiplicity as the ground state –typically a singlet state –is usually much larger than that of states of different spin multiplicity.

2.4.2 Radiative and Nonradiative Relaxation Pathways

When being in an electronically excited state $|\Psi_q\rangle$, there is a non-zero probability for a molecule to spontaneously descend to a lower-lying state $|\Psi_p\rangle$ by emitting a photon of the energy $\omega_{qp} = E_q - E_p$. Thus, electronically excited states are unstable and, over time, the molecule relaxes back to the electronic ground state. The probability of the spontaneous emission of a photon is given by the Einstein coefficient

$$A_{q\rightarrow p} = \frac{4\omega_{qp}^3}{3c^3}\,|\mu_{qp}|^2\,. \tag{2.58}$$

In general, the radiative relaxation can take place on different time scales ranging from nanoseconds to minutes. This process is classified as either fluorescence (F) or phosphorescence (P), depending on whether the two electronic states involved possess the same or different spin multiplicity, respectively (see Figure 2.2). For organic molecules, one finds that fluorescence typically is much faster than phosphorescence –both processes taking place on time scales of 10^{-9}-10^{-6} s (F) and 10^{-4}-10^{+2} s (P).[94] The different time scales can be understood considering that their probabilities are determined by the transition dipole moment $|\mu_{qp}|^2$. As in the case of absorption, $|\mu_{qp}|^2$ is non-zero for states of different spin multiplicity only when SOC is taken into account, but, as SOCs are small for organic molecules, the transition-dipole moments between states of different spin multiplicity are small as well, thus, limiting the rate of phosphoresence.

While being in an excited state, the molecule can relax not only through emission of a photon, but also non-radiatively, by moving on the PES of different electronic states, until it reaches the electronic ground state. In the course of this process, the excess energy of the molecule can be released as heat into the environment through collisions with other molecules. In the BOA, the electronic states, which the molecule temporarily occupies, are orthogonal, making the probability to transfer from one state to another through nuclear motion zero. This orthogonality is lifted when NACs [see eq. (2.8)] are taken into account. NACs couple different electronic states through the motion of the nuclei. NACs are usually small between different states when their energy difference is large, while at points where the energy difference becomes zero –so-called conical intersections (CIs) –the NACs become infinite. More importantly, the NACs remain large also in the vicinity of the CI, thus, making the space around a CI a region where the molecule can effectively be transferred between different electronic states.[98] In the absence of SOCs, NACs are only non-zero between states of the same spin multiplicity. Therefore, it is customary to distinguish the non-radiative transfer between different electronic states as IC or ISC, depending on whether the two electronic states involved possess the same or different spin multiplicity, respectively (see Figure 2.2).

For the non-radiative transfer processes to take place, the molecule needs to move from its initial point of excitation to regions near CIs where the state transfer can occur effectively. In principle, this transfer can take place on the same time scale as the motion of the nuclei, i.e., within several to hundreds of femtoseconds. In practice, however, the rate of a nonradiative relaxation process is determined by the topology of the electronic PES and the size of the NACs and SOCs. While for organic molecules, IC can be observed frequently on the femtosecond time scale, ISC is usually slower. Similar to the comparison of the rates of fluorescence and phosphorescence, the larger rates of IC with respect to ISC are typically explained by the small SOCs in organic molecules that should restrict ISC to be less efficient than IC. Still, for certain classes of organic molecules (see Chapter 1), also ISC has been observed on an ultrafast femtosecond time scale indicating that ISC can be as efficient as IC also for organic molecules. It was this unexpected circumstance that motivated this thesis.

For molecules, the processes of IC, ISC, F, and P after excitation must not be observed mutually exclusive. Rather, these processes can compete or take place sequentially in a cascade that brings the molecule back to its ground state.

2.5 Nuclear Motion

2.5.1 Surface Hopping

The nonradiative relaxation of a molecule after photoexcitation can be investigated theoretically by simulating the nuclear dynamics of the molecule in its electronically excited states. This can be done straighforward by solving the nuclear part of the time-dependent Schrödinger equation. The solutions, the nuclear wave functions, are non-local quantities that depend on the shape of the complete PES. Thus, for this scheme, the complete PES and all NACs have to be pre-computed before propagating the nuclear wave function, which is a computationally very expensive requirement for molecules comprised of more than a few atoms.

To circumvent the problem of having to know the full PES in advance, ab initio molecular dynamics (AIMD) methods can be used. In AIMD, the motion of the nuclei is propageted by classical trajectories on electronic potentials that are obtained from quantum chemical electronic-structure methods. The propagation of the nuclei then depends only on the energies, gradients, and NACs of the electronic states of the current time step, making the pre-computation of these quantities unnecessary. Because of the reduced computational cost, the excited-state dynamics of larger molecules can be simulated. However, due to the introduced classical approximation, this comes at the cost of missing quantum effects such as tunneling or coherence, which are not accounted for in the classical propagation.

The classical trajectories are propagated according to Newton's law of motion, so that the motion of each atom is described by

$$M_A \frac{\mathrm{d}^2}{\mathrm{d}t^2}\mathbf{R}_A(t) = -\nabla_A E_i\left(\mathbf{R}(t)\right). \tag{2.59}$$

In eq. (2.59), the molecule is assumed to be in the electronic state $|\Psi_i\rangle$, the active state, with an energy $E_i(\mathbf{R}(t))$, that depends on all nuclear coordinates. The propagation of the nuclear trajectory from time step t to time step $t+\Delta t$ can be performed using, e.g., the velocity Verlet algorithm,[99,100] where the atomic coordinates $\mathbf{R}_A(t)$ and velocities $\mathbf{v}_A(t)$ are calculated according to

$$\mathbf{R}_A(t+\Delta t) = \mathbf{R}_A(t) + \mathbf{v}_A(t)\Delta t + \frac{1}{2M_A}\nabla_A E_i(t)\Delta t^2 \tag{2.60}$$

$$\mathbf{v}_A(t+\Delta t) = \mathbf{v}_A(t) + \frac{1}{2M_A}\nabla_A E_i(t)\Delta t + \frac{1}{2M_A}\nabla_A E_i(t+\Delta t)\Delta t \tag{2.61}$$

In this manner, the nuclei of the molecule are always propagated on the potential of the same electronic state without the possibility to transfer to another electronic state. An AIMD method that allows for the transfers between different electronic states is the so-called surface hopping.[68,69] In surface hopping, the molecule has the possibility to "hop" from one electronic state $|\Psi_i\rangle$ to another electronic state $|\Psi_j\rangle$ between every time step. The probability for a hop can be calculated in the following way. The electronic wave function $|\Psi(t)\rangle$ is assumed to be a linear combination of different electronic states $|\Psi_i\rangle$, and its time-dependence is moved into the expansion coefficients, i.e.,

$$|\Psi(t)\rangle = \sum_i c_i(t)\,|\Psi_i\rangle\,. \tag{2.62}$$

$|\Psi_i\rangle$ are eigenfunctions of the electronic Hamiltonian $\hat{\mathcal{H}}^{el}$. This ansatz is inserted in the time-dependent electronic Schrödinger equation,

$$\mathrm{i}\frac{\mathrm{d}\,|\Psi(t)\rangle}{\mathrm{d}t} = \hat{\mathcal{H}}^{el}\,|\Psi(t)\rangle\,, \tag{2.63}$$

from which the expansion coefficients can be calculated as

$$\frac{\mathrm{d}c_j(t)}{\mathrm{d}t} = -\sum_i \Bigg[\underbrace{\mathrm{i}\left\langle \Psi_j \,\middle|\, \hat{\mathcal{H}}^{el} \,\middle|\, \Psi_i \right\rangle}_{H_{ji}} + \underbrace{\left\langle \Psi_j \,\middle|\, \frac{\mathrm{d}}{\mathrm{d}t} \,\middle|\, \Psi_i \right\rangle}_{K_{ji}}\Bigg] c_i(t). \tag{2.64}$$

The second term K_{ji} can be computed using the nonadiabatic coupling vector between the electronic states and the velocity of the nuclei

$$K_{ji} = \langle \Psi_j \,|\, \nabla_R \,|\, \Psi_i \rangle\, \mathbf{v}_R. \tag{2.65}$$

From this, the probability $P_{i\rightarrow j}$ of hopping from state $|\Psi_i\rangle$ to state $|\Psi_j\rangle$ can be calculated as

$$P_{i\rightarrow j} = \frac{2\Delta t}{c_i^*(t)c_i(t)} \Re\Big\{c_i^*(t)c_j(t)\,[\mathrm{i}H_{ij} + K_{ij}]\Big\}. \tag{2.66}$$

The classical trajectories in surface hopping are confined to be in a single electronic state at a given nuclear conformation, unlike the quantum mechanical nuclear wave function that has contributions of multiple electronic states and is spread in form of a wave packet over PES of these states. To mimic this behavior of the nuclear wave function in AIMD simulations, in practice, not one but an ensemble of trajectories is used. As the individual trajectories are propagated in the framework of classical mechanics, however, quantum effects such as tunneling are missing and, e.g., the coherence between electronic states is not described correctly, although there exist corrections for the latter.[101]

Originally, surface hopping included only NACs between electronic states of the same spin multiplicity and, thus, could be used only to study IC processes. To simulate also ISC, one has additionally to include SOCs between the electronic states of different spin multiplicity. This has been realized only recently in several different implementations.[71,102–105] It is done by adding a SOC operator $\hat{\mathcal{H}}^{\mathrm{SOC}}$ (see section 2.3.6) to the spin-free electronic Hamiltonian $\hat{\mathcal{H}}^{el}$, which is sometimes also called molecular Coulomb Hamiltonian $\hat{\mathcal{H}}^{\mathrm{MCH}}$.[106] The new, total electronic Hamiltonian then reads

$$\hat{\mathcal{H}}^{\mathrm{total}} = \hat{\mathcal{H}}^{\mathrm{MCH}} + \hat{\mathcal{H}}^{\mathrm{SOC}}. \tag{2.67}$$

The total electronic Hamiltonian $\hat{\mathcal{H}}^{\mathrm{total}}$ is not diagonal in the basis of the MCH states $\left|\Psi_i^{MCH}\right\rangle$. The off-diagonal couplings elements, that are due to SOC, can be considerably delocalized in the basis of the MCH states. This leads to non-zero ISC hopping probabilities between states of different spin multiplicity in extended regions of the PES, far away from the crossing regions of these states. This behavior is in contrast to that of the NACs that enable IC by coupling electronic states of same spin multiplicity: the NACs are only sizable in the vicinity of CIs. The SOCs can be localized by a unitary transformation $\mathbf{U}^\dagger\mathbf{U} = \mathbf{1}$ that transforms the electronic states into a basis that diagonalizes the total Hamiltonian, i.e.,

$$\mathbf{H}^{\text{diag}} = \mathbf{U}^\dagger\mathbf{H}^{\text{total}}\mathbf{U}. \tag{2.68}$$

In this new basis, the couplings between all states are described by the nonadiabatic couplings $\mathbf{K}^{\text{diag}}$ between the diagonal states; these NACs are localized only in the regions where the electronic states come close in energy. Performing surface hopping in this diagonal basis is the main idea of the surface hopping including arbitrary couplings (SHARC) method that is used in this work.[71,72,106]

2.5.2 Prerequisites for Surface Hopping Studies

The successful performance of surface hopping studies of excited-state dynamics relies on two key ingredients. Firstly, the outcome of surface hopping simulations crucially depends on the choice of the electronic-structure method that is used to calculate the PESs in which the classical trajectories move. The electronic structure method should be able to describe the PESs of all electronic states included in the dynamics simulations accurately, while being computationally affordable for dynamics simulation. Thus, to assess the accuracy of one electronic-structure method before employing it in the dynamics simulations, its performance can be tested in static calculations and compared against experimental reference data such as absorption or fluorescence spectra. Alternatively, one can compare against computational results from higher-level electronic-structure methods. Typically, the computationally most expensive part during the propagation of AIMD trajectories lies in the calculations of the electronic states and their gradients that need to be repeated each time step. It is the task of the theoretical chemist to find a method that guarantees a balance between accuracy and computational cost.

Secondly, the outcome of surface hopping simulations depends on a proper sampling of initial conditions, i.e., initial nuclear coodinates and momenta, for the trajectories. An appropriate sampling of nuclear conformations reflects the ensemble of nuclear geometries that the molecule can occupy in experiment at the moment it is excited, while an appropriate sampling of nuclear momenta lets the nuclei move with the appropriate velocities over the different electronic PESs. Additionally, appropriate initial conditions give the molecule the correct potential and kinetic energies, that determine both, which regions of the PESs the molecule can visit during the dynamics and how fast the molecule can molecule can transfer between these regions. Finally, the proper initial conditions should allow for a number of trajectories to be propagated in the dynamics simulation, that is sufficiently large to establish statistically significant statements about the reaction pathways and reaction rates of the ensemble.

3 Vibrational Sampling

This chapter deals with vibrational sampling: a method to account for the vibrational motion of the nuclei of the molecule in its electronic ground state. The fact that the molecule experiences vibrational motion explains the different nuclear conformations and momenta that comprise the initial conditions used in surface hopping simulations: as the molecule moves in its electronic ground state, it can occupy different nuclear conformations and momenta in the moment of excitation, i.e., when the dynamics start. Thus, vibrational sampling is routinely employed in surface hopping studies. However, accounting for the effects of nuclear motion through vibrational sampling can also be critical when studying static excited-state properties such as absorption spectra, and this is the focus of this chapter. The effects of different vibrational sampling techniques on excited-state dynamics will be presented later on in Chapter 5.

3.1 The Effects of Vibrational Sampling on Excited States

When studying static excited-state properties, the most common practice is to neglect nuclear motion and perform the excited-state calculations only at selected nuclear conformations. When, for example, absorption spectra are studied, the electronically excited states are computed typically only at the ground-state minimum-energy geometry (FC geometry). Naturally, to neglect the vibrational motion of the molecule greatly reduces the computational effort, which allows the usage of expensive high-level electronic structure methods. The resulting excitation energies and oscillator strengths computed in this approach are then usually compared to the positions and intensities of the experimental absorption band maxima. Often, a good agreement between these properties is indeed the result of an adequate description of the ensemble of molecules measured in the absorption spectrum by the properties of a single nuclear conformation. As will be shown below, however, there are unfortunate cases where this agreement can lead to completely wrong conclusions. Then, only by including nuclear motion through vibrational sampling, meaningful results can be obtained for the description of the electronic structure of excited states.

3.1.1 The Character of the Excited States of Nitrobenzene

Nitrobenzene shows a complex variety of photophysical and photochemical reactions upon excitation including various photodissociation processes[107–113] and ISC within 6 ps.[14,15,17] It can be considered the smallest prototype of NPAHs,

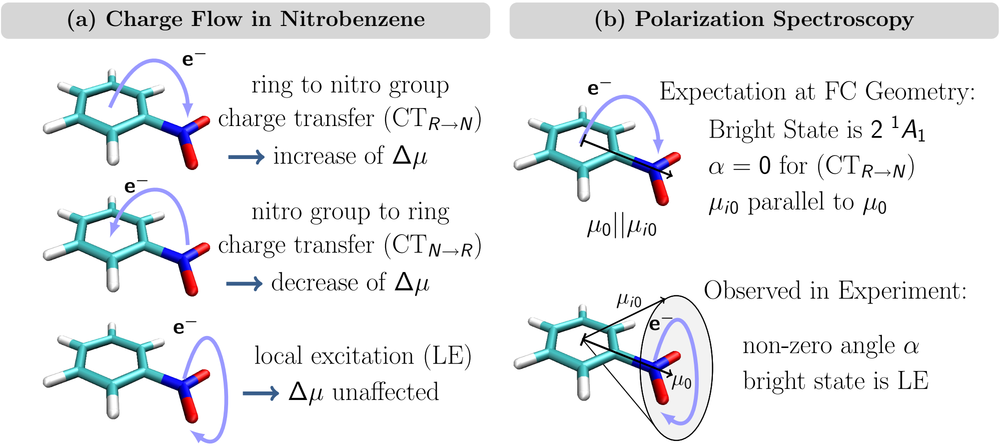
(a) Charge Flow in Nitrobenzene
(b) Polarization Spectroscopy
e$^-$
ring to nitro group
charge transfer (CT$_{R\rightarrow N}$)
⟶ increase of $\Delta\mu$
e$^-$
nitro group to ring
charge transfer (CT$_{N\rightarrow R}$)
⟶ decrease of $\Delta\mu$
e$^-$
local excitation (LE)
⟶ $\Delta\mu$ unaffected
e$^-$
Expectation at FC Geometry:
Bright State is 2 $^1A_1$
$\alpha = 0$ for (CT$_{R\rightarrow N}$)
μ_{i0} parallel to μ_0
$\mu_0 || \mu_{i0}$
μ_{i0}
e$^-$
μ_0
Observed in Experiment:
non-zero angle α
bright state is LE

Figure 3.1: (a) Characterization of excitations in nitrobenzene in terms of charge flow. Charge transfer defined as the difference between the excited-state and ground-state dipole moments, i.e., $\Delta\mu = \mu_i - \mu_0$. (b) Illustration of ground-state and transition dipole moment for the bright CT$_{R\rightarrow N}$ state at the FC geometry and as observed in polarization spectroscopy experiments.[118,119] α denotes the polarization angle.

for which reason it was chosen as the first molecule to be studied in this thesis. The excited-state properties of nitrobenzene have been investigated extensively in the past, both in experimental[114–121] and theoretical[16,121–123] studies. Surprisingly, despite its simple structure, there still remained controversy about the electronic character of its lowest-energy bright excited state. In absorption spectroscopy experiments, it was observed that the lowest-energy absorption band showed a solvent-induced red shift with increasing solvent polarity.[115] Thus, this band was first assigned to a charge-transfer (CT) $\pi\pi^*$ excitation from the aromatic ring system to the nitro group (CT$_{R\rightarrow N}$). Further experimental studies backed this conclusion[117,121] and high-level quantum chemical calculations could support this assignment, reporting that the only bright state in the energy region of the absorption band at the FC geometry was a $\pi\pi^*$ state of CT$_{R\rightarrow N}$ character, that is of $^1A_1$ symmetry at the C_{2v}-symmetric minimum-energy geometry.[121,123] This assignment was questioned, however, by polarization spectroscopy experiments.[118,119] In these experiments the angle α between the ground-state dipole moment μ_0 and the bright-state transition dipole moment μ_{i0} can be determined, which gives directly information about the symmetry of the excited-state wave function (see Figure 3.1). For the 2 $^1A_1$ state, the angle α had to be zero due to symmetry. Yet, the polarization spectroscopy experiments determined a value $\alpha = 67°$, i.e., ruling out that the lowest-energy absorption band is described by the 2 $^1A_1$ state. In lieu of a better explanation, the absorption band was assigned to a local $\pi\pi^*$ excitation (LE) at the nitro group.

Motivated by the ambiguous findings of the previous studies and the aim to find a suitable method for an accurate description of the excited states of nitrobenzene, the absorption spectrum was investigated in this work. The absorption spectra of nitrobenzene in gas phase and aqueous solution were computed for different vibrational ensembles and at the FC geometry. The vibrational ensembles were generated using a sequential combination of molecular mechanics and quantum mechanics (s-MM/QM) calculations to include the effects of vibrational motion on the description of the electronic states.[124–126] In this approach, first, ground-state molecular dynamics (MD) trajectories using classical force fields were propagated for nitrobenzene in three different environments: gas phase, a implicit solvation model (PCM[96]), and an explicit solvation model (TIP3P[127]). In the MD simulations, nitrobenzene was described by the generalized Amber force field (GAFF[128]). From each trajectory, 200 nuclear conformations were randomly selected, and for each conformation the excited state were calculated at the MS-CASPT2[129]/ANO-L-VDZP[130] level of theory. For each vibrational ensemble, the results of the 200 geometries were then combined to yield the full absorption spectra in gas phase, implicit, and explicit aqueous solution.

3.1.2 Quenching of Charge Transfer by Vibrational Motion

The absorption spectra calculated using the s-MM/QM approach, the experimental absorption spectra, and the bright states calculated at the FC geometry are shown in Figure 3.2(a). As can be seen, the energies of the bright states at the FC geometry are close to the absorption band maxima in gas phase as well as in aqueous solution, indicating that CASPT2 can accurately describe the excited states of nitrobenzene. A wave-function analysis of the bright states at the FC geometry (S_4@FC) in gas phase and water reveals that they are mainly described by $\mathrm{CT}_{R\to N}$ excitations (ca. 95 % of the examined configurations). Nitro group to ring charge transfer ($\mathrm{CT}_{N\to R}$) excitations and local excitations (LE) possess only minor contributions of 3.5 and 1.5 %, respectively. This composition of the excited-state wave function, illustrated in form of a pie chart in Figure 3.2(b), indeed results in a large CT in nitrobenzene upon excitation in both, gas phase and aqueous solution. The CT can be measured quantitatively by the difference between the excited-state and ground-state dipole moments, i.e., $\Delta\mu = \mu_i - \mu_0$, which amounts to 6.5 and 7.8 D in gas phase and water, respectively. The difference $\Delta\mu$ has also been assessed in a experimental study of thermochromic effects in the absorption spectra of nitrobenzene in 1,2-dichlorethane, where $\Delta\mu$ was determined to be 2.1-2.4 D.[120] Based on this result, the CT character in the excited states of the absorption spectrum of nitrobenzene appears to be overestimated, when only the bright states at the FC geometry are considered. Additionally, due to the A_1 symmetry of the bright S_4@FC state, the polarization angle α between the ground-state and transition dipole moment is zero, in stark contrast to polarization spectroscopy result of $\alpha = 67°$.

In Figures 3.2(a), also the s-MM/QM absorption spectra are shown. Compared to the experimental absorption bands, the maxima at 245 (gas phase), 276 (implicit aqueous solution), and 282 nm (explicit aqueous solution) agree well with the experimental positions at 240 (gas phase) and 266 nm (water).

(a) Absorption Spectra

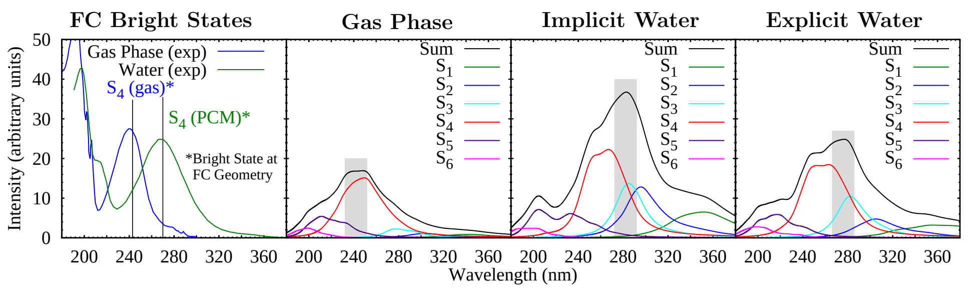

(b) State Character

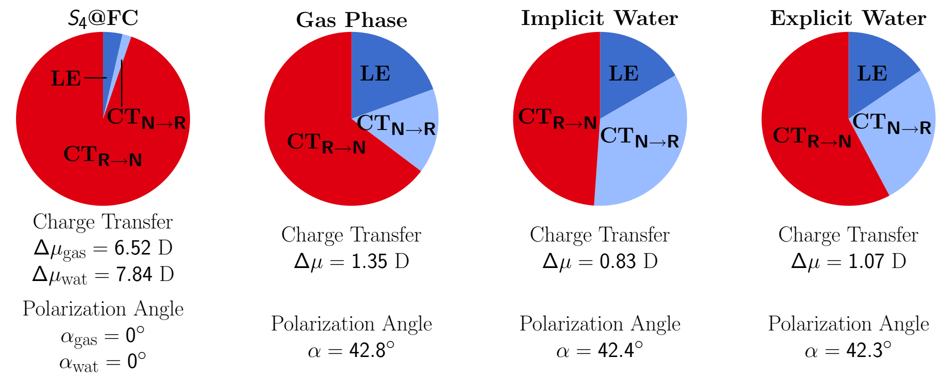

Figure 3.2: (a) Experimental[115] and calculated absorption spectra as well as bright states of nitrobenzene computed at the FC geometry. (b) Character of FC bright states and states within a 20 nm energy range [gray areas in (a)] around the computed absorption maxima. The area of the slices in the pie chart corresponds to the contribution of $CT_{R\to N}$, $CT_{N\to R}$, and LE configurations in the excited-state wave functions. The bright S_4 states in gas phase and water possess very similar character, thus, only one chart is shown.

This supports the previous conclusion that CASPT2 is able to accurately describe the excited states of nitrobenzene. As the positions of the calculate absorption band maxima also agree well with the energy of the bright S_4@FC states –243 and 270 nm in gas phase and water, respectively –it is tempting to assume that the S_4@FC also possess the same electronic character as the corresponding bright states in the s-MM/QM ensembles with similar energies. This assumption, however, proves to be wrong.

When analyzing the excited states around the absorption band maxima in the s-MM/QM ensembles [gray areas in Figure 3.2(a)], one finds that the excited states in the s-MM/QM ensembles possess quite different character from that of the S_4@FC. This is shown in Figure 3.2(b) where the composition of the excited states around the absorption maximum is expressed in terms of contributions of $CT_{R\to N}$, $CT_{N\to R}$, and LE configurations. Both in gas phase and aqueous solution, the contributions of $CT_{R\to N}$ configurations are decreased considerably compared to the S_4@FC states –from 95 % to 50-65 %. The $CT_{R\to N}$ con-

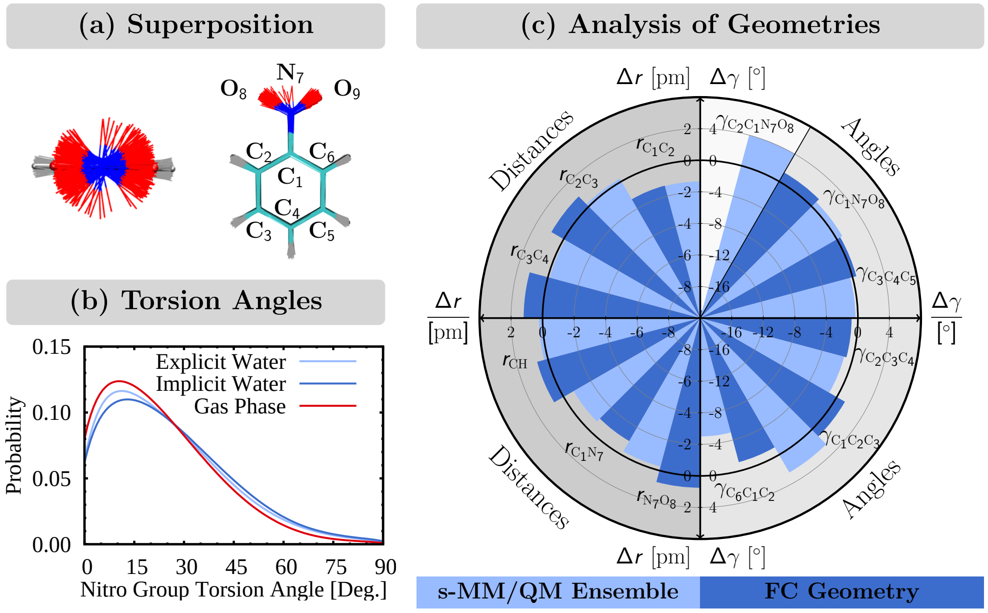

Figure 3.3: (a) Superposition of the 200 geometries from the s-MM/QM ensemble in explicit aqueous solution and atom numbering of nitrobenzene. (b) Distribution of nitro group torsion anlges for the geometries in the three s-MM/QM ensembles. (c) Differences of important structural parameters between an experimental gas phase structure[111] and the B3LYP/cc-pVDZ FC geometry as well as the gas-phase s-MM/QM ensemble.

tributions are replaced by contributions of $\mathrm{CT}_{N\rightarrow R}$ configurations (16-34 %) and LE configurations (16-20 %) instead. Because of this, the excited states in the s-MM/QM ensembles are described by an admixture of $\mathrm{CT}_{R\rightarrow N}$ and $\mathrm{CT}_{N\rightarrow R}$ configurations, i.e., configurations with charge flow in opposite directions. This opposing charge flow effectively quenches the net CT, e.g., reducing the differences in dipole moments to $\Delta\mu = 1.3$ and 0.8-1.1 D in gas phase and aqueous solution, respectively. The admixture of different configurations also changes the direction of the transition dipole moment, so that for the states in s-MM/QM ensembles, the polarization angle between the ground-state and transition dipole moment is $\alpha = 42$-$43°$. Both, the values of $\Delta\mu$ and α obtained for the s-MM/QM ensembles are much closer to the values obtained in experiment[118–120] than those of the S_4@FC states. This demonstrates the necessity to take into account the vibrational motion present in experiment also when calculating static excited-state properties.

Concluding this study, it is interesting to analyze the motion responsible for changing the character of the electronic states when going from the FC geometry to the s-MM/QM ensemble. For this, the superposition of the 200 geometries of the s-MM/QM ensemble in explicit aqueous solution is shown in Figure 3.3(a). It is apparent that the main deviation from the planar FC geometry is the torsional rotation of the nitro group, while the atoms of the aromatic ring system nearly stay in the same plane. Therefore, it is this torsional motion that is responsible for the change of electronic character that is observed in the excited states in the absorption spectrum compared to the bright state at the FC geometry.

The vast majority of geometries of the s-MM/QM ensembles are non-planar. The distribution of nitro group torsional angles γ of the ensembles shown in Figure 3.3(b) reveals that only as little as 15-20 % of all geometries possess torsional angles γ smaller than $10°$. In average, the s-MM/QM geometries possess a torsional angle of $\langle\gamma\rangle \approx 25°$, thus, deviating considerably from the planar FC geometry. Note that in the distribution of torsional angles in Figure 3.3(b), γ ranges only between 0 and $90°$. This takes into account interchangeability of the oxygen atoms of the nitro group making structures with γ and $\gamma + 180°$ identical, and it does not distinguish between enantiomeric rotamer pairs that possess torsional angles of $+\gamma$ and $-\gamma$, since the properties of these enantiomers would only differ when using polarized light for excitation. Thus, it is more useful to define γ only in the interval $[0, 90°]$.

Finally, it is interesting to compare the structures of the ensemble with experimental reference data, to examine how well the classical MM calculations can model the experimental structure. For this, the averages of the most important structural parameters of the s-MM/QM gas phase ensemble are compared with the values of an experimental gas-phase structure[111] in Figure 3.3(c). As can be seen, the errors of bond distances are of the order of 1 pm, and also all angles of the ensemble structures agree in average well with the experimental reference. This also applies to the average torsional angle, which is $\langle\gamma\rangle = 24°$ for the gas phase s-MM/QM ensemble compared to the experimental value of $\langle\gamma\rangle = 20°$. Note that $\langle\gamma\rangle$ was also determined by using the above considerations that restrict γ to the range $[0, 90°]$.

For comparison, in Figure 3.3(c), additionally the differences between the experimental gas phase sturcture and the B3LYP/cc-pVDZ optimized FC geometry are shown. Also the B3LYP/cc-pVDZ-optimized FC geometry shows only small deviations in the bond lengths and most angles agree well with the experimental reference data. However, at the FC geometry, the torsional angle γ is zero, deviating largely from the experimental average of $\langle\gamma\rangle = 20°$. This is not an error of the geometry optimization which predicted the correct minimum-energy structure. Rather, both values represent different quantities, as the experiment measures an ensemble of molecules with different nuclear conformations, and not a single molecule at the mimimum-energy geometry. The difference between the $\langle\gamma\rangle$ values shows that the single-geometry approach cannot always capture all important geometrical features of the molecule. As shown for the case of nitrobenzene, the single-geometry approach can give a erroneous description of its electronic structure, that can be corrected for by considering its vibrational motion, e.g., in form of vibrational sampling.

The results obtained in this section have been published in the study “Quenching of Charge Transfer in Nitrobenzene Induced by Vibrational Motion” in the Journal of Physical Chemistry Letters.[131]

3.2 Quantum and Classical Phase-Space Sampling

The previous section presented an example of the importance of the effects of the nuclear motion on the electronic properties of a molecule. This motion can be included in static calculations through vibrational sampling, by selecting geometries that the molecule can occupy during its vibrational motion. This vibrational sampling can also be used to generate initial conditions for surface-hopping simulations, where, however, one needs to sample also nuclear momenta in addition to the molecular geometries. The multitude of combinations of nuclear coordinates and momenta comprises the so-called phase space of the molecule, and, thus, the sampling of both coordinates and momenta is referred to as phase-space sampling.

For phase-space sampling, there exist classical and quantum approaches (see Figure 3.4). In classical sampling methods, one either performs MD simulations[132] in the electronic ground state and selects a sample of nuclear conformations with associated momenta from the trajectories, or one performs stochastic Monte-Carlo simulations.[133] The simulations are performed for the molecule at a given temperature T, all the degrees of freedom of the molecule are assumed to be in thermal equilibrium. Thus, these classical sampling methods are also referred to as thermal or finite-temperature sampling.[134]

In quantum phase-space sampling, one considers the Wigner function W,[135] which for a quantum system of f degrees of freedom reads in its coordinate representation

$$W[\Psi](\mathbf{q},\mathbf{p}) = \left(\frac{1}{2\pi\hbar}\right)^{f} \int \mathrm{d}\mathbf{s}\; \Psi^{*}(\mathbf{q}-\mathbf{s}/2)\, \mathrm{e}^{\mathrm{i}\mathbf{p}\cdot\mathbf{s}/\hbar}\, \Psi(\mathbf{q}+\mathbf{s}/2). \tag{3.1}$$

The Wigner function W is a representation of the density matrix of the system[136] and it serves as a (quasi-) probability distribution for the coordinates $\mathbf{q}$ and momenta $\mathbf{p}$ of the particles in the system. It depends on the wave function Ψ, that, for vibrational sampling, is the wave function of the nuclei. As the nuclear wave function is a complex quantity depending on the complete electronic PES, it is never calculated in an exact manner. Instead, each nuclear degree of freedom is considered independently, and its potential is assumed to be harmonic around the minimum-energy point, the FC geometry. In this way, the vibrational motion of the molecule is approximated by independent harmonic oscillators, for which analytical expressions for the wave functions are known. In practical applications, the harmonic oscillators are furthermore often restricted to the vibrational ground state, which corresponds to the hypothetical model system of the molecule at zero temperature. Thus, quantum or Wigner sampling is also referred to as zero-temperature sampling.[134] However, as will be discussed later on, it is also possible to perform Wigner sampling at finite temperatures by including vibrationally excited states.

Both sampling approaches, thermal and Wigner sampling, differ in a few important aspects that affect their performance and applicability. In thermal sampling, the molecule is in thermal equilibrium at a given temperature T so that each degree of freedoms in average possesses approximately the thermal energy

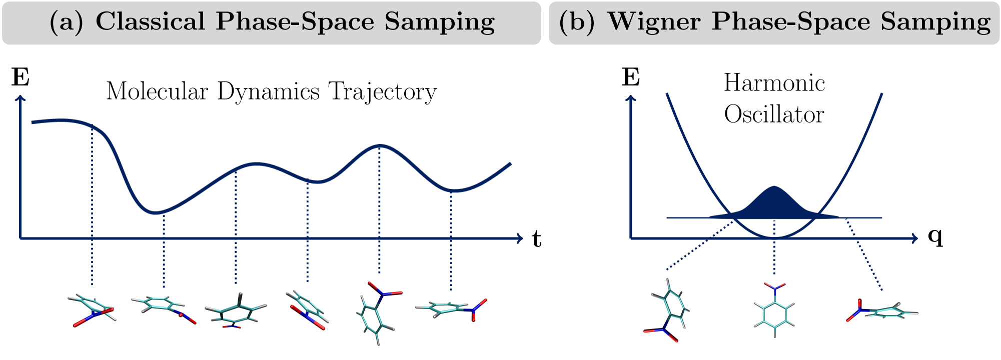
(a) Classical Phase-Space Samping
(b) Wigner Phase-Space Samping
E
Molecular Dynamics Trajectory
t
E
Harmonic Oscillator
q

Figure 3.4: Phase-space sampling from (a) a classical molecular dynamics trajectory by selecting snapshots at random time intervals or from (b) a quantum-mechanical Wigner distribution of a harmonic oscillator.

$\langle\varepsilon\rangle = k_B T$ (in the high-temperature limit). In contrast, in zero-temperature Wigner sampling, each degree of freedom possesses its individual zero-point energy (ZPE) $\varepsilon_i = {}^1\!/\!{}_2\,\omega_i$ depending on the frequency ω_i of the vibration. Neither of these approaches really account for the total energy of the molecule, which is actually the sum of ZPE and a thermal-energy contribution. However, the zero-temperature Wigner sampling usually captures a larger fraction of the total energy as ${}^1\!/\!{}_2\,\omega_i > k_B T$ for most vibrational modes in molecules at low or moderate temperatures, e.g., 300 K. An exception represent low-frequency vibrational modes, such as torsions or stretching modes in weakly-bonded cluster systems, where the thermal-energy contribution $k_B T$ is larger than the ZPE of ${}^1\!/\!{}_2\,\omega_i$. Then, thermal sampling gives a better estimate of the total energy. Wigner sampling can also become inferior to MD-based thermal samlping when the PES diverges from its assumed harmonic form. In particular, extended molecular systems or molecules embedded in an environment can possess a larger number of low-frequency vibrational modes with rather anharmonic potentials. The anharmonic features of the potentials can be captured well in thermal sampling when the underlying MD simulations are performed quantum mechanically or by mixed QM/MM schemes. However, also the potentials in purely classical MD simulations account for some effects of anharmonicity through the inclusion of the non-bonded Coulomb and van-der-Waals interactions .

The sampling approaches also differ in their computational cost. For small-sized molecular systems, Wigner sampling is computationally less expensive than thermal sampling. This is because Wigner sampling requires only a geometry optimization to find the minimum-energy structure and a subsequent frequency calculation in the harmonic oscillator approximation, which is a smaller effort in contrast to the many calculations performed during the MD simulation. For large systems, however, Wigner sampling is not feasible because the frequency calculation becomes unaffordable, which leaves thermal sampling as the method of choice. When the large system is subdivided into parts, there exists also a hybrid approach combining Wigner and thermal sampling.[137] In this approach, first, a Wigner ensemble is generated for a small part of the system. The resulting geometries are then placed in the remaining part of the system, e.g., the environment, and kept frozen during a subsequent MD simulation to allow the environment to adapt to the individual structures of the small region.

3.3 Performance of Different Sampling Models

After the study of nitrobenzene (section 3.1.1) revealed the importance of vibrational sampling for an accurate description of its electronic structure, it was interesting to investigate how these results transfer to other nitro aromatic compounds. Thus, studies on 2-nitronaphthalene (2NN) were conducted. Nitronaphthalene derivatives contribute largely to the overall air mutagenicity caused by NPAHs.[138] For three of them –1-nitronaphthalene (1NN), 2NN, and 2-methyl-1-nitronaphthalene (2M1NN)– ultrafast ISC has been observed in experiment,[2,4,6,11,13,139] making these molecules interesting objects in the framework of this thesis. 1NN and 2M1NN exhibit photodegradation upon UV-VIS irradiation while 2NN is photostable[13], suggesting that the photodynamics of the latter compound are less complicated. For this reason, 2NN was selected as the first nitronaphthalene derivative to study.

The electronic structure of 2NN was studied by investigating its absorption spectrum in methanol (MeOH). The results presented in this section are currently submitted for publication in a manuscript titled "Vibrational Sampling and Solvent Effects on the Electronic Structure of the Absorption Spectrum of 2-Nitronaphthalene".[140] Note that a similar study on the different performance of Wigner and MD sampling has been published for pyrrole.[134] There, the focus was laid on the effects that the different sampling methods have on the outcome of excited-state dynamics of pyrrole in the gas phase through their use in generating the initial conditions for the dynamics. In contrast, in this work, the focus lies on the effects of vibrational sampling and the presence of a solvent on the energies and wave-function characters of the electronic states in the absorption spectrum.

3.3.1 The Absorption Spectrum of 2-Nitronaphthalene

To investigate the absorption spectrum of 2NN in MeOH, four different vibrational sampling approaches have been employed to generate vibrational ensembles: Wigner/COSMO, Wigner/MM, MD/COSMO, and MD/MM. The ensembles are generated from a Wigner distribution or thermal sampling based on MD simulations, and the presence of the solvent was modeled by either an implicit continuum solvent model (COSMO[97]) or by an explicit solvent model, where the solvent molecules were described by classical MM point charges.[141] The Wigner sampling was performed at zero-temperature based on frequencies obtained at the B3LYP[142–145]/def2-TZVP[146] level of theory, while the MD simulations were run at $T = 300$ K at the B3LYP[142–145]/def2-SVP[146] level of theory. From each ensemble, 100 geometries were selected and 20 excited states were calculated, using different electronic structure methods. Additionally, the

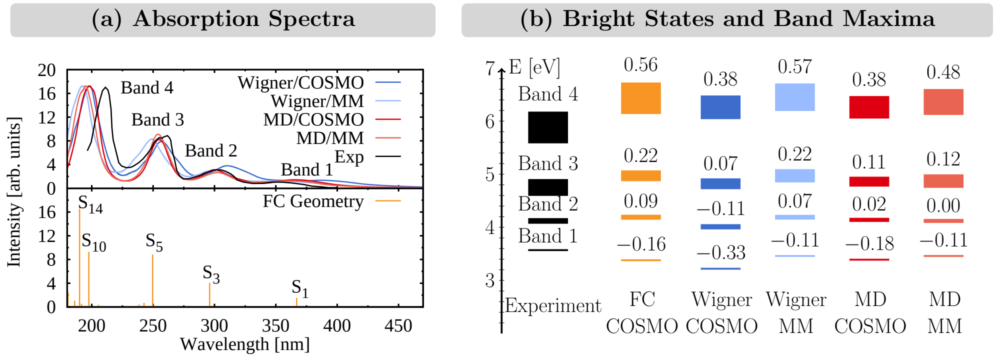
(a) Absorption Spectra

(b) Bright States and Band Maxima

Figure 3.5: (a) Experimental[148] and computed absorption spectra as well as excited states at the FC geometry of 2-nitronaphthalene in MeOH. Excited states computed at the PBE0/def2-TZVP level of theory. (b) Comparison of the energies and intensities of the band maxima and bright states from (a). The height of the blocks corresponds to the intensity of the band/state, while the labels denote the energy difference to the experimental results.

excited states were computed at the B3LYP/def2-TZVP-optimized FC geometry. Different electronic structure methods were employed, however, as the best agreement with experimental reference data was obtained using TDDFT at the PBE0[147]/def2-TZVP[146] level of theory, only these results are discussed here.

The excited states at the FC geometry as well as the computed and experimental[148] absorption spectra of 2NN in MeOH are shown in Figure 3.5(a). As can be seen, including 20 electronically excited states in the calculations captures all excited states in the wide energy range of 180-450 nm. The experimental absorption spectrum displays four absorption bands in this range. Overall, the spectra computed by the different sampling approaches agree well with the experimental spectrum, as they describe all four bands well in terms of both, energies and intensities. This is better appreciated in Figure 3.5(b) where the excitation energies and intensities of the maxima of the experimental and computed absorption bands are compared. The energy differences between the experimental and calculated band maxima ΔE are typically less than 0.2 eV except for the highest-energy absorption band where $\Delta E = 0.4$-0.6 eV, and the intensities at the maxima are very similar.

Interestingly, the band maxima are blue-shifted when changing the solvent model from COSMO to MM. This blue shift is ca. 0.2 eV for the Wigner ensembles, while it is ≤ 0.1 eV for the MD ensembles. When comparing Wigner and MD ensembles for a given solvent model, no clear trend in the energies is visible: the Wigner/COSMO bands are at higher energy than the MD/COSMO bands while the Wigner/MM bands are at lower energies compared to the MD/MM bands. Overall, the smallest average energy differences of all bands compared to experiment is found for the MD/MM ensemble (0.17 eV), suggesting that the MD/MM combination is slightly superior to the other sampling methods. Yet, it is fair to say, that also the other sampling methods perform comparatively well. Importantly, however, there is a larger difference between the bright states of the vibrational ensembles and the bright states at the FC geometry, thus, highlighting again the importance to account for vibrational motion.

3.3.2 Influence of Vibrational Motion

The stick spectrum of the excited states calculated at the FC geometry is shown in the lower panel of Figure 3.5(a), where only the bright states are labeled. As can be seen, in each energy range of the first three absorption bands, only one bright state is present (S_1, S_3, S_5), while there are two bright states (S_{10}, S_{14}) close in energy to band 4. This conveniently suggests that the absorption bands may be described solely by these states. To better compare to the experimental and calculated absorption bands of the vibrational ensemble, the energies and intensities of the FC bright states are drawn in Figure 3.5(b), where for comparing to band 4, the energies of the states S_{10} and S_{14} were averaged while their intensities were added. Comparing to the experimental absorption band maxima, the FC bright states show similar intensities, and the energetic differences are only 0.1-0.2 eV for bands 1-3, while it is 0.56 eV for band 4. These differences are similar to the energy differences between the calculated and experimental absorption band maxima, however, overall, the average differences are larger for the FC bright states than for the computed absorption bands.

The comparison of FC bright states with the experimental absorption bands assumes that the absorption bands can be described solely by the FC bright states, i.e., the bright states do not mix with other states that are dark at the FC geometry. To test this assumption, a transition-density-matrix analysis[87–90] (see section 2.3.5) of the computed absorption bands and FC bright states was performed to compare their electronic character. The results are depicted in Figure 3.6 which shows the hole-electron (h/e) difference populations, charge-transfer numbers (CT), and exciton sizes (ES) of the FC bright states and the corresponding average quantities of the states of each individual absorption band. The averaging includes weighting each state's contributions by its oscillator strength. For this comparison, only results of the Wigner/COSMO ensemble are shown; since there the same solvent model is used and sampling is performed centered around the FC geometry, comparing these results to the FC bright states is expected to give the most reasonable assessment of the effects of vibrational motion.

As can be seen in Figure 3.6, the properties of the bright states S_1 and S_3 agree well with those of bands 1 and 2, respectively. The h/e difference populations show very similar electronic transitions with a pronounced charge flow from the aromatic ring [large (blue) hole populations] to the nitro group [large (red) electron population], resulting in large CT numbers and exciton sizes in both, the FC bright states and the absorption bands. Thus, both band 1 and 2 comprise mainly excited states of S_1 and S_3 character, respectively. Comparing band 3 and FC bright state S_5, one can observe notable differences. While the S_5 state shows large h/e differences populations –meaning that the hole and electron part of the transition density are located on different atoms –the average h/e differences populations in band 3 are much smaller. This

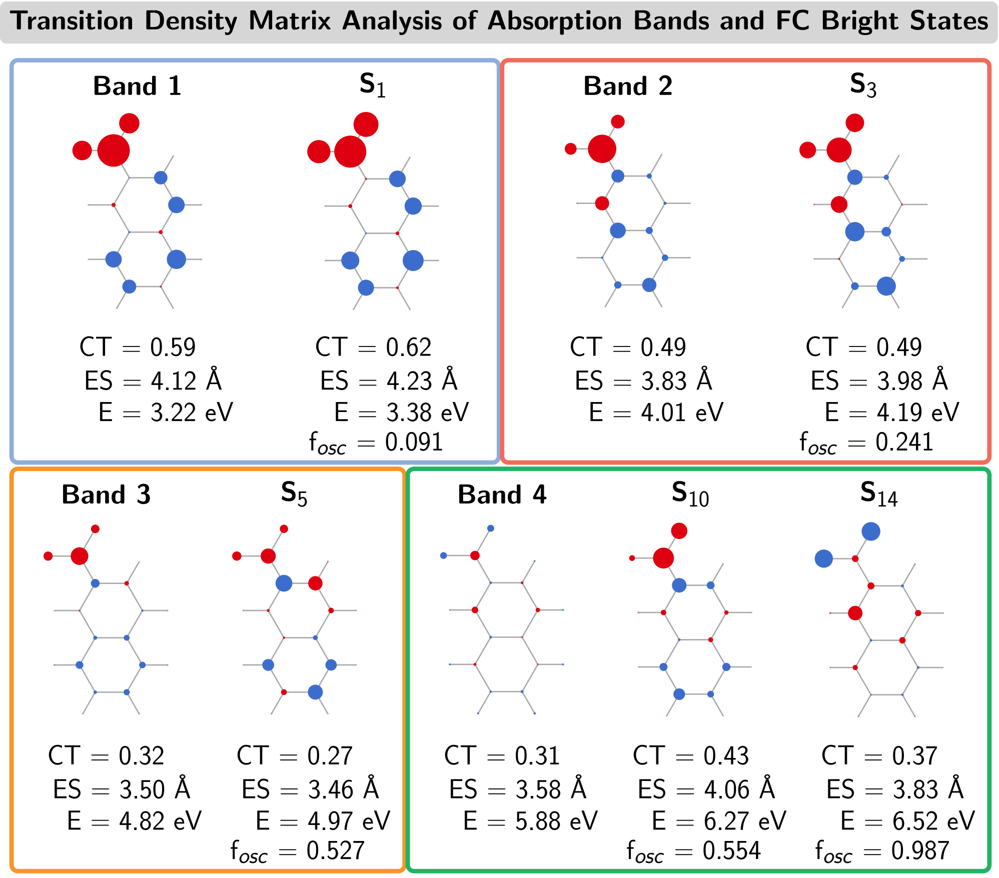
Transition Density Matrix Analysis of Absorption Bands and FC Bright States
Band 1
S$_1$
CT = 0.59
ES = 4.12 Å
E = 3.22 eV
CT = 0.62
ES = 4.23 Å
E = 3.38 eV
f$_{osc}$ = 0.091
Band 2
S$_3$
CT = 0.49
ES = 3.83 Å
E = 4.01 eV
CT = 0.49
ES = 3.98 Å
E = 4.19 eV
f$_{osc}$ = 0.241
Band 3
S$_5$
CT = 0.32
ES = 3.50 Å
E = 4.82 eV
CT = 0.27
ES = 3.46 Å
E = 4.97 eV
f$_{osc}$ = 0.527
Band 4
S$_{10}$
S$_{14}$
CT = 0.31
ES = 3.58 Å
E = 5.88 eV
CT = 0.43
ES = 4.06 Å
E = 6.27 eV
f$_{osc}$ = 0.554
CT = 0.37
ES = 3.83 Å
E = 6.52 eV
f$_{osc}$ = 0.987

Figure 3.6: Transition-density-matrix analysis of the average properties of the absorption bands of the Wigner/COSMO ensemble and the FC bright states. Molecule representations show the atomic hole-electron difference populations (blue: positive; red: negative). CT and ES denote charge-transfer number and exciton size, respectively. For computing the CT, the molecule has been partioned into two fragments, the nitro group and aromatic ring system. Energy E of the bands correspond to the positions of the absorption band maxima. f_{OSC} is the oscillator strength.

indicates that additional states, that are dark at the FC geometry, mix with the S$_5$ state at the geometries included in the Wigner/COSMO ensemble. The mixing of additional dark states with the bright FC states becomes even more pronounced in the case of band 4. Here, the h/e population show only a weak resemblence to the ones of bright states S$_{10}$ and S$_{14}$. For example, the negative h/e population at the nitrogen atom or the positive h/e populations at the oxygen atoms that are characteristic features of the S$_{10}$ and S$_{14}$, respectively, are much smaller in band 4. Furthermore, the CT number and exciton size of band 4 are much smaller than that of either FC bright state, thus, proving that additional electronic states contribute to the band 4 when nuclear motion is included in the calculations.

While bands 1 and 2 display the same electronic properties as the states S_1 and S_3, and band 3 shows only minor contributions of states other than the S_5, there is one important difference between these bands and their corresponding FC brights states: the absorption bands are red-shifted from the FC bright states. Comparing the energies of the bright states with the positions of the maxima of bands 1-3 (Figure 3.6), this shift amounts to 0.15-0.20 eV. For band 4, the maximum is shifted even further from states S_{10} (0.39 eV) and S_{14} (0.64 eV), which, however, is also due to the pronounced admixture of other states that are dark at the FC geometry, as has been discussed above. The red-shift found for the ensemble is induced by the vibrational motion of the molecule. To demonstrate this, in Figure 3.7(a), the energies of the excited states in the absorption bands of the Wigner/COSMO ensemble are shown as a function of the root-mean-square displacement (RMSD) of the atoms from the FC geometry in 2NN. As can be seen, all bands show a increasing red-shift when the RMSD increases, i.e., when a larger motion displaces the molecule farther away from its FC geometry.

As the red-shift of the absorption bands in the vibrational ensembles scales with the extent of nuclear motion, the red-shift is smaller for the MD/COSMO ensemble (~ 0.09 eV) than for the Wigner/COSMO ensemble (~ 0.17 eV) [see Figure 3.5(b)]. The overall motion of the molecule in the MD/COSMO ensemble is less pronounced than in the Wigner/COSMO ensemble due to the smaller vibrational energy that is available. While the total ZPE in 2NN is ca. 4.1 eV, the thermal energy in the high-temperature limit is only $E = (3N-6)k_BT = 1.4$ eV at 300 K. In particular, the motion-induced red-shift of the absorption bands is explained by the fact, that the increase of the ground-state energy, induced by the vibrational motion, is larger than the increase of the energies of the excited states. This is shown exemplarily for the absorption band 1 in Figure 3.7(b). While the energy of the ground states in the geometries of the Wigner/COSMO ensemble increases by 1.76 eV with respect to the energy at the FC geometry, those of the excited states belonging to absorption band 1 increases only by 1.43 eV, thus resulting in a red-shift compared to the excitation energy of the S_1 state at the FC geometry. For MD/COSMO, both the increases in the ground-state and excited-state energies are smaller than for Wigner/COSMO. As the increase is still larger for the ground states than the excited states, this still results in a red-shift of the absorption band, that is, however, also smaller than for Wigner/COSMO.

To examine the motion in the Wigner/COSMO and MD/COSMO ensembles, a superposition of all geometries is shown in Figure 3.5(c). Similar to the case of nitrobenzene (see section 3.1.2), also for 2NN, the largest difference between the ensemble geometries and the FC geometry is the out-of-plane torsion of the nitro group, while the atoms of the aromatic ring system nearly stay in the same plane. The nitro group torsion is more pronounced in the MD/COSMO ensemble than in the Wigner/COSMO ensemble. This is because the torsion is described by a low-frequency vibrational mode ($\omega = 56$ cm^{-1}), for which the ZPE is much smaller than the thermal energy. Therefore, the energy available for this motion is larger in the MD/COSMO ensemble than in the Wigner/COSMO ensemble, which increases the extent of the nitro group torsion

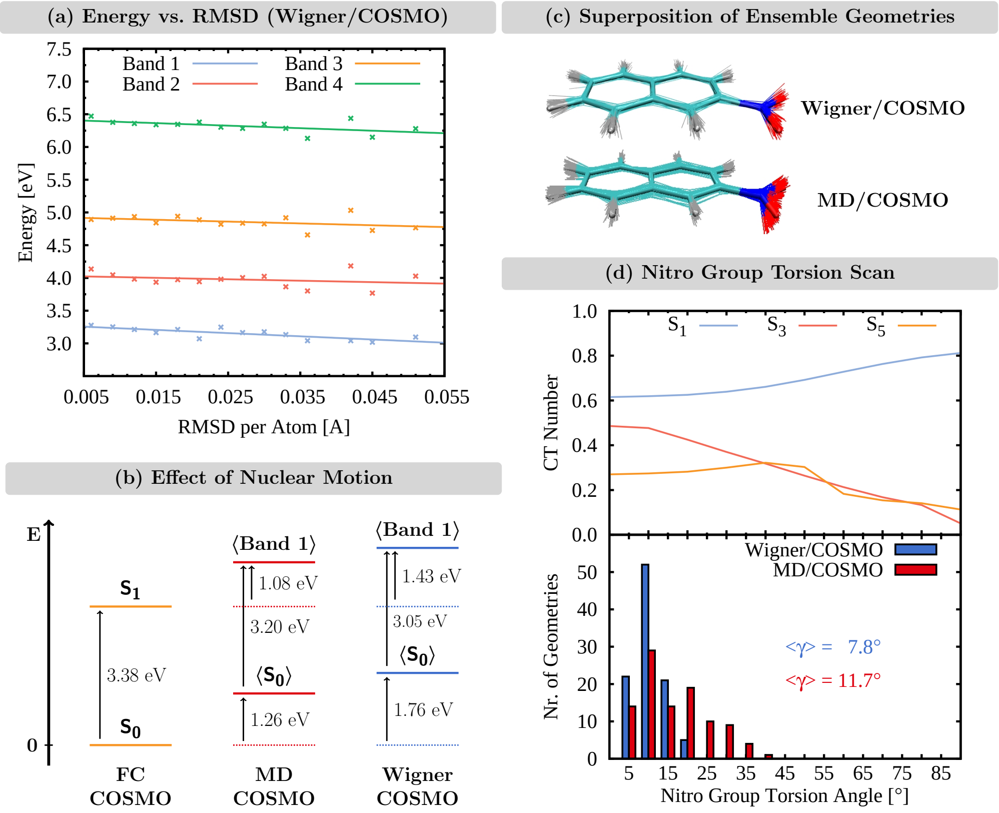

(a) Energy vs. RMSD (Wigner/COSMO)

(b) Effect of Nuclear Motion

(c) Superposition of Ensemble Geometries

(d) Nitro Group Torsion Scan

Figure 3.7: (a) Average energy of the excited states of each absorption band as a function of the atomic root-mean-square displacement (RMSD) of the Wigner/COSMO ensemble geometries. Average energies weighted by oscillator strengths of the contributing states. (b) Comparison of the energies of the S_0 and S_1 states at the FC geometry with the average energies of the S_0 state and band 1 for the MD/COSMO and Wigner/COSMO ensembles. Average energies weighted by oscillator strengths of the contributing states. (c) Superposition of the geometries of the Wigner/COSMO and MD/COSMO ensembles. (d) Variation of the charge-transfer (CT) number as well as probability distribution of the nitro group torsion angle γ of the MD/COSMO and Wigner/COSMO ensemble.

in the former ensemble. This can be seen in the bottom panel of Figure 3.7(d), where the probability distribution of the nitro group torsion angles is shown for the MD/COSMO and Wigner/COSMO ensembles. While all geometries in the Wigner/COSMO ensemble have torsional angles $\gamma < 20°$, the spread of γ is larger for the MD/COSMO ensemble reaching angles up to $\gamma = 40°$. The larger torsion does not possess a significant effect on the energies of the absorption bands –the larger red-shift from the FC geometry was observed for the Wigner/COSMO ensemble indicating that other vibrational displacements affect the energies –but it can change the electronic character of specific absorption bands. For example, the CT number of the absorption bands 1-3 for the Wigner/COSMO ensemble are 0.59, 0.49, and 0.31, respectively, while those of bands 1-3 for the MD/COSMO ensemble are 0.60, 0.41, and 0.31, respectively, i.e., the CT numbers of bands 1 and 3 are the same for both ensembles while the CT number of band 2 decreases when going from Wigner/COSMO to MD/COSMO. To understand this, the CT numbers of the states S_1, S_3, and S_5, i.e, main contributions to bands 1-3, are shown as a function of the nitro group torsion. As can be seen, the CT numbers of S_1 and S_5 do not vary much for torsion angles that are populated in either the MD/COSMO or Wigner/COSMO ensemble, i.e., when $\gamma \leq 40°$. Thus, the differences between the CT numbers of bands 1 and 3 in both ensembles and the CT numbers of the S_1 and S_5 states at the FC geometry are very small. The CT number of the S_3 state stays constant for values of $\gamma \leq 10°$ before it decreases with increasing γ. This decrease affects the CT number of band 2 in the Wigner/COSMO ensemble only weakly, as only few geometries possess a torsion angle $\gamma > 10°$. However, in the MD/COSMO ensemble, $\gamma > 10°$ for the majority of geometries, which effectively decreases the CT number of band 2 when compared with the S_3 state at the FC geometry. Thus, similarly to the case of nitrobenzene presented in section 3.1.1, charge transfer again is quenched by the nitro group torsion in the absorption band 2 of 2NN.

3.3.3 Influence of the Solvent Model

In addition to the effects of vibrational motion, also the influence of a solvent (MeOH) on the electronic properties of 2NN was investigated. For this, one implicit (COSMO) and one explicit (MM) solvent model were employed, both in the generation of the vibrational ensembles as well as in the excited-state calculations. In order to evaluate the influence of the solvent solely on the electronic structure of 2NN, gas-phase excited-state calculations were conducted for the solvent-equilibrated geometries of the ensembles and at the FC geometry.

In Figure 3.8(a), the energy differences between the bright states at the FC geometry in gas phase and in solution as well as the differences between the positions of the absorption band maxima in gas phase and in solution are shown. As can be seen, the bright states and absorption bands are nearly all red-shifted upon solvation. This red-shift is more pronounced when the COSMO solvent model is used, where it amounts, in average, to ca. 0.2 eV, while it is ca. 0.1 eV for the MM solvent model. The extent of the red-shift, however, depends on the bright state/absorption band. It is the largest for the first bright state/absorption band and subsequently becomes smaller when going higher in energy. Interestingly, the red-shifts dependence on both, the solvent model and the specific bright state/absorption band are interconnected as they depend on the CT character of the state/band.

The dependence of the red-shift on the charge-transfer character is revealed in Figure 3.8(b), where the CT numbers of the absorption bands of the Wigner/COSMO and Wigner/MM ensembles as well as of the FC bright states are compared for the calculations in MeOH and in the gas phase. In general, CT states are energetically stabilized upon solvation in polar media due to more

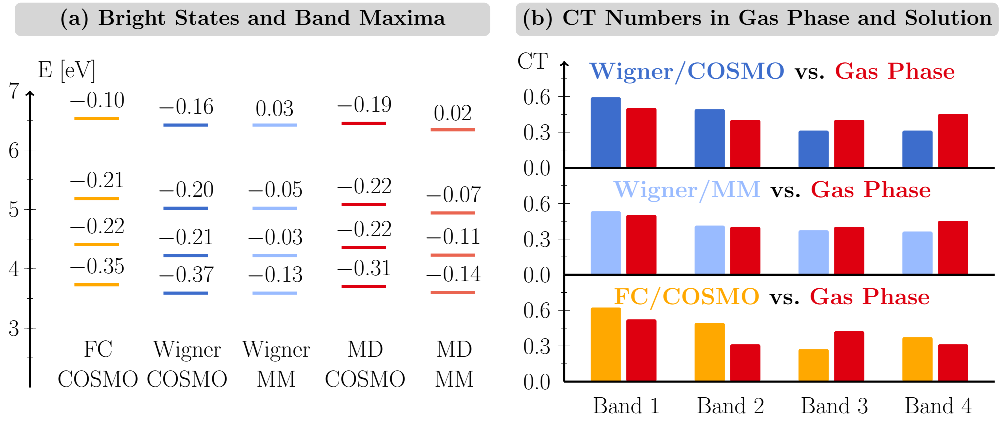

Figure 3.8: (a) Energy differences of the bright states and absorption maxima between excited-state calculations in gas phase and in MeOH. In the gas-phase calculations, still the solvent-equilibrated geometries from the original vibrational ensembles were used. (b) CT numbers of the absorption bands of the Wigner/COSMO and Wigner/MM ensembles and the FC bright states from excited-state calculations in gas phase and solution.

favorable electrostatic interactions, and the larger the CT character is, the larger the energetic stabilization can expected to be. Due to this, the lowest-energy bright state/absorption band of 2NN, that possess the most pronounced CT character, are shifted more towards lower energies in solution than the other bright states/absorption bands. In a rather conceptional picture, the shift upon solvation applies also to individual electronic configurations. Configurations with large CT character move to lower energies in polar media while the energy of configurations with small CT character stays constant. Thus, upon solvation in a polar medium, the CT character of the low-lying states increases even more at the expense of the CT character of the high-lying states. This feature becomes evident in Figure 3.8(b) by comparing the CT numbers of the bright states and absorption bands in gas phase and solution. As can be seen, the CT numbers of the low-energy bands/states 1 and 2 increase upon solvation, while the CT numbers of the high-energy bands/states 3 and 4 decrease.

The increase and decrease of CT numbers upon solvation of the low-energy and high-energy bands, respectively, is more pronounced when using the COSMO solvent model (ΔCT = 0.08) than for the MM solvent model (ΔCT = 0.02), thus resulting in the larger red-shift in the COSMO spectra compared to the MM spectra. As this energy shift is induced by electrostatic interactions between the solute and the solvent, the red-shift in the MM spectra is likely underestimated since electrostatic interactions are generally better described by continuum models than by using classical non-polarizable schemes. Thus, it is likely that the circumstance, that best agreement with the experimental absorption spectrum was obtained for the MD/MM ensemble, was solely due to fortuitous error cancellation.

Figure 3.8 also displayed the energy shifts and CT numbers for the FC bright states in gas phase and using COSMO. Compared to the Wigner/COSMO ensemble, the FC bright states show the same red-shifts as their corresponding absorption bands. In contrast, the change in CT character is larger for the FC bright states ($\Delta\text{CT} = 0.12$) than even for the Wigner/COSMO absorption bands ($\Delta\text{CT} = 0.09$). Thus, a simplistic anaylsis of the FC bright states overestimates the effect of the solvent on the character despite predicting the correct solvatochromic shift. This highlights again the importance of including nuclear motion to obtain a correct description of excited-state properties.

3.4 Including Temperature in Quantum Phase-Space Sampling

The study of the absorption spectrum of 2NN revealed two important effects of the vibrational motion for the description of the excited states: a red-shift of the absorption bands that was correlated to vibrational motion of the whole molecule, and a change of electronic character that depended more specifically on the torsional motion of the nitro group. The overall motion of the molecule – and, thus, the red-shift –should be better described for zero-temperature Wigner ensembles while the nitro group torsion –and, thus, the electronic character –should be better described in the thermal MD ensembles. This different performance is due to the uneven manner with which the different vibrational sampling approaches account for the energy of the molecule. As Wigner sampling accounts for the ZPE which, typically, comprises the largest fraction of the total vibrational energy, the motion of most of the vibrational modes is better described in Wigner sampling. However, for low-energy modes, the thermal-energy contributions can become larger than the ZPE. In these cases the thermal-energy contribution cannot be neglected in order to obtain meaningful results.

Motivated by this dilemma, the idea of a finite-temperature Wigner phase-space sampling was implemented in this work.

3.4.1 Finite-Temperature Wigner Phase-Space Sampling

In principle, the ZPE may be included in a crude way in thermal sampling by performing the MD simulations at an elevated temperature.[134] However, this leads to an inbalance in the description of low and high-frequency vibrational modes. As in MD simulations every degree of freedom receives in average the same energy, especially low-frequency modes would receive an excessive amount of energy, while the energy of high-frequency modes would still be too small. On the contrary, the thermal energy can be included in the usual (zero-temperature) Wigner sampling just by allowing the population of vibrationally excited states –a surprisingly simple idea. In fact, temperature is only a measure of the energy in the excited states in a quantum system – independently of whether they are electronically, vibrationally, or rotationally excited states. Despite this simplicity, this idea of finite-temperature Wigner distributions is only rarely mentioned[149–152] and only applied by one group, see, e.g., Refs. 149, 153–158. Also in the studies of this work, at first, only thermal (MD) sampling and zero-temperature Wigner sampling were employed, until the necessity to improve both samplings for an accurate description of 2NN lead to these considerations.

In practice, to perform finite-temperature Wigner phase-space sampling one needs to (i.) calculate the temperature-dependent probability to populate the n-th vibrational state φ_n, and (ii.) derive an expression for its Wigner distribution $W[\varphi_n]$. The probability $P_n(T)$ to populate the state φ_n at a temperature T can be obtained by a Boltzman distribution, i.e.,

$$P_n(T) = \frac{\exp\left(-\frac{E_n}{k_BT}\right)}{\sum_n \exp\left(-\frac{E_n}{k_BT}\right)} = \frac{\exp\left(-\frac{E_n}{k_BT}\right)}{Z(T)}. \tag{3.2}$$

For simplicity, the harmonic-oscillator model can be assumd with energy levels

$$E_n = \hbar\omega(n + 1/2) \quad \text{with} \quad n = 0, 1, 2, \ldots. \tag{3.3}$$

The canonical partition function $Z(T)$ then reads

$$Z(T) = \sum_{n=0}^{\infty} \exp\left(-\frac{\hbar\omega}{k_BT}(n + 1/2)\right) = \frac{\exp\left(-\frac{\hbar\omega}{2k_BT}\right)}{1 - \exp\left(-\frac{\hbar\omega}{k_BT}\right)}. \tag{3.4}$$

Using the temperature-dependent populations $P_n(T)$ from eq. (3.2), one can stochastically select vibrational states φ_n of the harmonic oscillator and calculate the corresponding Wigner distributions $W[\varphi_n]$. The wave functions of an harmonic oscillator with frequency ω_i and reduced mass μ_i read

$$\varphi_n(q_i) = \frac{1}{\sqrt{2^n n!}} \left(\frac{\mu_i\omega_i}{\pi\hbar}\right)^{1/4} \exp\left(-\frac{\mu_i\omega_i^2 q_i^2}{2\hbar}\right) H_n\left(\sqrt{\frac{\mu_i\omega_i}{\hbar}} q_i\right), \tag{3.5}$$

where $H_n(x)$ it the n-th order Hermite polynomial. Inserting this expression in the definition in eq. (3.1) yields the Wigner distribution

$$W_i[\varphi_n](q_i, p_i) = \frac{1}{\pi\hbar}(-1)^n \exp\left(-\frac{2H_i}{\hbar\omega_i}\right) L_n\left(\frac{4H_i}{\hbar\omega_i}\right) \tag{3.6}$$

for the state φ_n of the harmonic oscillator, where $L_n(x)$ is the n-th order Laguerre polynomial, and $H_i = p_i^2/2\mu_i + 1/2\mu_i\omega_i^2 q_i^2$ is the classical energy.

Thus, in finite-temperature Wigner phase-space sampling as introduced above one samples subsequently from the probability distribution of the harmonic-oscillator state populations and the selected states' corrsponding Wigner distribution. For a canonical ensemble of a one-dimensional harmonic oscillator, there exists also an approximated analytical expression for the Wigner distribution W, that reads[135,159]

$$W(q_i, p_i, T) = \frac{1}{\pi\hbar} \tanh\left(\frac{\hbar\omega_i}{2k_BT}\right) \exp\left(-\frac{2}{\hbar\omega_i} \tanh\left(\frac{\hbar\omega_i}{2k_BT}\right)\left(\frac{p_i^2}{2\mu_i} + \frac{\mu_i\omega_i^2 q_i^2}{2}\right)\right) \tag{3.7}$$

that was used in previous works.[149,153–158] This expression for $W(q_i, p_i, T)$ is positive for all values of (q_i, p_i) bearing the properties of "normal" probability distribution. In contrast, the Wigner function $W[\varphi_n](q_i, p_i)$ from eq. (3.6) can also adopt negative values, a reason for which it is often referred to as "quasi"-probability distribution. Certainly, dealing with the unusual "negative probabilities" can appear troublesome[152], motivating one to use $W(q_i, p_i, T)$ instead of $W[\varphi_n](q_i, p_i)$ to avoid this problem. However, for practical applications, when sampling a pair of coordinates (q_i, p_i) with negative quasi-probability $W[\varphi_n](q_i, p_i)$, one simply has to discard these coordinates, in line with the interpretation that they correspond to phase-space regions that the molecule simply cannot access in experiment[160,161] –a feature that can also be demonstrated in experiment.[162] The use of $W[\varphi_n](q_i, p_i)$ also possesses one conceptional advantage over the use of $W(q_i, p_i, T)$, as $W(q_i, p_i, T)$ does not contain any information about the vibrational state that the molecule occupies. Although, a quantum system can be in a superposition of reference states, this superposition should collapse to a single state once a corresponding property of the system is measured, i.e., once the system is sampled. Thus, using a Boltzman distribution of Wigner functions $W[\varphi_n](q_i, p_i)$ appears to be the more natural approach.

3.4.2 Zero-Point Energy and Thermal-Energy Contributions

Finite-temperature Wigner phase-space sampling is performed by allowing the molecule to populate both, vibrational ground and excited states. The population of the vibrationally excited states depends on the frequency of the vibrational modes and the temperature. Thus, for every vibrational mode, a different part of the population is in its excited states, which adds a different amount of thermal energy to the total energy. The total energy of the molecule is simply the sum of total energies of the individual vibrational modes, that, in the harmonic oscillator approximation are given as the sum of the ZPE and a thermal energy contribution: $\varepsilon(T)$

$$E(T) = \sum_{n=0}^{\infty} P_n(T) E_n = \frac{\hbar\omega}{2} + \hbar\omega \frac{\exp\left(-\frac{\hbar\omega}{k_BT}\right)}{1 - \exp\left(-\frac{\hbar\omega}{k_BT}\right)} = \mathrm{ZPE} + \varepsilon(T), \tag{3.8}$$

Note that only in the high-temperature limit $k_BT \gg \hbar\omega$, when the thermal-energy contribution becomes $\varepsilon(T) = k_BT - \hbar\omega$, the total energy approximately amounts to

$$\lim_{k_BT \gg \hbar\omega} E(T) \approx k_BT \tag{3.9}$$

which is frequently used as the thermal energy irrespective of the ratio T/ω.

It is interesting to examine the temperature-dependent populations of vibra-

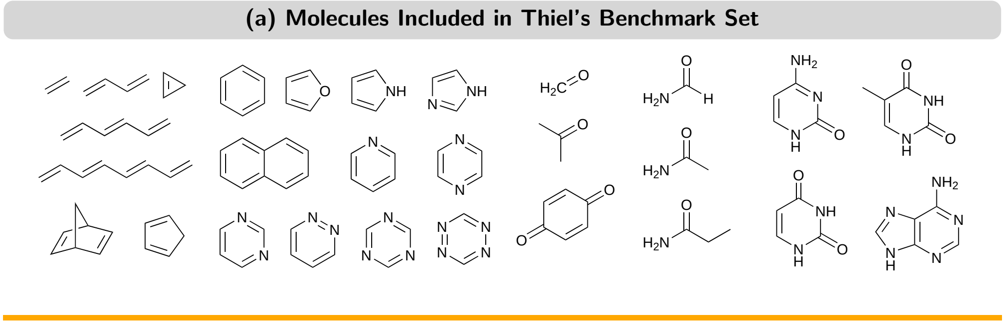

(a) Molecules Included in Thiel's Benchmark Set

Figure 3.9: Molecules included in Thiel's benchmark set.[163]

tional modes and the contributions of their ZPE and $\varepsilon(T)$ in typical molecules encountered in computational studies, such as the molecules in the Thiel benchmark set shown in Figure 3.9.[163] For these molecules, the ZPE and thermal-energy contributions to the total energy at a temperature of $T = 300$ K are listed in Table 3.1. For one simple representative, formamide, also the populations of the vibrational ground (P_0) and excited states (P_n) as well as the contributions of ZPE and thermal energy $\varepsilon(T)$ to the total energy $E(T)$ at a temperature of $T = 300$ K are shown for each mode in Table 3.2.

As can be seen in Table 3.2, at a temperature of $T = 300$ K, most of the vibrational modes of formamide are nearly completely in their ground state ($P_0 \approx 100$ %). Thus, their small excited-state populations only contribute small amounts of thermal energy $\varepsilon(T)$ to the total energy. Only the three lowest-frequency modes show notable population of the vibrational excited states, that for the lowest-frequency mode ω_1, however, is already larger in sum than the ground-state population P_0. Thus, only these modes possess considerable thermal-energy contributions to the total energy. All thermal-energy contributions $\varepsilon_i(T)$ sum up to 237 cm^{-1}, corresponding to 2.3 % of the total energy of 10408 cm^{-1} at $T = 300$ K. For the molecules in Thiel's benchmark set (Table 3.1), this contribution of the thermal energy ranges between 0.1 % (formaldehyde) and 4.3 % (thymine). Comparing all thermal-energy contributions shows that $\varepsilon(T)$ is unique for each molecule. This is due to the distribution of normal-mode frequencies in the individual molecules: the more low-frequency modes the molecule possesses, the larger the thermal energy contribution is. Typically, high-frequency normal modes are associated with very rigid internal movements in the molecule, e.g., vibrations between atoms with strong chemical bonds. In contrast, low-frequency normal modes describe more flexible motion, e.g., vibrations between loosely bound atoms or torsional motions of atom groups. Based on this, one can predict, that the less rigid the chemical structure of a molecule is, the larger the thermal energy will contribute to the total energy of the molecule. For the molecules in Thiel's benchmark set, this prediction works well. Molecules with non-rigid structural elements such as CH_3 or NH_2 groups show the largest thermal-energy contributions (3-4 %), while small and extremely rigid molecules such as ethene or formaldehyde possess nearly none ($\varepsilon < 0.4$ %).

ZPE and Thermal Energy Contributions

Molecule	ZPE	$\varepsilon(T)$	$E(T)$	$C(ZPE)$	$C(\varepsilon)$
Acetamide	2.054	0.063	2.117	97.01	2.98
Acetone	2.342	0.070	2.413	97.08	2.91
Adenine	3.089	0.121	3.210	96.23	3.76
Benzene	2.754	0.048	2.802	98.26	1.73
Benzoquinone	2.315	0.100	2.416	95.82	4.17
Butadiene	2.362	0.051	2.413	97.87	2.12
Cyclopentadiene	2.565	0.037	2.602	98.56	1.43
Cyclopropene	1.566	0.013	1.579	99.14	0.85
Cytosine	2.725	0.104	2.829	96.32	3.67
Ethene	1.424	0.005	1.430	99.60	0.39
Formaldehyde	0.745	0.001	0.746	99.87	0.12
Formamide	1.261	0.029	1.290	97.71	2.28
Furan	1.928	0.026	1.954	98.66	1.33
Hexatriene	3.284	0.110	3.394	96.75	3.24
Imidazole	1.966	0.026	1.992	98.67	1.32
Norbornadiene	3.571	0.054	3.625	98.49	1.50
Octatetraene	4.204	0.170	4.375	96.09	3.90
Propanamide	2.863	0.093	2.957	96.84	3.15
Pyrazine	2.120	0.038	2.158	98.23	1.76
Pyridazine	2.093	0.040	2.134	98.08	1.91
Pyridine	2.445	0.041	2.487	98.31	1.68
Pyrimidine	2.126	0.038	2.164	98.23	1.76
Pyrrole	2.277	0.033	2.310	98.53	1.46
Tetrazine	1.412	0.038	1.450	97.35	2.64
Thymine	3.180	0.141	3.321	95.73	4.26
Triazine	1.804	0.035	1.839	98.08	1.91
Uracil	2.398	0.095	2.494	96.17	3.82

Table 3.1: ZPE, thermal energy $\varepsilon(T)$, and total energy $E(T)$ in eV as well as percentage of contributions $C(\text{ZPE})$ and $C(\varepsilon)$ of the ZPE and thermal energy, respectively, for the molecules contained in the Thiel benchmark set.[163] Geometry optimizations and frequency calculations performed at MP2/6-31G* level of theory using Gaussian09.

Populations and Energy Contributions of Vibrational States of Formamide

Mode	ω_i	P_0	$\sum_{n>0} P_n$	ZPE$_i$	$\varepsilon_i(T)$	$E_i(T)$
ω_1	132.08	46.6	53.4	66.04	149.38	215.42
ω_2	564.96	93.3	6.7	282.48	40.28	322.76
ω_3	649.30	95.5	4.5	324.65	30.17	354.82
ω_4	1058.31	99.3	0.7	529.15	6.65	535.80
ω_5	1074.72	99.4	0.6	537.36	6.24	543.60
ω_6	1305.22	100.0	0.0	652.61	2.49	655.10
ω_7	1458.89	100.0	0.0	729.44	1.33	730.78
ω_8	1657.87	100.0	0.0	828.93	0.58	829.51
ω_9	1841.38	100.0	0.0	920.69	0.26	920.95
ω_{10}	3066.37	100.0	0.0	1533.18	0.00	1533.18
ω_{11}	3689.79	100.0	0.0	1844.89	0.00	1844.89
ω_{12}	3843.70	100.0	0.0	1921.85	0.00	1921.85

Table 3.2: Population of vibrational ground (P_0) and excited states (P_n) in percentage (%) as well as contributions of ZPE and thermal energy $\varepsilon(T)$ to the total energy $E(T)$ in cm^{-1} of the normal modes of formamide at $T = 300$ K. Geometry optimizations and frequency calculations performed at MP2/6-31G* level of theory using Gaussian09.[164]

Including finite-temperature effects, when generating initial conditions using Wigner sampling, can impact excited-state dynamics simulations. The additional vibrational energy given by the thermal-energy contribution in the electronic ground state will also be available in the electronically excited state. This can facilitate climbing potential-energy barriers in the excited state as is depicted in Figure 3.10(a). For the molecules in the Thiel benchmark set, this additional energy is of the order of 0.1-0.2 eV at $T = 300$ K (see Table 3.1), which could be decisive for the outcome of an excited-state reaction. This influence becomes even larger for larger molecules, where, due to the larger number of low-frequency vibrational modes, the thermal-energy contribution naturally becomes larger, e.g., amounting to 0.7 eV for a Ru(bpy)$_3$ metal complex.

Besides the additional energy available when generating initial conditions at a finite temperature, the shape of the Wigner distribution changes due to the contribution of vibrationally excited states. The higher excited these states are, the more their probability distribution is shifted away from the minimum of the harmonic potential. Thus, Wigner sampling at a finite temperature can yield a considerable fraction of nuclear conformations that are farther displaced from the potential-energy minimum and are less accessible at zero temperature. Exciting the molecule in these displaced conformations can open new reaction pathways in the excited state, by placing the molecule closer to or on the other side of potential-energy barriers as shown in Figure 3.10(b). While the consideration presented here are rather theoretical, a practical example of the temperature effects on the excited-state dynamics of 2-nitronaphthalene is

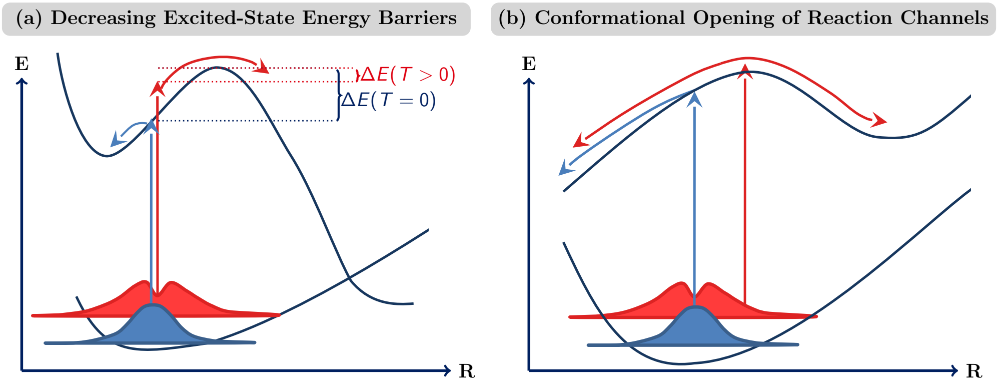
(a) Decreasing Excited-State Energy Barriers
E
R
ΔE(T > 0)
ΔE(T = 0)
(b) Conformational Opening of Reaction Channels
E
R

Figure 3.10: (a) Decrease of a energy barrier in the electronically excited state due to increased vibrational energy in the electronic ground state. (b) Opening of a new reaction channel due to more wide spread conformational phase space sampling.

presented lateron in Chapter 5.

3.5 Conclusions on Vibrational Sampling

Vibrational sampling is an important and well-known tool to generate an ensemble of geometries with different internal coordinates and momenta for use, e.g., as initial conditions in excited-state dynamics simulations. It can be employed also to introduce the effects of vibrational motion on excited states in static quantum-chemical calculations. For the absorption spectra of nitrobenzene in the gas phase and in water, it was shown that neglecting vibrational motion and calculating the excited states of this molecule solely at the FC geometry yields an erroneous characterization of its lowest-energy absorption band. The pronounced CT character that was found for the bright state at the FC geometry was quenched to a large extent in the excited states of a vibrational ensemble at the corresponding absorption band maximum, i.e., in the multitude of different states that are excited to in experiment. In addition to the difference of the average electronic properties of the vibrational ensemble and the FC geometry, both differ also in their structural features. While the minimum-energy FC geometry is planar, the structures in the ensemble are in average non-planar due to the torsion of the nitro group.

In pratice, vibrational sampling can be accomplished by quantum phase-space sampling, e.g., from a Wigner distribution, or by classical phase-space sampling, e.g., from a MD trajectory. The performance of two approaches, zero-temperature Wigner sampling and thermal MD sampling at $T = 300$ K, was investigated upon calculating the absorption spectrum of 2NN in MeOH. As in the case of nitrobenzene, also for 2NN it was found that including vibrational motion leads to state mixing, which changes the characters of some of the absorption bands compared to the bright states at the FC geometry. In addition, the vibrational sampling induced a red-shift for all absorption bands of the spectrum. This red-shift scaled with the extent of motion accounted for by the sampling method, i.e., it was larger for the Wigner sampling than for the MD sampling. The larger motion in the Wigner sampling is because the ZPE included in the Wigner sampling is larger than the thermal energy included in the MD sampling.

At a finite temperature, the total energy of a molecule is the sum of its ZPE and a thermal-energy contribution, and neither zero-temperature Wigner sampling nor thermal MD sampling account for this total energy. The total energy can, however, be accounted for in Wigner sampling by including the effects of finite temperatures, i.e., the population of vibrationally excited states. This can be realized easily either through using the Wigner distribution of a canonical ensemble or by sampling the different Wigner distributions of all vibrational states according to their temperature-dependent populations. Due to this simplicity, whenever computationally affordable, finite-temperature Wigner phase-space sampling should become the new standard for vibrational sampling.

Finally, an interesting thought on vibrational sampling from MD simulations is the following. The thermal energy k_BT included in MD sampling corresponds only in the high-temperature limit to the real thermal energy contribution $\varepsilon(T)$ of the total energy. For most temperatures, it is $k_BT \gg \varepsilon(T)$ while at the same time, for moderate temperatures –say, 300 K –it is often $k_BT \ll$ ZPE. Thus, at such moderate temperatures, the energy that a molecule possesses in MD simulations does not agree with the energy available to the same molecule under experimental conditions, i.e., the molecule possesses the "incorrect" energy in MD simulations. This problem can become apparent when performing ab initio MD simulations where the molecule moves in the "correct" quantum-chemical potential possessing the wrong energy. This holds for MD simulations in both, electronic ground and excited states. However, this situation may be different in MD simulations on potentials computed by empirical force fields. These potentials usually differ from the correct quantum-chemical potentials, i.e., they are incorrect. In this case, the combination of wrong energies and incorrect potentials can give better results thanks to improved error cancellation than an ab initio MD simulation. Classical MD simulations purposely rely on this error cancellation through the parametrization of the empirical force fields. In contrast, ab initio MD simulations are destined to feature some error in their results through combinig the wrong energies for the correct potentials. Clearly, this is an interesting topic that should be explored further.

4 The CASPT2 Method and Excited States of Organic Molecules

In Chapter 2, a number of methods have been introduced that are used to solve the electronic part of the Schrödinger equation, i.e., to calculate electronic states and their energies. These methods –HF, FCI, CASSCF, CASPT2, DFT, and TDDFT –are the ones most used in this work. However, they represent only a small fraction of the variety of methods that is available in the toolbox of modern computational chemistry. As ab initio methods, these methods should be generally applicable to study all kinds of processes in all different kinds of molecules. In practice, though, the choice of the method is dictated by the nature of process and the size of the molecule that is studied –and it is the responsibility of the theoretical chemist to select the appropriate, which usually requires extensive testing and benchmarking. Sadly, in the majority of studies published in the scientific literature, only the application of the finally identified, suitable method is reported. This conceals the bad performance of the other tested methods, leaving these methods with a clean track record of only successful applications that are published. Thus, the real performance and applicability of most methods is not as well known as suggested by the available literature.

One of the most trusted methods for the description of electronic states is CASPT2, having been named the "gold standard for strong correlation problems".[165] It is commonly believed to be able to describe electronic states with an error smaller than 0.2 eV. Therefore, initially in this work, CASPT2 was seen as a promising candidate to use in the investigation of the exicted states of nitrobenzene and other small aromatic nitro compounds, and its performance was tested extensively. This chapter summarizes the experiences made with CASPT2 in the study of the electronically excited states of nitrobenzene, 2-nitronaphthalene, and other organic compounds. Parts of the results presented in this chapter have been published in the studies "Quenching of Charge Transfer in Nitrobenzene Induced by Vibrational Motion" in the Journal of Physical Chemistry Letters[131] and in "The IPEA Dilemma in CASPT2" in Chemical Science[166].

4.1 The Study of Nitrobenzene and 2-Nitronaphthalene

The work of this thesis began with the study of the excited states of nitrobenzene at the state-averaged (SA) CASSCF[76]/multi-state (MS) CASPT2[77,78,129] level of theory. The excited states of nitrobenzene were computed at the FC geometries in gas phase and aqueous solution using PCM[96] to describe the solvent. The calculations used different active spaces, included different numbers

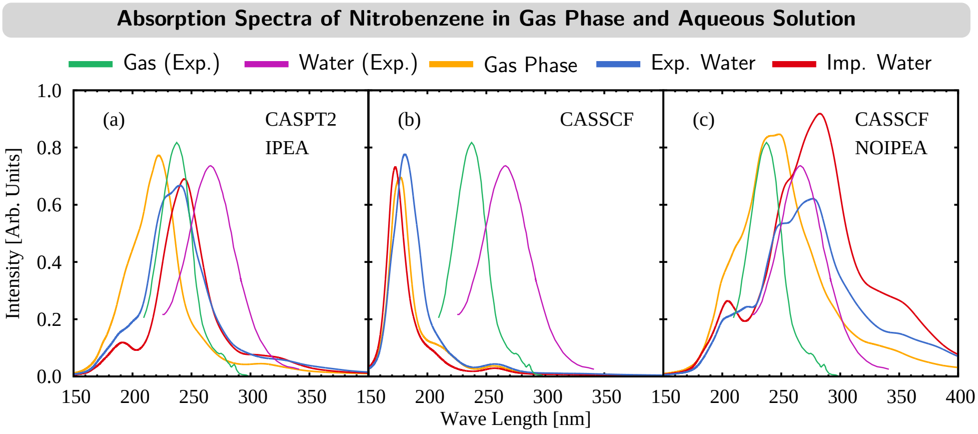

Figure 4.1: Experimental[115] and calculated absorption spectra of nitrobenzene in gas phase and aqueous solution. Calculations performed at the SA(7)-CASSCF/ANO-L-VDZP (b) and MS(7)-CASPT2/ANO-L-VDZP (a,c) levels of theory using a (14,11) active space and IPEA shift values of 0.25 a.u. (IPEA) and 0 (NOIPEA) for the vibrational ensembles from Section 3.1.2.

of states in the state-averaging, used different sizes of ANO-RCC basis sets[167], and employed the IPEA-shifted Hamiltonian with the recommended IPEA shift value of $\varepsilon = 0.25$ a.u.[168] Despite computationally demanding, these efforts sadly yielded very poor results. For example, using the ANO-RCC-VDZP basis set and a (14,11) active space including all π and π^* orbitals as well as two n orbitals at the nitro group, excitation energies of 5.76 and 5.39 eV were obtained for the bright states at the FC geometries in gas phase and aqueous solution of nitrobenzene. These energies are far off from the maxima of the experimental[115] absorption bands at 5.16 and 4.66 eV, respectively, i.e., the CASPT2 results show surprisingly large deviations of 0.6-0.7 eV from experiment.

One attempt to improve the poor performance of CASPT2 was to augment the ANO-RCC basis set with diffuse functions at the atoms of the nitro group to better describe the CT character of the bright excited states at the FC geometry (recall Section 3.1.2). In the course of this, however, an error in the ANO-RCC basis set was discovered.[169] Thus, unassured, whether the ANO-RCC results could be trusted, all CASPT2 calculations were repeated using ANO-L basis sets.[130] These calculations, however, yielded very similar errors compared to experiment as those obtained using the erroneous ANO-RCC basis sets.

Despite the large errors comparing the energies of the bright states to the positions of the experimental band maxima, the solvatochromic red-shift of ca. 0.5 eV, that was found for the experimental absorption bands when going from gas phase to aqueous solution, was reproduced correctly by the CASPT2 calculations at the FC geometries. With this spark of hope, the full absorption spectra of nitrobenzene in gas phase and aqueous solution were computed using vibrational sampling based on the sequential MM/QM approach introduced in Section 3.1.1. The resulting spectra are shown in Figure 4.1(a). The calculated absorption bands possess maxima at ca. 5.6 and 5.1 eV in gas phase and aqueous solution, respectively. These maxima are slightly red-shifted from the bright states at the FC geometries, however, being still 0.5 eV higher in energy than the experimental absorption maxima. For comparison, Figure 4.1(b) also shows the absorption spectra calculated at the CASSCF level of the theory. There, the absorption-band maxima appear around 7.0 eV in both, gas phase and solution, even further away from the experimental results. Thus, despite the large deviation from experiment, CASPT2 still yields a considerable improvement over the CASSCF results.

As a last resort, the CASPT2 calculations were repeated setting the IPEA shift parameter to 0. The IPEA shift is an empirical parameter[168] that was introduced to correct for a systematic underestimation of dissociation energies of small molecules. This underestimation was believed to originate from a general underestimation of the energies of electronic states with open-shell character, and, thus be present also in the calculation excitation energies. Despite its nature, the IPEA shift parameter ε "should not be used as an empirical parameter to improve the results of a specific application".[75] Rather, if large errors should appear in CASPT2 calculations, they were believed to have other sources. Yet, lo and behold, setting the IPEA shift parameter ε to zero resulted in a strong red-shift of the calculated absorption bands of nitrobenzene, and, as can be seen in Figure 4.1(c), finally, gave a good agreement with the experimental spectra in gas phase and solution. The results obtained in these calculations have already been presented in Section 3.1.

Following the study of nitrobenzene, the excited states of 2-nitronaphthalene were investigated at the CASPT2 level of theory. Based on the experience gained for nitrobenzene, the calculations were performed by again setting the IPEA shift parameter ε to zero ("NOIPEA"). At the FC geometry, the best agreement with an experimental reference spectrum[13] was found for a (14,11) active space, for which the results are shown in Figure 4.2(a). As can be seen, the energies of the first two bright states calculated with $\varepsilon = 0$ agree well with positions of the absorption band maxima, being red-shifted only slightly by 0.25 and 0.03 eV, respectively. Accordingly, the full absorption spectrum was calculated using the same active space and IPEA shift of zero for a vibrational ensemble of 100 geometries obtained from a classical MD trajectory of 2NN in MeCN. Shown in Figure 4.2(b), this calculated spectrum displays two absorption bands similar to the experimental one. While the higher-energy band 2 agrees well with its experimental reference, the lower-energy band 1 is found at too low energies, being red-shifted by ca. 0.5 eV from the experimental absorption band 1, i.e., even further away than its corresponding bright state S_1 at the FC geometry (0.25 eV).

The error of 0.5 eV of the lower-energy absorption band is surprisingly large for a CASPT2 excitation energy, especially given the good agreement of the higher-energy absorption band and the smaller error of the bright S_1 state at the FC geometry. Therefore, in analogy to the study of nitrobenzene, the CASPT2 calculations were repeated using a different IPEA shift value. However, contrary to the study of nitrobenzene, the IPEA shift was re-set from zero to the recommended value of $\varepsilon = 0.25$ a.u. The results of these CASPT2

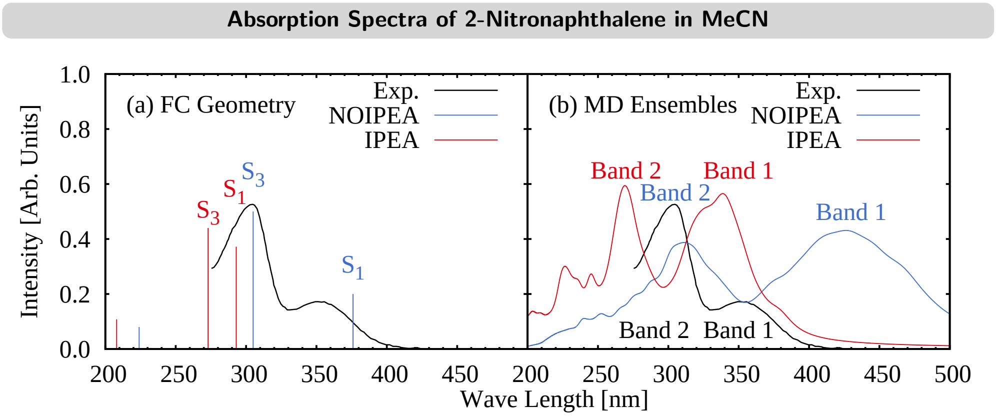

Figure 4.2: Experimental[13] and calculated absorption spectra of 2-nitronaphthalene in MeCN. Calculations performed at the MS(7)-CASPT2/ANO-L-VDZP level of theory using a (14,11) active space and IPEA shift values of 0.25 a.u. (IPEA) and 0 (NOIPEA) at the FC geometry (a) and for a vibrational ensemble of 100 geometries obtained from a MD trajectory (b). Solvent MeCN modeled using PCM.

calculations (“IPEA”) at the FC geometry and for the vibrational ensemble are shown in Figure 4.2(a) and (b), respectively. The IPEA bright states at the FC geometry are strongly blue-shifted from the experimental absorption bands by 0.5-0-7 eV. The same size of error is also found for the calculated absorption band 2 for the vibrational ensemble. In contrast, however, the calculated absorption band 1 is now only 0.1 eV blue-shifted from its experimental reference. Clearly, some sort of error cancellation is at play, which involves the IPEA shift and potentially the sampling scheme, and which affects the two absorption bands differently. Given the large impact that was found for the IPEA shift on the excitation energies of 2NN as well as nitrobenzene, it seemed that using the appropriate IPEA shift value is crucial to obtain meaningful results. Thus, in order to evaluate the impact of the IPEA shift value systematically, a closer look was taken on the origin of the IPEA shift and its performance in excited-state calculations.

4.2 The IPEA Dilemma in CASPT2

4.2.1 Introduction of the IPEA Shift

Soon after the first implementations of CASPT2 in 1990-1992[77,78], a report on systematic errors calculations of equilibrium geometries and atomization energies of a set of 32 small molecules was published.[170] While the calculated CASPT2 equilibrium geometries agreed well with their experimental references, the atomization energies were underestimated. This underestimation scaled by 3-6 kcal/mol (0.13-0.26 eV) times the differences of the number of electron pairs in the molecules and their atomic fragments. This error was later ascribed to an energetic favoring of wave functions dominated by an open-shell configuration over those dominated by closed-shell configurations.[171] Different corrections to the zeroth-order Hamiltonian of CASPT2 were suggested[171], however, providing only minor improvements.

In 2004, an explanation of the underestimation of the energy of open-shell electronic states was suggested[168] upon inspection of the diagonal elements of the matrix representation f_{pq} of the generalized Fock operator $\hat{\mathcal{F}}$ (see Section 2.3.2). It was assumed that Koopmans' theorem –stating that for single-configurational wave functions the orbital energies of occupied and unoccupied orbitals give good approximations to the negative ionization potentials $-(\mathrm{IP})_p$ and electron affinities $-(\mathrm{EA})_p$, respectively –also should hold for the multi-configurational CASPT2 wave functions. In the single-configurational case, the orbital energies are simply given by the diagonal elements of the standard Fock operator [see eq. (2.12)]. However, the non-diagonal form of the generalized Fock operator requires the neglect of the inactive-active and active-secondary coupling matrix elements to apply the Koopmans approximation. Still doing so, it was assumed[168] that the diagonal elements f_{pp} of the generalized Fock operator for active orbitals may be written as weighted averages of $-(\mathrm{IP})_p$ and $-(\mathrm{EA})_p$, so that

$$f_{pp}^{\mathrm{active}}(N_{pp}) = -\frac{1}{2}\left(N_{pp}(\mathrm{IP})_p + (2 - N_{pp}) \cdot (\mathrm{EA})_p\right). \tag{4.1}$$

For doubly occupied ($N_{pp} = 2$) and empty ($N_{pp} = 0$) active orbitals, f_{pp}^{active} reduces simply to $-(\mathrm{IP})_p$ and $-(\mathrm{EA})_p$, respectively. For singly-occupied ($N_{pp} = 1$) active orbitals, the matrix elements f_{pp}^{active} reads

$$f_{pp}^{\mathrm{active}}(N_{pp} = 1) = -\frac{1}{2}\left((\mathrm{IP})_p + (\mathrm{EA})_p\right). \tag{4.2}$$

It was asserted that "this feature of the [generalized] Fock operator will lead to denominators in the expression for the second-order energy that are too small in the case of excitation into or out from a partially occupied orbital"[168], which, in turn, lead to the underestimation of the energies of open-shell electronic states.

As an attempt to correct the diagonal matrix elements, it was suggested to add different shift values $\sigma_p^{(\mathrm{EA})}$ and $\sigma_p^{(\mathrm{IP})}$ to f_{pp}^{active} when exciting into or out of an active orbital, respectively. For the singly-occupied active orbitals, the shifted matrix elements should be

$$\begin{aligned}
\widetilde{f}_{pp}^{\mathrm{active}}(N_{pp} = 1)^{\mathrm{EA}} &= f_{pp}^{\mathrm{active}} + \sigma_p^{(\mathrm{EA})} = f_{pp}^{\mathrm{active}} + \frac{1}{2}N_{pp}\left((\mathrm{IP})_p - (\mathrm{EA})_p\right) \\
&= -(\mathrm{EA})_p && (4.3) \\
\widetilde{f}_{pp}^{\mathrm{active}}(N_{pp} = 1)^{\mathrm{IP}} &= f_{pp}^{\mathrm{active}} + \sigma_p^{(\mathrm{EA})} = f_{pp}^{\mathrm{active}} + \frac{1}{2}(2 - N_{pp})\left((\mathrm{IP})_p - (\mathrm{EA})_p\right) \\
&= -(\mathrm{IP})_p && (4.4)
\end{aligned}$$

Both shifts $\sigma_p^{(\mathrm{EA})}$ and $\sigma_p^{(\mathrm{IP})}$ depend on the difference $(\mathrm{IP})_p - (\mathrm{EA})_p$. As it was not clear how to determine the individual values of $(\mathrm{IP})_p$ and $(\mathrm{EA})_p$, the differences for the shifts of all active orbitals were replaced by a single average shift parameter $\varepsilon = (\mathrm{IP})_p - (\mathrm{EA})_p$, the IPEA shift parameter. For $\varepsilon > 0$, the shift will increase the total energies of open-shell states by decreasing their second-order energy contribution $E^{(2)}$. This becomes apparent when one splits up the sum of Eq. (2.26) into terms belonging to closed-shell configurations (index i) and terms belonging to open-shell configurations (index j),

$$\begin{aligned} E^{(2)} = & - \sum_{i=1}^{\text{closed-shell}} \frac{\left| \left\langle \Phi_i \middle| \hat{\mathcal{H}}' \middle| \Psi^{(0)} \right\rangle \right|^2}{E_i - E^{(0)}} \\ & - \sum_{j=1}^{\text{open-shell}} \frac{\left| \left\langle \Phi_j \middle| \hat{\mathcal{H}}' \middle| \Psi^{(0)} \right\rangle \right|^2}{E_j - E^{(0)} + \frac{1}{2}\kappa_j \varepsilon}. \end{aligned} \tag{4.5}$$

For the elements of the first partial sum, $N_{pp} = 0$ for $\sigma_p^{(\mathrm{EA})}$ and $N_{pp} = 2$ for $\sigma_p^{(\mathrm{IP})}$, so that no shift ε is added. But for the elements in the second sum, a shift is added. The prefactor κ_j can take the values 0, 1, and 2, depending on the excitation class of Φ_j.[172]

An optimal value for the effective IPEA shift parameter was determined empirically by calculating the dissociation energies of 49 diatomic molecules and comparing the results with experimental reference data.[168] Without the IPEA shift, the dissociation energies were mostly underestimated with the largest errors found for triply-bonded diatomics N_2, P_2, and As_2, and the average unsigned error $\Delta E = |E_{\mathrm{calc}} - E_{\mathrm{exp}}|$ of the complete set amounted to 0.22 eV. In contrast, using a IPEA shift value of $\varepsilon = 0.25$ a.u. lead to a minimal unsigned error of 0.09 eV.

In addition to the calculation of the dissociation energies, the influence of the IPEA shift was further tested for a few additional properties of selected molecules. For equilibrium geometries and harmonic vibrational frequencies in the ground and excited states of a small number of diatomic molecules an optimal parameter of $\varepsilon = 0.1$ a.u. was found, while for anharmonic-frequency corrections the optimal parameter was $\varepsilon \geq 0.5$ a.u. Furthermore, four adiabatic excitation energies of N_2 and four vertical excitation energies for benzene were computed, again suggesting different optimal shift values of 0.4 and 0.1 a.u., respectively. Finally, the ionization potentials of the $3d$ transition metals were computed using only a shift of $\varepsilon = 0.25$ a.u. and good agreement with the experimental results was observed. From all of these results, it was concluded that a shift of $\varepsilon = 0.25$ a.u. represented the optimal value for CASPT2 calculations to correct the systematic error in the description of open-shell states. This value, coincidentally, resembles the average atomic value of the quantity (IP − EA) when going through the periodic table, which was seen as a good omen to give some physical motivation to the size of the IPEA shift.[75]

4.2.2 Literature Survey of CASPT2 Excitation Energies

The underestimation of open-shell state energies was believed to be present also in the calculation of excitation energies. However, there existed no sys-

(a) Organic Molecules Included in the Literature Survey

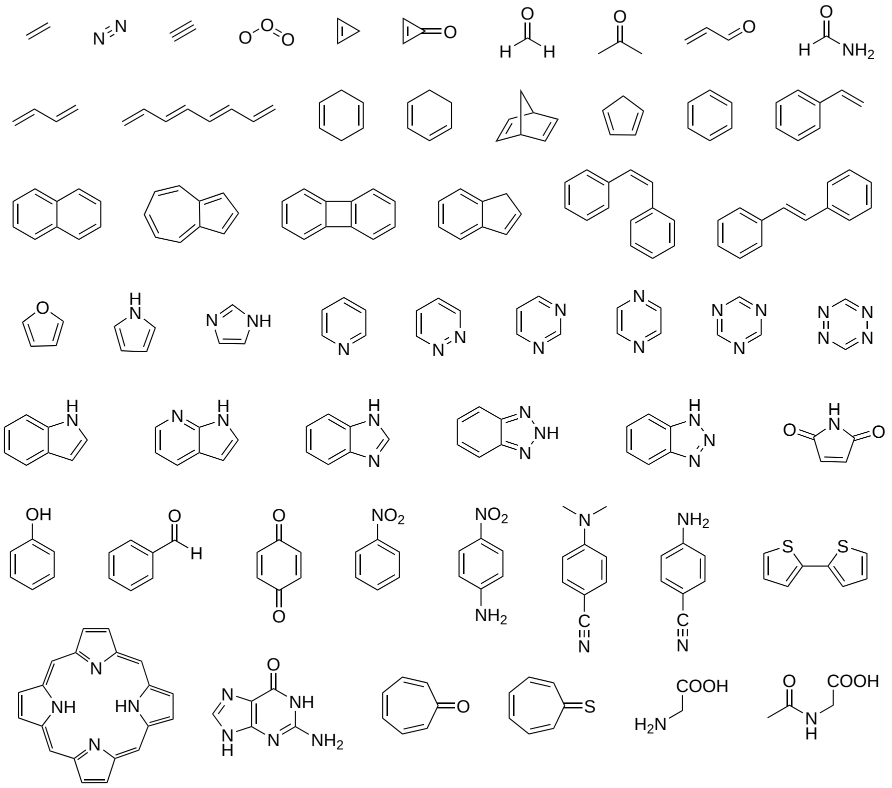

(b) Metal Complexes Included in the Literature Survey

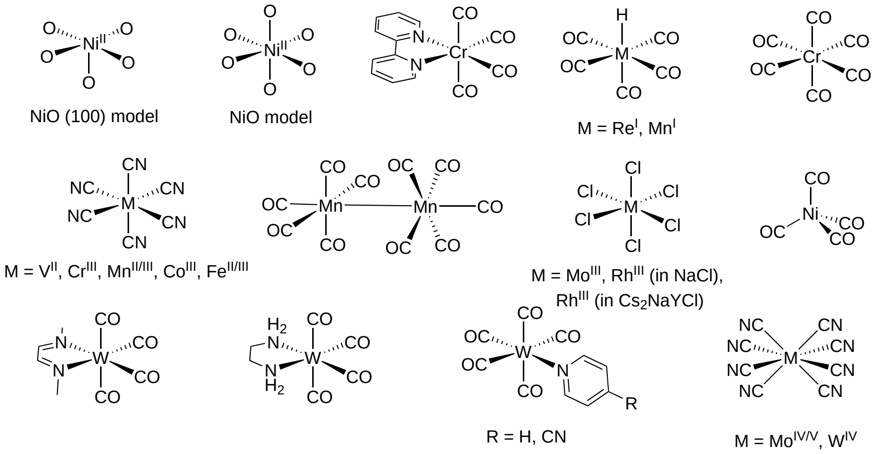
NiO (100) model
NiO model
M = Re^I, Mn^I
M = V^{II}, Cr^{III}, Mn$^{II/III}$, Co^{III}, Fe$^{II/III}$
M = Mo^{III}, Rh^{III} (in NaCl), Rh^{III} (in Cs$_2$NaYCl)
R = H, CN
M = Mo$^{IV/V}$, W^{IV}

(c) Molecules Included in the FCI-CASPT2 Benchmark Study

HLi HBe HB HC HN HO Li_2 B_2 C_2 N_2 H_2O CH_2

Figure 4.3: (a/b) Organic molecules and metal complexes included in the literature survey. (c) Molecules included in the FCI-CASPT2 benchmark study.

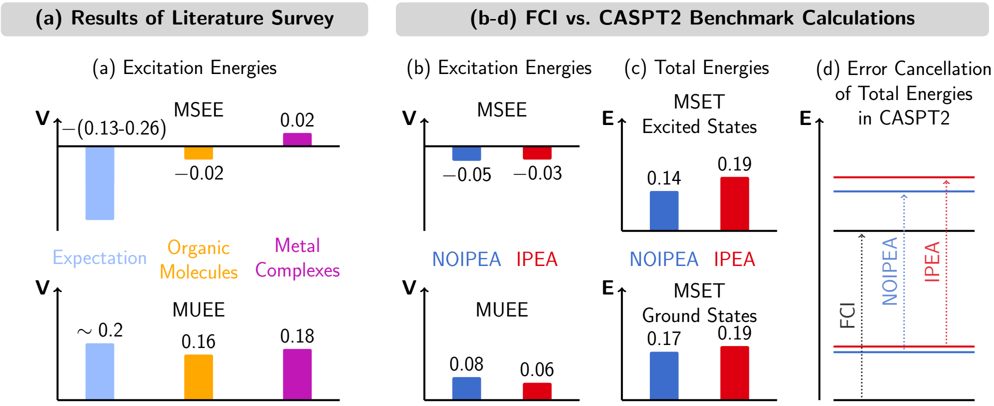

Figure 4.4: (a) Mean signed and unsigned errors of CASPT2 excitation energies V in eV (MSEE/MUEE) of molecules included in the literature survey with respect to experimental reference data. (b/c) Mean signed and unsigned errors of excitation energies V in eV (MSEE/MUEE) as well as mean signed error of total energies E in eV (MSET) of ground and excited states of the molecules included in the FCI-CASPT2 benchmark. Errors with respect to FCI results. (d) The improved error cancellation in the IPEA-CASPT2 calculations is due to an increase of the errors of the energies of the excited states. (b-d) Only results for the 6-31G basis set are shown as using the 6-311G basis set yielded very similar results.

tematic study demonstrating this effect. Thus, in this work, a literature survey was performed collecting vertical excitation energies computed with CASPT2 up to 2004 –the year that the IPEA shift was introduced. The energies of 356 excited states of 53 organic molecules[121,129,171,173–209] and 92 excited states of 25 metal complexes[182,210–222] were collected and compared to experimental reference data. The organic molecules and metal complexes are shown in Figure 4.3(a) and (b), respectively. The result of the literature survey is shown in Figure 4.4(a).

The ground states of the molecules included in the literature survey are closed-shell states and most of their low-lying excited states are described by single excitations. Accordingly, the number of paired electrons in the ground and excited states typically differs by two electrons (one electron pair), and their excitation energies are expected to be underestimated by ca. 0.13-0.26 eV (3-6 kcal/mol). This expectation is not met, however, neither for the organic molecules nor for the metal complexes. The mean signed error of the excitation energies (MSEE) of the organic molecules is only -0.02 eV, i.e., an order of magnitude smaller than expected, while the excitation energies of the metal complexes are even slightly overestimated by 0.02 eV. In addition to an MSEE close to zero, also the mean unsigned error for the excitation energies (MUEE) of CASPT2 is small: MUEE < 0.2 eV, which is commonly considered to be the error of CASPT2 in predicting excitation energies. Given the overall good performance (small MUEE) and the absence of a sizable systematic error (small

MSEE), it seems questionable whether the systematic error present in the calculation of dissociation energies of the diatomic molecules is also present when calculating excitation energies, and whether, accordingly, the IPEA shift should be used in the calculation of excitation energies.

4.2.3 FCI-CASPT2 Benchmark Study of Small Molecules

In the literature survey presented in the previous section, the performance of CAPST2 was evaluated by comparing calculated excitation energies to experimental reference data. This is commonly done by comparing vertical excitation energies computed at the FC geometry with the position of the experimental absorption band maxima. As discussed in Chapter 3, this comparison may not always be reasonable, as the bright states at the FC geometry can differ from the excited-states around the maximum of the absorption bands. Therefore, in order to compare the very same well-defined property, a benchmark study was conducted comparing the results of CASPT2 calculations with the results of FCI –a method that can be considered exact, disregarding the finite size of the basis set.

The benchmark comprised the calculations of 137 electronic states of the 12 molecules molecules shown in Figure 4.3(c). The calculations were conducted at the CASSCF/CASPT2 and FCI levels of theory using the 6-31G and 6-311G basis sets.[223,224] For the homodiatomic molecules as well as H_2O and CH_2, the frozen-core approximation was applied, so strictly speaking only the first-row hydrides included in the benchmark set were treated with FCI. The CASPT2 calculations were performed using the recommended IPEA shift value of $\varepsilon = 0.25$ a.u. ("IPEA") and setting the IPEA shift to zero ("NOIPEA"). The active spaces in the CASSCF/CASPT2 calculations comprised all valence orbitals and electrons for each molecule.

The results of the FCI-CASPT2 benchmark calculations are depicted in Figure 4.4(b). As can be seen, similar to the case of the organic molecules of the literature survey, NOIPEA CASPT2 underestimates the (FCI) reference excitation energies slightly (MSEE = −0.05 eV). When using the IPEA variant, the excitation energies increase, which results in an even better agreement with the FCI excitation energies (MSEE = −0.03 eV). This better agreement can be understood when analyzing the total energies of the ground and excited states obtained using FCI and CASPT2 [Figure 4.4(c)]. Both NOIPEA and IPEA CASPT2 show similar errors in the total ground-state energies (MSET = 0.17-0.19 eV). This is expected, as, due to their closed-shell character, the ground-state energies should not affected by the IPEA correction. For NOIPEA CASPT2, the error of the excited-state total energies is smaller (MSET = 0.14 eV) than the error of the ground-state energies, resulting in a underestimation of the excitation energies (MSEE = −0.05 eV). In contrast, for IPEA CASPT2, the error in the total energies of the excited states is increased (MSET = 0.19 eV), and, as it is closer to the MSET of the IPEA ground states, the IPEA excitation energies are less underestimated (MSEE = −0.03 eV), see Figure 4.4(d). Note that the MSEE for the whole benchmark set is not simply given by the differences of the MSET of the ground and excited states,

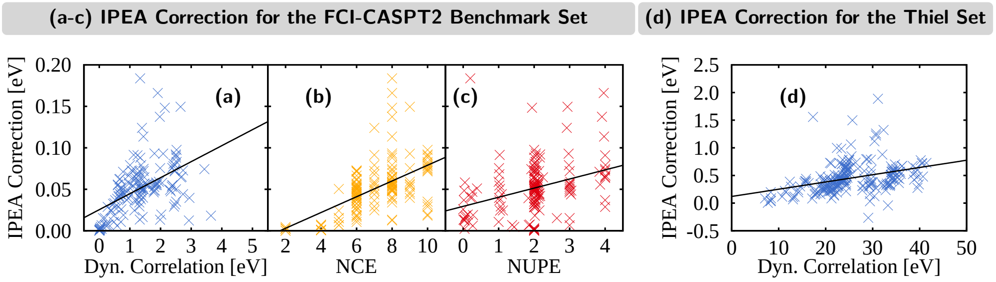

Figure 4.5: Size of the IPEA correction to the total energy (in eV) as functions of (a) the dynamical correlation energy (in eV), (b) the number of correlated electrons (NCE), and (c) the number of unpaired electrons (NUPE) of the electronic states in the FCI-CASPT2 benchmark set. (d) Size of the IPEA correction to the excitation energy (in eV) as a function of the dynamical correlation energy (in eV) of the electronic states in the Thiel benchmark set. Black lines represent linear fits of the data sets.

as a different number of excited states were included for each molecule, i.e., corresponding to each ground state.

The difference between the MSEE of the NOIPEA and IPEA calculations shows that the increase of excitation energies due to the IPEA shift amounts to ca. 0.02 eV. This increase is tiny compared to the 0.5 eV energy shifts found for the excited states of nitrobenzene and 2-nitronaphthalene (Section 4.1). This difference in the magnitude of the energy shifts is due to the fact that the size of the IPEA correction scales with the size of the system in the CASPT2 calculation. To demonstrate this for all molecules in the FCI-CASPT2 benchmark, the size of the IPEA correction is shown as functions of the dynamical correlation energy E^{dyn} and the number of correlated electrons in the CASPT2 calculation for all electronic states in Figures 4.5(a) and (b). The number of correlated electrons, i.e., the number of electrons included in the active space, is a good measure of the system size represented by the reference wave function in the CASPT2 calculation, while E^{dyn} represents the energy added by the perturbation in CASPT2. The size of the IPEA correction is simply the difference between the IPEA and NOIPEA CASPT2 energies. As best appreciated by the linear fits in Figure 4.5(a/b), the IPEA correction becomes larger when either E^{dyn} or the number of correlated electrons increase. However, for specific values of E^{dyn} or the number of correlated electrons, the IPEA correction displays quite a large spread of values, indicating that other factors affect the size of the IPEA correction as well.

The intention of the IPEA shift originally was to correct for systematic errors that were supposed to scale with the number of unpaired electrons. To test this intention, the size of the IPEA correction as a function of the number of unpaired electrons is shown in Figure 4.5(c). As can be seen, the IPEA correction does increase with the number of unpaired electrons, however, the spread of the IPEA energy correction is large for the states of the same number of unpaired electrons –certainly not an inteded behavior.

4.2.4 CASPT2 Benchmark of Thiel's Set of Organic Molecules

For the small molecules in the FCI-CASPT2 benchmark, the size of the IPEA correction increases with the size of system via, e.g., the dynamical correlation energy E^{dyn}. This scaling translates also for larger systems such as the 28 organic molecules included in Thiel's benchmark set[163] (see Figure 3.9). For these molecules, the benchmark set comprises 248 excited electronic singlet and triplet states that were calculated at MP2/6-31G* optimized FC geometries. In the original study[163], these excited states were already calculated at the MS-CASPT2[129]/TZVP[225] level of theory employing the recommended IPEA shift value of $\varepsilon = 0.25$ a.u. (IPEA). The calculations were repeated for this work using the same CASPT2 parameters –active spaces, number of states, level shifts –but setting the IPEA shift to zero (NOIPEA).

For all electronic states, the size of the IPEA correction to the excitation energies is shown as a function of the dynamical correlation energy E^{dyn} in Figure 4.5(d). As can be seen, the size of the IPEA correction scales well with E^{dyn}, and it ranges mostly between zero and one eV for the molecules of the Thiel set. The IPEA correction in average amounts to 0.45 eV which is of the same size as observed in the studies of nitrobenzene and 2NN, clarifying that these two molecules did not represent unfortunate candidates where the effect of the IPEA shift is exceedingly large. Figure 4.5(c) and (d) also show linear fits for the IPEA correction as a function of E^{dyn}. Both fit functions show similar slopes, i.e, 0.011 and 0.013 (eV IPEA correction per eV dynamical correlation energy) for the FCI-CASPT2 and Thiel benchmark sets, respectively, suggesting that this particular scaling may be a general property of IPEA-CASPT2.

Due to the large increase of the excitation energies, the IPEA shift should only be employed in cases where the NOIPEA excitation energies were considerably underestimated. This is, however, not the case for the Thiel benchmark set. For all excited states where experimental data was reported in Ref. 163, the NOIPEA excitation energies underestimate the experimental reference energies in average by 0.13 eV. Using the recommended IPEA shift value $\varepsilon = 0.25$ a.u., in turn, yields an average overestimation of 0.29 eV. Note that not for all states in the Thiel set, experimental reference energies were reported, and, thus, the difference between both errors does not equal the previously reported IPEA correction of 0.45 eV, which was the average of all calculated states. The large error of 0.29 eV of the IPEA results is due to a consistent overestimation of the experimental excitation energies. This is shown in Figures 4.6(a) and (b), where the individual errors of all excited states together with linear fits are plotted as a function of the dynamical correlation energy for $\varepsilon = 0$ (NOIPEA) and 0.25 a.u. (IPEA). As best appreciated by the linear fits, the error of the IPEA results is nearly constant throughout the ranges of dynamical correlation energies E^{dyn}. The error of the NOIPEA calculations varies more as a function of E^{dyn}, however, for the ranges of E^{dyn} that appear in the calculated excited states, it is closer to the experimental reference data, i.e., closer to the error value of zero, which, thus, leads to the smaller average error of -0.13 eV.

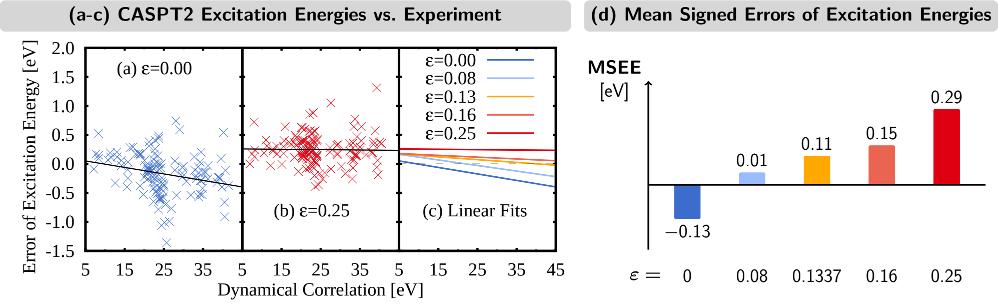

Figure 4.6: (a-c) Error of CASPT2/TZVP excitation energies compared to experimental reference data for the excited states in the Thiel benchmark set for different IPEA shift values ε. (d) Mean signed error of the CASPT2/TZVP excitation energies (MSEE) for the different IPEA shift values ε of the excited states in the Thiel benchmark set compared to experimental reference data.

The underestimation of the NOIPEA ($\varepsilon = 0$) excitation energies and the overestimation of the IPEA ($\varepsilon = 0.25$) excitation energies suggests the use of an intermediate shift value. Accordingly, three intermediate IPEA values were tested, and their errors alongside to the NOIPEA and IPEA results are shown in Figure 4.6(d). As can be seen, increasing the IPEA shift parameter gradually leads to larger, positive errors. Notably, the average error compared to the experimental energies is only 0.01 eV when using $\varepsilon = 0.08$ a.u. However, no single IPEA shift value can be favored for all excited states, since both the error of CASPT2 without an IPEA shift [Figure 4.6(a)] as well as the size of the IPEA correction [Figure 4.5(d)] depend on the dynamical correlation energy. Thus, for different ranges of dynamical correlation energies, different IPEA shift values produce the smallest errors. This is best appreciated by the linear fits of the CASPT2 errors as functions of the dynamical correlation energy for different IPEA shift values in Figure 4.6(c), that cross the line of zero error in different regions of the dynamical correlation energy.

Interestingly, using the recommended IPEA shift value $\varepsilon = 0.25$ a.u. resulted in an almost constant overestimation of ca. 0.3 eV. This suggests to use this IPEA shift and just add the subtract the remaining error as a correction to completely eliminate the average error of CASPT2 in predicting excitation energies. Alas, this convenient error cancellation is fortuitous only for the combination of the TZVP basis set with $\varepsilon = 0.25$ a.u., as was found when the CASPT2 calculations for the Thiel benchmark set were repeated using the ANO-RCC in different sizes (MB, VDZ, VDZP, VTZP, VQZP) and different IPEA shift values of $\varepsilon =$ 0-0.5 a.u. The average errors obtained for all combinations are shown in Figure 4.7(a). As can be seen for every basis set, increasing the IPEA shift leads to an increase of the excitation energies which shifts the average errors to larger, more positive values. However, increasing the basis set sizes decreases the excitation energies for a given IPEA shift value, so that the average errors are shifted towards smaller, more negative values. When using the smaller basis

(a) MSEE of CASPT2 for Different Basis Sets and IPEA Shift Values ε

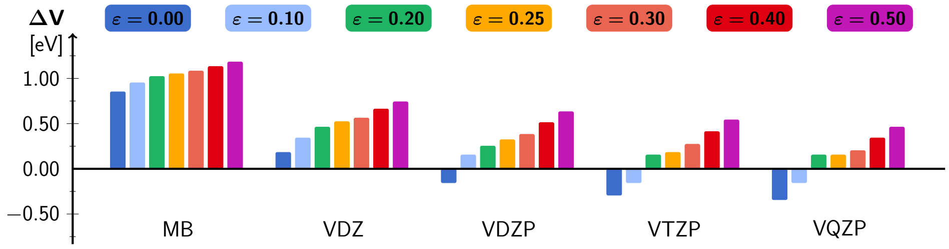

(b) Error of CASPT2 Excitation Energies as a Function of the Dynamical Correlation Energy

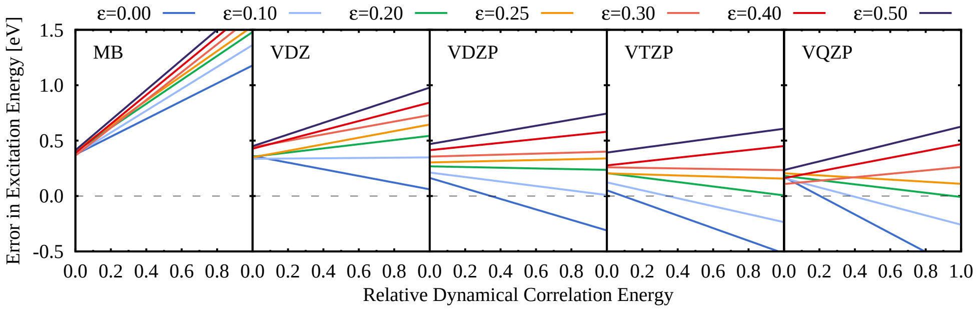

(c) Performance of Electronic Structure Methods for the Thiel Benchmark Set

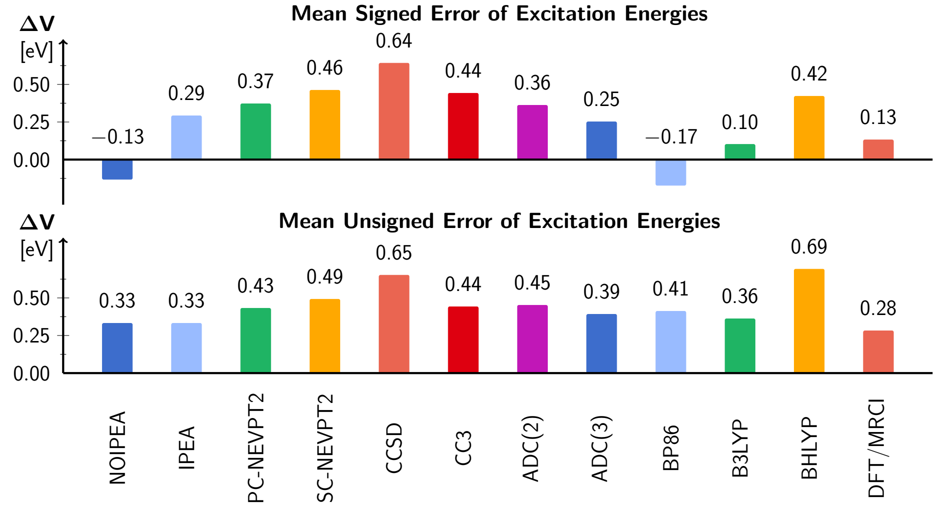

Figure 4.7: (a) Mean-signed errors of CASPT2 excitation energies (MSEE) of the excited states in the Thiel benchmark set for different ANO-RCC basis sets and IPEA shift values ε compared to experimental reference data. (b) Errors of the CASPT2 excitation energies for the different ANO-RCC basis sets and IPEA shift values as a function of the relative dynamical correlation energy $E^{\text{dyn}}_{\text{rel}}$. $E^{\text{dyn}}_{\text{rel}}(i;j)$ of a state Ψ_i in the basis $\{j\}$ is obtained by scaling the total dynamical correlation energy $E^{\text{dyn}}(i;j)$ to fit into the interval of $[0,1]$, where $E^{\text{dyn}}_{\text{rel}} = 1$ for the state Ψ_p with the largest total dynamical correlation energy $E^{\text{dyn}}(p;j) = E^{\text{dyn}}_{\text{max}}(j)$ in basis $\{j\}$. (c) Mean signed and unsigned errors of excitation energies (MSEE/MUEE) of different electronic structure methods for the excited states in the Thiel benchmark set compared to experimental reference data. All methods used the TZVP basis set.

sets (MB, VDZ), CASPT2 constantly overestimates the excitation energies so that the error is minimal for $\varepsilon = 0$. For the larger basis sets (VDZP, VTZP, VQZP), the sign of the error depends on the IPEA shift value. Here, neither $\varepsilon = 0$ nor the recommended $\varepsilon = 0.25$ a.u. yield the smallest average error, but the best agreement with experiment is found for intermediate shift values.

As found for the TZVP basis set, the error of the individual excitation energies varies with the dynamical correlation energy of the excited states also for the ANO-RCC basis sets. This is shown in Figure 4.7(b). It can be seen, e.g., that $\varepsilon = 0$ yields the smallest errors for the MB and VDZ basis sets. $\varepsilon = 0$ also gives the smallest errors for the VDZP basis set, however, only for small values of the dynamical correlation energy. For the VTZP and VQZP basis sets, $\varepsilon = 0$ underestimates the experimental excitation energies for most ranges of the dynamical correlation energy, and for these basis sets, $\varepsilon = 0.1$ and 0.2 a.u. perform better for intermediate and large values of the dynamical correlation energy, respectively. Nevertheless, these results demonstrate that there is no single, favorite IPEA shift for which errors are consistently small for all basis sets and independent of the size of dynamical correlation energy.

The use of the IPEA shift in computing excitation energies is an intricate problem due to its effect depending on the dynamical correlation energy and the basis set. Clearly, it is dissatisfying and against the spirit of an ab initio method to have to select a different IPEA value for each new problem to study. In this regard, one might wonder how adequate CASPT2 is in comparison with other methods, i.e., whether discussing the IPEA dilemma in CASPT2 is even worth the trouble. Fortunately, the excited states in the Thiel benchmark set have been studied in the past at various levels of theory besides CASPT2, i.e., coupled-cluster (CC2, CCSD, CC3)[163], NEVPT2[226], ADC(2)/ADC(3)[227], TDDFT (BP86, B3LYP BHLYO)[228] and hybrid DFT/MRCI approach.[228] All studies used the same TZVP basis set[225], thus, allowing for direct comparison.

For all methods, the mean signed and unsigned errors of excitation energies (MSEE/MUEE) compared to experimental reference data are shown in Figure 4.7(c). As can be seen, among the wave-funtion based methods, both NOIPEA ($\varepsilon = 0$) and IPEA ($\varepsilon = 0.25$ a.u.) CASPT2 variants yield the smallest MUEE (0.33 eV). Thereby, the MSEE of the IPEA variant is larger than that of the NOIPEA variant due to the very consistent overestimation of excitation energies. Among these methods, only NOIPEA CASPT2 underestimates the experimental excitation energies, while other rather well-trusted wave-function methods show a surprisingly large overestimation of the excitation energies that reaches 0.64 eV for CCSD. Unsurprisingly, for TDDFT, the size and the sign of the error depend on the functional used, where the best performance is obtained using B3LYP which displays an overall smallest MSEE of only 0.10 eV. An excellent performance is also obtained for DFT/MRCI with a MSEE of 0.13 eV and an MUEE of 0.28 eV, which is the smallest error of all methods.

4.3 Conclusions on the IPEA Shift in CASPT2

The IPEA shift was originally introduced to correct for errors found when computing dissociation energies of small molecules, which were calculated too low. This behavior was attributed to a general underestimation of the energies of open-shell states that scaled with 0.13-0.26 eV per open shell. This underestimation was assumed to be present also when calculating excited states. This claim, however, could be rebuked by an extended literature survey collecting the excitation energies of organic molecules and metal complexes published prior to the introduction of the IPEA shift. For organic molecules, the excitation energies were slightly underestimated by 0.02 eV, i.e., an order of magnitude smaller than expected, while those of the metal complexes were slightly overestimated by 0.02 eV.

To obtain a more detailed picture of the performance of CASPT2 and the role of the IPEA shift, benchmark calculations for a set of di- and triatomic molecules were performed and the results of CASPT2 with and without the recommended IPEA shift value of $\varepsilon = 0.25$ a.u. were compared against FCI results. Without the IPEA correction, the CASPT2 excitation energies were only slightly underestimated by 0.05 eV, and this underestimation could be reduced to 0.03 eV when using $\varepsilon = 0.25$ a.u. The smaller error in the excitation energies due to the use of the IPEA shift, however, originated from an increase of the error of open-shell states –that better cancels with the large error of the closed-shell states –rather than a decrease of the error of open-shell states. Importantly, it was observed that the size of the IPEA correction –in average 0.02 eV for the di-/triatomic molecules –scaled with the size of the molecule as measured by its dynamical correlation energy.

The scaling of the IPEA correction with the system size was also found for the larger organic molecules in the Thiel benchmark set. For these molecules, the average increase of the CASPT2/TZVP excitation energies amounted to 0.45 eV when using the recommended $\varepsilon = 0.25$ a.u. IPEA shift. Without the IPEA shift, the CASPT2/TZVP excitation energies for the molecules in the Thiel set were underestimated by 0.13 eV compared to experiment. Thus, using the recommeded IPEA shift for these states deteriorated the agreement with experiment, leading to a larger overestimation of 0.29 eV. Although it was possible to find an IPEA shift value intermediate between zero and the recommended $\varepsilon = 0.25$ a.u., that minimized the average error, it was found that the individual excited states still demanded different IPEA shifts that were correlated to their dynamical correlation energy. Even worse, this correlation changes when a different basis set is used, making the ideal IPEA shift value depending on the system size and the basis set –very much against the spirit of an ab initio method. For basis sets of double-zeta quality, the smallest average errors of the excitation energies for the Thiel set are obtained by setting the IPEA shift to zero, while larger basis sets demand larger IPEA shifts –that are, however, still below the recommended $\varepsilon = 0.25$ a.u. This suggests the pragmatic approach of neglecting the IPEA shift and just using basis sets of double-zeta quality for excited-state CASPT2 calculations of organic molecules.

Comparing to calculations using other high-level electronic structure methods, it was reassuring that CASPT2 calculations without the IPEA shift still yielded one of the best agreements with experimental data. However, this conclusion might be applicable only to excited states of organic molecules. Although the literature survey revealed no underestimation of excitation energies of metal complexes in CASPT2 studies published before the introduction of the IPEA shift, and, thus, no need to use the IPEA shift for these systems, more recent work concerned on the high-spin/low-spin gaps of six-coordinate iron(II) complexes and similar compounds indicates that, in such cases, the IPEA shift is necessary. Interestingly, also for these systems, there is controversy about the adequate IPEA shift value. In contrast to the organic molecules studied here, however, these studies debate whether the recommended[229–232] $\varepsilon = 0.25$ a.u. or even larger[172,233–235] IPEA shift values are necessary. Cleary, this is an interesting question for future studies.

5 Excited-State Dynamics Simulations of Nitronaphthalene Derivatives

This chapter presents the results of the excited-state dynamics simulations of the three NPAHs: 2NN, 1NN, and 2M1NN (Figure 5.1). These NN derivatives are reported to exhibit the fastest ISC measured for organic molecules solely composed of light atoms.[13] The very short time scale of this process minimizes the required simulation time to study their excited-state dynamics, and their small size makes the electronic structure calculations done at each time step affordable. Thus, the NN derivatives represent ideal systems for the first excited-state dynamics simulations to investigate the ultrafast ISC found in many NPAHs.

5.1 Previous Studies on Nitronaphthalene Derivatives

The first evidence for ultrafast ISC in NN derivatives was found in femtosecond fluorescence up-conversion experiments in 2007.[2] In this study, ISC was assumed to occur in less than 100 fs after excitation to the lowest-energy absorption band for 1NN in MeOH. This suggestion was motivated by results of early semi-empirical calculations[236] from 1972, which reported the presence of triplet excited states with energies similar as the bright excited states at the FC geometry. In the same experimental study[2], other NPAHs were investigated exhibiting a similarly fast sub-100 fs decay time. However, for these NPAHs, the decay time was attributed to dynamics in the singlet excited states involving a re-orientation of the nitro group. Later fluorescence up-conversion studies on 1NN in different solvents[4] and sub-ps-resolved transient-absorption spectroscopy experiments of 1NN in MeOH[6] reassured that the decay of the initially excited singlet state occurs within 100 fs. Additionally, it was reported that relaxation within the triplet manifold ($T_n \rightarrow T_1$) proceeded on a time scale of 1-16 ps.

Further transient-absorption spectroscopy experiments[11,13,139] on 1NN as well as on 2NN and 2M1NN showed that, after excitation to the lowest-energy absorption band, all three NN derivatives exhibit multiexponential decay signals with similar life times in the orders of $\tau_1 \sim$ 0.1-0.4 ps, $\tau_2 \sim$ 1-3 ps, and $\tau_3 \sim$ 6-10 ps (see Figure 5.1). For 2NN, the time constants were assigned to ISC from the singlet to the triplet states (τ_1), IC within the triplet manifold (τ_2), and vibrational cooling in the hot T_1 state (τ_3). The assignment of lifetimes for 1NN and 2M1NN was similar. However, since 1NN and 2M1NN exhibit also partial photodegradation upon UV irradiation in contrast to 2NN, τ_1 was supposed to describe a bifurcation of the initial excited-state dynamics into ISC to the triplet states and conformational relaxation to a dissociative singlet state.

Properties of Nitronaphthalene Derivatives

	2NN		**1NN**		**2M1NN**	
Molecule	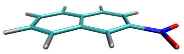		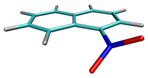		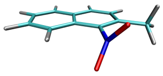	
Solvent	MeCN	Cyclohexane	MeCN	Cyclohexane	MeCN	Cyclohexane
τ_1 [ps]	0.17 ± 0.05	0.11 ± 0.05	0.14 ± 0.05	0.11 ± 0.05	0.21 ± 0.05	0.37 ± 0.07
τ_2 [ps]	1.9 ± 0.2	2.1 ± 0.1	2.8 ± 0.2	2.3 ± 0.2	0.6 ± 0.1	1.4 ± 0.3
τ_3 [ps]	9.1 ± 0.1	10 ± 1	11.2 ± 0.4	10.3 ± 0.3	5.9 ± 0.3	7.1 ± 0.9
γ [°]	0.3	0.1	33.9	33.1	55.4	58.6
$\Phi_{\mathrm{trip}}^{\mathrm{N_2}}$	0.93 ± 0.15	–	0.64 ± 0.12	–	0.33 ± 0.05	–
$\Phi_{\mathrm{deg}}^{\mathrm{N_2}}$	~ 0	–	0.0035 ± 0.0004	–	0.123 ± 0.008	–
$\Phi_{\mathrm{deg}}^{\mathrm{air}}$	–	–	0.0015 ± 0.0004	–	0.043 ± 0.002	–
$\Phi_{\mathrm{deg}}^{\mathrm{O_2}}$	–	–	0.0013 ± 0.0002	–	0.023 ± 0.002	–

Figure 5.1: Time constants τ_i of excited-state dynamics of three NN derivatives obtained from transient-absorption spectroscopy experiments in MeCN and cyclohexane.[11] Nitro-group torsion angle γ with respect to aromatic ring plane at the FC geometry.[13] Triplet and photodegradation quantum yields Φ_{trip} and Φ_{deg}, respectively, measured in MeCN saturated by N_2, air, or O_2.[13,139]

The different behavior of 2NN and 1NN/2M1NN in their excited-state dynamics was attributed to the conformational control of the nitro group torsion in the electronic ground state. When the nitro group torsion angle γ in the ground-state minimum-energy geometry (Figure 5.1) tends to zero, the triplet quantum yield $\Phi_{\mathrm{Trip}}^{\mathrm{MeCN,N_2}}$ of the molecules in N_2 saturated solutions of MeCN increased while the photodegradation quantum yield $\Phi_{\mathrm{deg}}^{\mathrm{MeCN,N_2}}$ decreased.[13] Thus, it was concluded that the small torsion angles in 2NN directed the dynamics only towards ISC after photoexcitation, while the larger angles in 1NN/2M1NN allowed also the population of the dissociative singlet state. While the relationship of inverse proportion of $\Phi_{\mathrm{Trip}}^{\mathrm{MeCN}}$ and $\Phi_{\mathrm{deg}}^{\mathrm{MeCN,N_2}}$ seemed to confirm the proposed mechanism including the bifurcation of the dynamics in 1NN and 2M1NN, it was also found that the photodegradation quantum yield decreased significantly if the experiments were conducted in air- or O_2-saturated solutions of MeCN instead ($\Phi_{\mathrm{deg}}^{\mathrm{MeCN,air}}$, $\Phi_{\mathrm{deg}}^{\mathrm{MeCN,O_2}}$).[139] Usually, the effect of the molecular oxygen concentration on the photodegradation quantum yield is a sign of the involvement of triplet states in the photodegradation reaction. Due to the small energy gap between the triplet ground state and the first excited singlet state in molecular oxygen, triplet-triplet energy transfer from the triplet states of chromophores to molecular oxygen is relatively easy, which can effectively quench the population of longer-lived triplet states in the chromophores. However, in the case of the NN derivatives, it rather was assumed that molecular oxygen can react with a radical intermediate appearing in the dissociation pathway, scavenging the radical character of the intermediate so that the NN derivative can safely return to the ground state.[139]

In addition to the experimental work, the excited-state dynamics of 1NN were investigated in two studies that performed static calculations at the CASSCF/ CASPT2 level of theory. In the first study[237], the minimum-energy path of the S_1 state, a state of mixed $\pi\pi^*/n\pi^*$ character, was calculated starting at the FC geometry. Along the minimum-energy path, this S_1 state showed significant SOCs of ca. 65 cm^{-1} with the T_2 state, a $\pi\pi^*$ state, with energy differences as small as 0.1-0.2 eV between the two states.[237] Based on these results, the rate constant of ISC was estimated using Fermi's golden rule as $k_{\mathrm{ISC}} = 1.8$-$5.2 \cdot 10^{11}\ \mathrm{s}^{-1}$, which corresponds to a time constant of $\tau_{\mathrm{ISC}} = 1.9$-$5.2$ ps. These results were confirmed in the second study, where also the minimum-energy path of the S_1 starting at the FC geometry was calculated, and a crossing point between the $S_1(n\pi^*)$ and $T_2(\pi\pi^*)$ state with a large SOC of 66 cm^{-1} was identified.[238] Although the calculated rate of ISC is quite large for an organic molecule, it is still 20-50 times smaller than that obtained in the experiments.[11] Thus, to obtain a clear picture of the processes after photoexcitation and understand the reasons behind their ultrafast ISC, in this thesis, the excited-state dynamics of the three NN derivatives were simulated explicitely, starting with 2NN.

5.2 The Mechanism of Ultrafast ISC in 2NN

The excited-state dynamics of 2NN in the gas phase were simulated using the SHARC method.[71,72,106] The potential energies, gradients, NACs, and SOCs were calculated at the PBE0[147,239]/DZP[240] level of theory using the ADF2016 program package.[241] This level of theory was chosen as it was already found that PBE0 is able to reproduce the absorption spectrum of 2NN in MeOH (see Section 3.3). Although there is no experimental gas-phase absorption spectrum of 2NN to use as a reference, it can be noted that the PBE0/DZP calculated gas-phase absorption spectrum of 2NN agrees also well with an experimental absorption spectrum of 2NN in the nonpolar solvent n-heptane[148] as shown in Figure 5.2(a). Note also the small differences between the experimentally obtained time constants of all three NN derivatives in MeCN and cyclohexane in Figure 5.1, which indicate that solvent effects are negligible in the excited-state dynamics. The initial conditions for the SHARC simulations were sampled from a Wigner distribution of 1000 geometries at $T = 300$ K. Using this ensemble, the absorption spectrum of 2NN was calculated. For the SHARC simulations, 99 trajectories were started at stochastically selected bright states[242] in an energy range of 0.5 eV around the maximum of the lowest-energy absorption band [gray area in Figure 5.2(a)]. The trajectories were propagated for 500 fs.

The results presented in this chapter have been published in the study "Mechanism of Ultrafast Intersystem Crossing in 2-Nitronaphthalene" in Chemistry –A European Journal.[243]

5.2.1 Excited-State Relaxation Mechanism

According to the experimental conditions, the SHARC simulations are started by exciting to electronic states around the maximum of the lowest-energy absorption band [see Figure 5.2(a)]. Thus, initially, the population is roughly equally distributed over the MCH states S_1 and S_2 [see Figure 5.2(b)]. From the beginning of the simulations, the population of the S_2 state decreases while that of the S_1 state, the higher-lying triplet states T_n (n = 2-6), and the T_1 state increase. After ca. 100 fs, the S_1 population stops growing and begins to decrease. After ca. 200 fs the T_n population becomes steady, so that at later simulation times only the T_1 population continues to grow. This behavior of the MCH state populations can be explained by the simple kinetic model

$$\mathrm{S}_2 \xrightarrow{\tau_S} \mathrm{S}_1 \xrightarrow{\tau_{ISC}} \mathrm{T}_n \xrightarrow{\tau_T} \mathrm{T}_1. \tag{5.1}$$

Here, the triplet states are subdivided into T_n (n = 2-6) and T_1. This subdivision was motivated as analyzing the hops of the individual trajectories showed no ISC directly from the singlet states to the T_1. Based on eq. (5.1), the time evolution of the MCH state populations can be described by mono-exponential functions. For these functions, using the bootstrap method[244] with 100 copies, a fit yielded the time constants $\tau_S = 56 \pm 8$ fs, $\tau_{ISC} = 710 \pm 101$ fs, and $\tau_T = 149 \pm 20$ fs.

These time constants, however, may not be compared directly to the ones obtained in experiment for two reasons. First, as the time constants describe transitions between MCH states in the dynamics, they can include adiabatic IC and nonadiabatic IC processes. Adiabatic IC occurs when the active state of the trajectory simply changes in the energetic ordering with another state, which leaves the properties of the active state unaffected. In contrast, nonadiabatic IC occurs when the trajectory hops between two states of different electronic character. In the experiment, only the latter process can likely be monitored, so to compare the calculated results with experimental results, the nonadiabatic transitions have to be identified. Note that for ISC processes, a similar problem does not appear since a transition from a singlet to a triplet state changes the properties of the active electronic state in every case.

When analyzing the initial excited states in the trajectories $-\langle \mathrm{S}_1(t = 0)\rangle$ and $\langle \mathrm{S}_2(t = 0)\rangle$ –it is found, that all trajectories start in electronic states of similar character. These states correspond to the S_1 state at the FC geometry (S_1@FC). This is shown in Figure 5.2(c) where the atomic hole/electron difference populations, CT numbers, and exciton sizes are reported as obtained by an analysis of the transition-density matrix using the TheoDORE package (see section 2.3.5).[87–90] As can be seen, these transition-density properties are very similar for the initially excited states in the trajectories ($\langle \mathrm{S}_{1,2}(t = 0)\rangle$) and the S_1@FC state, while they deviate considerably from that of the S_2@FC state. Thus, at least part of the IC between the MCH states $S_2(t)$ and $S_1(t)$ included in τ_S will correspond to transitions between adiabatic states.

Characterized by their natural-transition orbitals (NTOs) in Figure 5.2(d), the S_1@FC and S_2@FC states can be described by a $\pi\pi^*$ transition involving CT from the aromatic ring to the nitro group [S_1@FC = $\mathrm{S}_{\mathrm{CT}}(\pi\pi^*)$] and a $n\pi^*$ local excitation (LE) at the nitro group [S_2@FC = $\mathrm{S}_{\mathrm{LE}}(n\pi^*)$], respectively. As will be shown in Section 5.2.2, the major part of ISC involves transitions from the states of $\mathrm{S}_{\mathrm{LE}}(n\pi^*)$ character to the triplet manifold. Thus, the initial dynamics in the singlet states prior to ISC must contain also nonadiabatic IC between

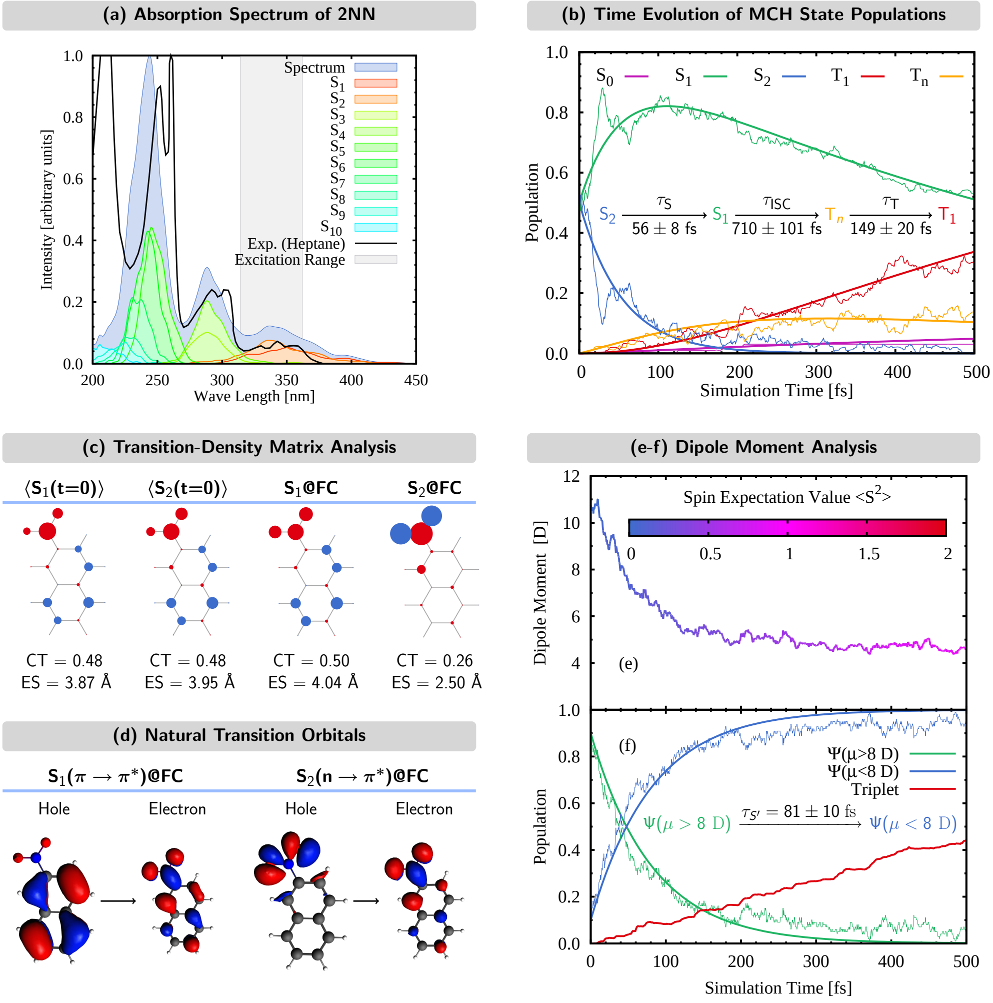

(a) Absorption Spectrum of 2NN

(b) Time Evolution of MCH State Populations

(c) Transition-Density Matrix Analysis

(d) Natural Transition Orbitals

(e-f) Dipole Moment Analysis

Figure 5.2: (a) Calculated absorption spectrum of 2NN in gas phase with individual state contributions and experimental absorption spectrum of 2NN in n-heptane.[148] Gray area denotes the excitation-energy range used in the initial conditions of the dynamics simulations. (b) Time evolution of the MCH state populations (thin lines) as well as fit functions of the populations (thick lines) based on the kinetic model shown in the graph. (c) Transition-density matrix analysis of the initially excited $S_1(t = 0)$ and $S_2(t = 0)$ states in the dynamics as well as of the S_1 and S_2 states at the FC geometry. Circles correspond to atomic hole/electron difference populations (blue: positive, red: negative) while CT and ES denote the charge-transfer number and exciton size, respectively. (d) Natural transition orbitals of the S_1 and S_2 states at the FC geometry. (e) Time evolution of the dipole moment $\mu(t)$ averaged for all trajectories. (f) Time evolution of the population of MCH states with $\mu > 8$ D and $\mu < 8$ D and of all triplet states (thin lines) as well as fit functions (thick lines) based on the kinetic model shown in the graph.

the initially excited $S_{CT}(\pi\pi^*)$-type states and the $S_{LE}(n\pi^*)$-type states.

Because of the different electronic character of both states, the population transfer between them can be monitored along the simulations by the dipole moment of the active state. This is done in Figure 5.2(e), which shows the time evolution of the average dipole moment $\langle\mu(t)\rangle$ of all trajectories. At the beginning of the simulations $\langle\mu(t)\rangle \sim$ 10-11 D, before it decreases to ca. 5 D after 150 fs and stays constant for the remainder of the 500 fs simulation time. The former value of 10-11 D is similar to the dipole moment $\mu = 12.9$ D of the $S_{CT}(\pi\pi^*)$ state at its mimimum-energy geometry, while the final value of 5 D is close to the dipole moment of $\mu = 3.7$ D of the $S_{LE}(n\pi^*)$ state at its minimum-energy geometry. Thus, the decrease of $\langle\mu(t)\rangle$ is a sign of the continous population transfer from the $S_{CT}(\pi\pi^*)$ to the $S_{LE}(n\pi^*)$ state.

In order to calculate the time constant for the $S_{CT}(\pi\pi^*) \rightarrow S_{LE}(n\pi^*)$ IC, the active states of trajectories in the simulations were assigned to either $S_{CT}(\pi\pi^*)$ or $S_{LE}(n\pi^*)$ if $\mu(t) > 8$ D or $\mu(t) < 8$ D, respectively. Using this classification, a time constant of $\tau_{S'} = 81 \pm 10$ fs is calculated for the nonadiabatic population transfer [Figure 5.2(f)]. Note that the above classification is applicable when the excited-state population is still for the most part in the two singlet states and the population of the triplet states is small. As this is the case in the beginning of the simulation time [Figure 5.2(f)], $\tau_{S'}$ can indeed be used to describe the dynamics in the singlet manifold.

Second, if a slow reaction is followed by a fast reaction, it can be difficult to monitor both processes separately in the experiment. The resolution of the fast reaction can be lost. This may lead an unaware observer to mistake that only a single reaction occurs, i.e., the slower one, for which an effective time constant is measured. This indeed can be the case for the slow singlet-to-triplet ISC ($\tau_{ISC} = 710$ fs) that is followed by fast IC from the higher-lying triplet states T_n to the T_1 ($\tau_T = 150$ fs). Considering both processes as one, an effective ISC time constant of $\tau_{ISC'} = 968 \pm 142$ fs can be calculated based on the kinetic model

$$S_2 \xrightarrow{\tau_S} \text{Intermediate Species} \xrightarrow{\tau_{ISC'}} T_1, \tag{5.2}$$

where the intermediate species is simply the combination of S_1 and T_n states.

Comparing the time constants $\tau_{S'} = 81 \pm 10$ fs and $\tau_{ISC'} = 968 \pm 142$ fs to the experimental results (Figure 5.1), one finds that $\tau_{S'}$ and $\tau_{ISC'}$ can be attributed to the time constants of the two initial processes observed experimentally, for which time constants of $\tau_1 = 110 \pm 50$ fs and $\tau_2 = 2.1 \pm 0.1$ ps were reported for 2NN in cyclohexane.[13] Note that, although there is a difference between $\tau_{ISC'}$ and τ_2, both are of the same order of magnitude. However, while in this work, $\tau_{S'}$ and $\tau_{ISC'}$ were assigned to IC in the singlet states and ISC in combination with relaxation within the triplet manifold, respectively, in the experimental studies, τ_1 was assigned to ISC while τ_2 was assigned to IC within the triplet manifold. The experimental assignment was based on the assumption that after excitation to the lowest-energy singlet state S_1, 2NN can only relax further via ISC to the triplet states, i.e., the potential presence of another singlet excited state was not considered.[11,13,139] Following this erroneous view, it was further assumed that ISC occured from the initially excited singlet state of $\pi\pi^*$ character to a triplet state of $n\pi^*$ character. However, as will be shown in Section 5.2.2, while this ISC pathway is also found in the simulations, it accounts only for a minor fraction of the total ISC rate.

According to the experimental assignment of τ_2, IC within the triplet manifold is assumed to take place in a time window of 2 ps, while in the mechanism introduced in this work, it only requires $\tau_T = 149 \pm 20$ fs, i.e., it is taking place on a similar time scale as the IC within the singlet states ($\tau_S/\tau_{S'}$). The twofold difference between the rate of both IC processes can be attributed to the fact that IC in the singlets involves only a single transition between two singlet states. In contrast, relaxation in the triplets requires consecutive ICs through multiple triplet states and, consequently, is slower. The similar IC time constants obtained suggest a consistent description of the excited-state dynamics, thus, further supporting the mechanism proposed in this work in contrast to the previously suggested mechanims based on experimental results. The third time constant obtained in experiment, τ_3 = 6-10 ps, is too large to be reproduced in the 500 fs simulations of this work, and, thus, is left out of the discussion.

5.2.2 Electronic Structure in the ISC Pathways

After excitation to the $\mathrm{S_{CT}}(\pi\pi^*)$ state, 2NN undergoes IC to a $\mathrm{S_{LE}}(n\pi^*)$ state on a time scale faster than ISC occurs. Analyzing the electronic states at the geometries where ISC hops occur, ISC is found to happen from either of the two singlet states. When in the $\mathrm{S_{LE}}(n\pi^*)$ state, the molecule transfers to a locally excited $\pi'\pi^*$ triplet state [$\mathrm{T_{LE}}(\pi'\pi^*)$] during ISC, while when in the $\mathrm{S_{CT}}(\pi\pi^*)$ state, the molecule transfers to a locally-excited $n\pi^*$ state [$\mathrm{T_{LE}}(n\pi^*)$]. The NTOs describing both singlet and both triplet states are shown in Figure 5.3(a). As can be seen, the electron NTOs (π^*) of the $\mathrm{S_{LE}}(n\pi^*)$ and $\mathrm{T_{LE}}(\pi'\pi^*)$ states are very similar. Thus, the net electron transfer during this ISC hop is from the π' orbital to the n orbital –or, in other words: the hole is transferred from the n orbital in the singlet state to the π' orbital in the triplet state, as shown in Figure 5.3(b). Since both, the π' and n orbital are located at the nitro group, $\pi' \rightarrow n$ represents a localized electronic transition, and the corresponding ISC pathway is labeled accordingly as localized-electronic (LE) pathway. The electron NTOs ("π^*") of the $\mathrm{S_{CT}}(\pi\pi^*)$ and $\mathrm{T_{LE}}(n\pi^*)$ are also similar [Figure 5.3(a)], so that the net electron transfer in this ISC pathway simply is $n \rightarrow \pi$. As the π orbital is located at the aromatic ring system while the n orbital is at the nitro group, this transition is of CT character, and the corresponding ISC pathway is, thus, labeled charge-transfer (CT) pathway [Figure 5.3(b)].

Analyzing all ISC hops, it is found that the LE pathway accounts for ca. 91 % of the ISC hops while only 9 % of ISC hops occur via the CT pathway. The favoring of the LE pathway is partially due to the fact that its singlet donor state, the $\mathrm{S_{LE}}(n\pi^*)$, is gradually populated during the dynamics while the donor state of the CT pathway [$\mathrm{S_{CT}}(\pi\pi^*)$] is depopulated. However, the LE pathway is also favored by the larger SOC between the singlet donor and triplet acceptor states, which increases the probability for this transition. At the hopping geometries of the LE pathway, the SOC between the $\mathrm{S_{LE}}(n\pi^*)$ state and the $\mathrm{T_{LE}}(\pi'\pi^*)$

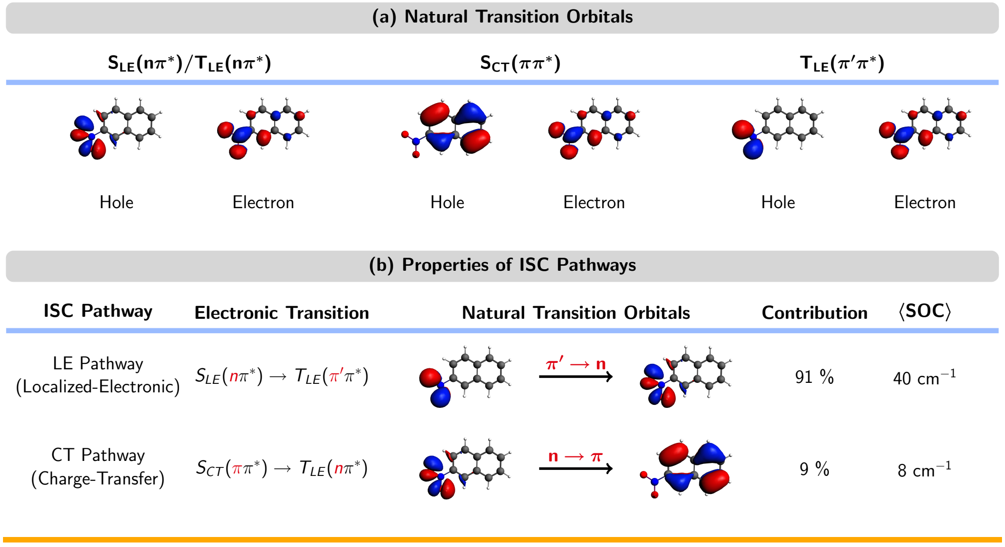
(a) Natural Transition Orbitals
$S_{LE}(n\pi^*)/T_{LE}(n\pi^*)$
$S_{CT}(\pi\pi^*)$
$T_{LE}(\pi'\pi^*)$
Hole
Electron
Hole
Electron
Hole
Electron
(b) Properties of ISC Pathways
ISC Pathway
Electronic Transition
Natural Transition Orbitals
Contribution
⟨SOC⟩
LE Pathway (Localized-Electronic)
$S_{LE}(n\pi^*) \rightarrow T_{LE}(\pi'\pi^*)$
$\pi' \rightarrow n$
91 %
40 cm^{-1}
CT Pathway (Charge-Transfer)
$S_{CT}(\pi\pi^*) \rightarrow T_{LE}(n\pi^*)$
$n \rightarrow \pi$
9 %
8 cm^{-1}

Figure 5.3: (a) Natural transition orbitals describing the electronic states involved in the ISC pathways. (b) Properties of the LE and CT ISC pathways.

state is in average 40 cm^{-1} while it is only 8 cm^{-1} for the $S_{CT}(\pi\pi^*)$ state and the $T_{LE}(n\pi^*)$ state of the CT pathway. The larger SOC in the LE pathway may be explained by the fact that the orbitals involved in the $\pi' \rightarrow n$ transition are located at the nitro group and share a strong resemblence. Both orbitals are mainly antisymmetric linear combinations of atomic p-orbitals located at the oxygen atoms of the nitro group, which lie either on the molecular plane $(p^{(x,y)}_{O_1} - p^{(x,y)}_{O_2} \rightarrow n)$ or perpendicular to it $(p^{(z)}_{O_1} - p^{(z)}_{O_2} \rightarrow \pi')$. The $\pi' \rightarrow n$ electron transfer is, thus, realized simply by changing the angular momentum of the electron in the p orbitals of the oxygen atoms, going from $p^{(z)}$ to $p^{(x,y)}$ –a process following textbook El-Sayed rules.[94] In contrast, the orbitals in the $n \rightarrow \pi$ transition of the CT pathway are located at different fragments of the molecule. Thus, in addition to the change of angular momentum, the $n \rightarrow \pi$ transition requires further charge re-distribution throughout the molecule.

5.2.3 Nuclear Motion Towards ISC

After characterizing the electronic states involved in ISC, the nuclear motion governing the excited-state dynamics of 2NN can be identified. For this, a normal-mode analysis (NMA)[245,246] was performed, in which the nuclear motion in the dynamics is expressed in terms of displacements of the normal modes determined at the FC geometry. To identify the nuclear motions that drive the molecule towards ISC, the normal-mode displacement at the initial conditions and at the ISC hopping geometries of the LE and CT pathways were calculated. As can be seen in Figure 5.4(a), the NMA showed very large displacements for the normal modes 19, 27, 29, 36, and 43 at the geometries of either the LE or CT pathway while the displacements are close to zero in the initial conditions –as expected from a harmonic Wigner distribution. Thus, it is the motion of

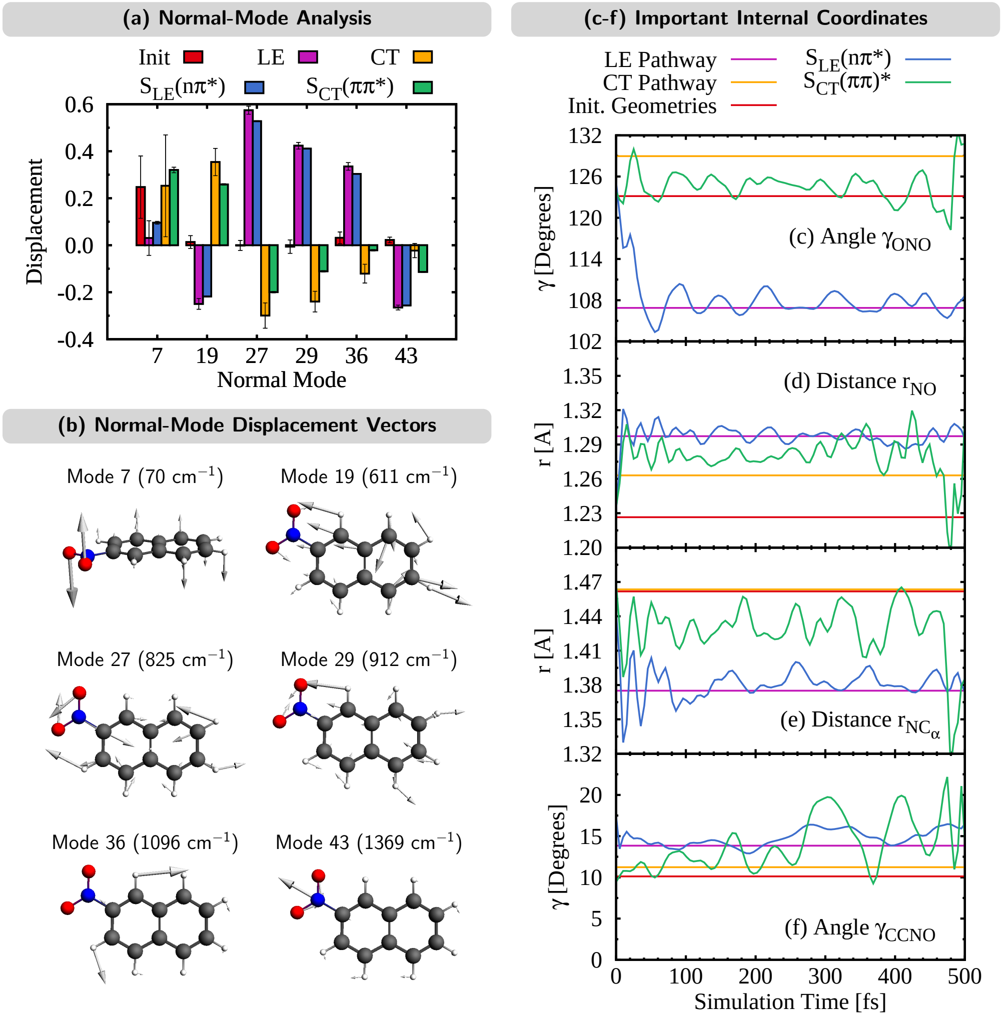

Figure 5.4: (a) Normal-mode analysis showing the average displacements of mode 7 (nitro group torsion) and the most active modes during the dynamics for the geometries in the initial conditions, the ISC hopping geometries of the LE and CT pathways, and the geometries of trajectories in either the $\mathrm{S}_{\mathrm{LE}}(n\pi^*)$ or $\mathrm{S}_{\mathrm{CT}}(\pi\pi^*)$ state. (b) Normal mode displacement vectors of mode 7 and the most active modes during the dynamics. (c-f) Averages of selected important coordinates at the hopping geometries of the LE (violet) and CT (orange) ISC pathways, and in the initial conditions (gray), as well as the time evolution of the internal coordinates for the corresponding trajectories in the $S_{LE}(n\pi^*)$ (blue) or $S_{CT}(\pi\pi^*)$ (green) state.

these normal modes that drives the system towards ISC. With the exception of mode 43, the normal-mode displacements at the hopping geometries of the LE and CT pathways are of opposite sign, meaning that both ISC pathways take place at distinct, well-separated regions of the PES. Figure 5.4(a) also shows the average normal-mode displacement of the molecule when it is in either of the ISC singlet donor states, i.e., the $S_{LE}(n\pi^*)$ or the $S_{CT}(\pi\pi^*)$ state. As can be seen, the differences between the displacements of the $S_{LE}(n\pi^*)$ state and the LE pathway hopping geometries are smaller than those of the $S_{CT}(\pi\pi^*)$ state and the CT pathway hopping geometries. This is another factor favoring the LE pathway over the CT pathway: while in the $S_{LE}(n\pi^*)$ state, the molecule is in average closer to a ISC hopping region (LE pathway geometries) than while in the $S_{CT}(\pi\pi^*)$ state, thus, requiring less structural changes to reach an ISC hopping point.

The results from the NMA can also be translated into internal coordinates. The internal coordinates important for the dynamics can be identified by looking at the displacement vectors of the normal modes as shown in Figure 5.4(b): the angle γ_{ONO} between the atoms of the nitro group, the distances r_{NO} between the N and the O atoms, and the distance r_{NC_α} between the N atom and its neighboring C atom. For these coordinates, the time evolution of their averages for trajectories in either the $S_{LE}(n\pi^*)$ or the $S_{CT}(\pi\pi^*)$ state as well as the averages calculated at the ISC hopping geometries and the initial conditions are shown in Figure 5.4(c-e). As predicted by the NMA, the averages of all three internal coordinates of trajectories in the $S_{LE}(n\pi^*)$ state are very close their average values at the LE pathway hopping geometries for most of the simulation time. In contrast, the averages of these internal coordinates in the $S_{CT}(\pi\pi^*)$ state and of the CT hopping geometries show a larger difference.

In addition, Figure 5.4(f) shows the time evolution of the nitro group torsion angle of the trajectories in the $S_{LE}(n\pi^*)$ or the $S_{CT}(\pi\pi^*)$ states as well as the average values at the ISC hopping geometries and in the initial conditions. The nitro group torsion angle is described mainly by the normal mode 7 shown in Figure 5.4(a/b). As can be seen in Figure 5.4(f), unlike proposed in the experimental studies[11,13,139], ISC in 2NN does not happen at planar geometries. Rather, the geometries in the trajectories as well as at the ISC hopping points show torsional angles in the range of ca. 10-20°, which is larger than the average angle of 10.1° found in the initial conditions. The average of the torsional angle of the trajectories in the $S_{LE}(n\pi^*)$ state is again closer to the average value of the LE pathway hopping geometries than in the case of the $S_{CT}(\pi\pi^*)$ state and the CT pathway.

5.3 Effects of Different Initial Conditions

The excited-state dynamics simulations of 2NN presented in Section 5.2 employed initial conditions sampled from a Wigner distribution at $T = 300$ K (W300 ensemble). As discussed in Section 3.4, using a finite-temperature Wigner distribution includes both the ZPE and a thermal-energy contribution in the total vibrational energy. This sampling gives a more accurate description of the molecule under experimental conditions than when using either zero-temperature Wigner sampling or thermal sampling based on MD simulations, where only the ZPE or the high-temperature limit thermal energy are included in the total vibrational energy, respectively. Before the possibility of using the advanced finite-temperature Wigner sampling was realized, excited-state dynamics simulations had already been performed using initial conditions from a zero-temperature Wigner distribution (W0 ensemble) and sampled from a ground-state MD trajectory, that was propagated at the PBE0[147,239]/cc-pVDZ[247] level of theory at a temperature of $T = 300$ K (MD300 ensemble). Additionally, another set of excited-state dynamics simulations was performed using a modified version of the MD300 initial conditions (MD300+ ensemble). In these initial conditions, the same geometries as in the MD300 ensemble were used, but the atomic velocities of the molecules were scaled up so that the kinetic energy is increased to match the ZPE of the molecule. As the average frequency of 2NN of $\langle\omega\rangle = 1240\ \mathrm{cm}^{-1}$ corresponds to a temperature of $T = 868$ K in the high-temperature limit, and as the atomic velocities depend on the temperature via $3/2k_BT = 1/2mv_T^2$, the atomic velocities were scaled from $v_{T=300K}$ to $v_{T=868K}$ by a factor of $\sqrt{868/300} = 1.7$.

While the choice of the W0/MD300/MD300+ initial conditions appears inferior in light of the possibility to use the W300 ensemble, these efforts were not wasted, as the results of all calculations could be used to investigate the effects of different initial conditions on the outcome of excited-state dynamics simulations of 2NN. Motivated by this, the excited-state dynamics of 2NN have also been simulated using a fifth set of initial conditions, sampled from a Wigner distribution at $T = 500$ K (W500 ensemble). Differing only in their initial conditions, the excited-state dynamics simulations of the five ensembles were all carried out at the same level of theory as described in Section 5.2. The results of the calculations for all ensembles are presented in this section.

5.3.1 Absorption Spectra and Initially Excited States

In order to set-up the excited-state dynamics simulations, the absorption spectra of all five ensembles were calculated. The spectra are shown in Figure 5.5(a-d) alongside the density of states for each ensemble. Since the MD300 and MD300+ ensembles only differ in their momenta but contain the same geometries, their absorption spectra and density of states are identical and therefore only shown once. All five ensembles possess similar absorption spectra in the UV-VIS region with three absorption bands whose maxima lie at similar energies, i.e., between 333-337 nm, 281-291 nm, and 237-244 nm, respectively. Only the shape of the bands varies for the different ensembles. The bands become broader in the order of MD300/MD300+ < W0 < W300 < W500, i.e., with increasing vibrational energy that is available in the ensemble. With the larger vibrational energy, the individual states are smeared over larger energy ranges as is best appreciated by the densities of states shown in Figure 5.5(a-d). For example, the states S_3 and S_4, which contribute mainly to the second absorption band, also reach the excitation energy range around the lowest-energy absorption band –that is used in the dynamics simulations [gray areas in Fig-

(a-d) Absorption Spectra and Density of States for Different Initial Conditions

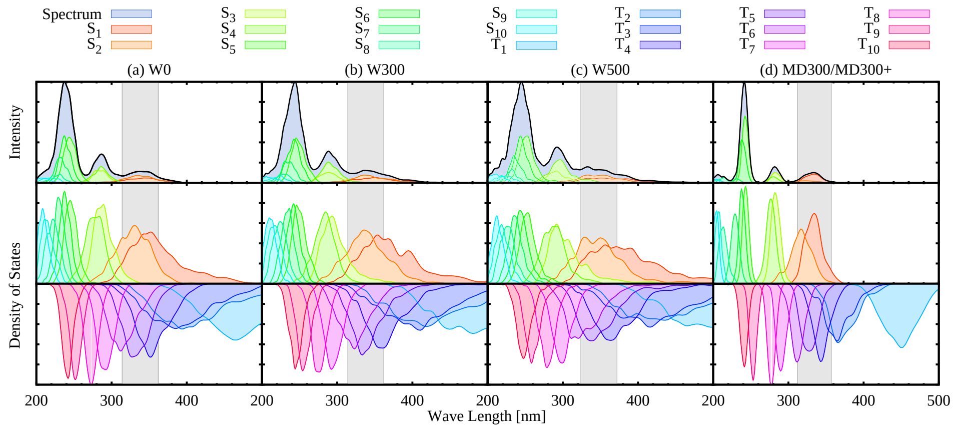

(e-i) Time Evolution of MCH Populations for Different Initial Conditions

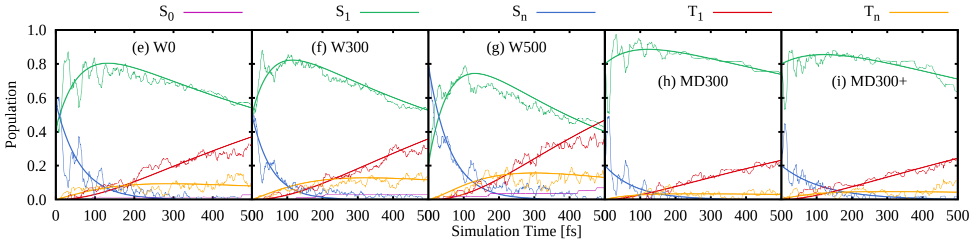

(j) Time Constants for Different Initial Conditions

Time Constant	W0	W300	W500	MD300	MD300+
τ_S [fs]	64 ± 10	56 ± 8	64 ± 13	91 ± 17	119 ± 25
τ_{ISC} [fs]	754 ± 134	710 ± 101	507 ± 88	1550 ± 448	1367 ± 346
τ_T [fs]	110 ± 14	149 ± 19	137 ± 17	78 ± 17	101 ± 27
$\tau_{S'}$ [fs]	95 ± 12	81 ± 10	90 ± 18	68 ± 11	55 ± 7
$\tau_{\mathrm{ISC'}}$ [fs]	1184 ± 230	968 ± 142	819 ± 130	2160 ± 738	1914 ± 586

(k) Properties of the DE Pathway Found in the W500 Ensemble

ISC Pathway	Electronic Transition	Natural Transition Orbitals	⟨SOC⟩
DE Pathway (Delocalized-Electronic)	$S_{CT}(\rho\pi^*) \rightarrow T_{CT}(\rho'\pi^*)$	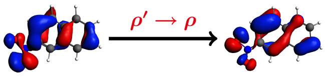	10-20 cm^{-1}

(l) Contributions of ISC Pathways for Different Initial Conditions

ISC Pathway	W0	W300	W500	MD300	MD300+
LE Pathway [%]	95	91	80	95	92
CT+DE Pathway [%]	5	9	20	5	8

Figure 5.5: (a-d) Computed absorption spectra (top panel) as well as density of states for singlet (middle panel, positive axis) and triplet (bottom panel, negative axis) states for different initial conditions. Gray areas denote the excitation-energy range used in the dynamics simulations. (e-i) Time evolution of the MCH states. (j) Time constants of the excited-state dynamics. (k) Properties of the DE pathway. ρ/ρ' are admixtures of n and π orbitals. (l) Contributions of the ISC pathways.

ure 5.5(a-d)] – in the case of the Wigner ensembles. In the stochastic selection of initially excited states in the trajectories, this lead to 20 % of all trajectories being started in either the S_3 and S_4 state in the W500 ensemble, whereas this had no effect for the W0 and W300 ensembles, where all trajectories were started in the S_1 and S_2 states. Performing a transition-density matrix analysis of the initially excited states, it is found that these S_3 and S_4 states of the W500 ensemble resemble the S_3@FC state (Figure 3.6), which, similar to the S_1@FC state, is also described by a charge-transfer $\pi\pi^*$ transition from the aromatic ring system to the nitro group.

5.3.2 Excited-State Dynamics

The time evolution of the MCH state populations of the five ensembles is shown in Figure 5.5(e-i). In general, the behavior of the excited-state dynamics of all ensembles is similar to the one of the W300 ensemble discussed in detail in Section 5.2.1. After initial dynamics in the singlet manifold ($S_n \xrightarrow{\tau_S} S_1$), population is transferred to higher-excited triplet states ($S_1 \xrightarrow{\tau_{ISC}} T_n$), before the molecule relaxs to the T_1 state ($T_n \xrightarrow{\tau_T} T_1$). As discussed previously, the dynamics in the singlet manifold are better described in terms of the reaction $S_{CT}(\pi\pi^*) \xrightarrow{\tau_{S'}} S_{LE}(n\pi^*)$, and the time constants τ_{ISC} of the singlet-to-triplet ISC and τ_T of the relaxation within the triplet manifold can be combined into an effective ISC time constant $\tau_{ISC'}$. For the five ensembles, the time constants of all processes are shown in Figure 5.5(j).

As can be seen in Figure 5.5(j), the IC dynamics within the singlet and triplet manifolds occur on a similar time scale of the order of magnitude of ca. 100 fs for all ensembles. More interestingly, however, there is a distinct difference between the ISC rates in the Wigner and MD ensembles. Both the actual (τ_{ISC}) and the effective ($\tau_{ISC'}$) ISC time constants show that ISC is approximately twice as fast in the Wigner ensembles than in the MD ensembles. Additionally, it is found that the ISC rate increases in the Wigner ensembles with higher temperatures, and ISC is faster for the MD300+ ensemble than for MD300 ensemble. Comparing all ensembles, thus it is found, that the ISC rate is larger the more vibrational energy is available. Surprisingly, the effective ISC time constants $\tau_{ISC'}$ of the MD300/MD300+ ensembles are very close to the experimentally observed time constants of $\tau_2 \approx 2$ ps (Figure 5.1). This agreement, however, is likely only coincidental. As the ISC rate increases with the vibrational energy that is available in the molecule, and the vibrational energy is not correctly accounted for in the MD ensembles, the ISC rate in the excited-state dynamics simulations of the MD ensembles has to be slower than the real one.

5.3.3 Intersystem Crossing Pathways

In Section 5.2.2, it was found that ISC for the W300 ensemble occurs via different pathways, the LE pathway [$S_{LE}(n\pi^*) \rightarrow T_{LE}(\pi'\pi^*)$] and the CT pathway [$S_{CT}(\pi\pi^*) \rightarrow T_{LE}(n\pi^*)$]. When analyzing the electronic states involved in the ISC for the W500 ensemble, a third pathway was identified. This pathway, labelled DE pathway, is depicted in Figure 5.5(k). It is characterized by the transition from a $\mathrm{S_{CT}}(\rho\pi^*)$ to a $\mathrm{T_{CT}}(\rho'\pi^*)$ state. The π^* electron NTO describing both states is again the antibonding orbital at the nitro group that also describes the other singlet and triplet states mediating the ISC [see Figure 5.3(a)]. Thus, the $\mathrm{S_{CT}}(\rho\pi^*) \rightarrow \mathrm{T_{CT}}(\rho'\pi^*)$ transition simply corresponds to the transfer of an electron from the ρ' hole NTO of the $\mathrm{T_{CT}}(\rho'\pi^*)$ state to the ρ hole NTO of the $\mathrm{S_{CT}}(\rho\pi^*)$ state. The ρ and ρ' NTOs are admixtures of different π and n orbitals [see Figure 5.5(k)] and are as such delocalized over the complete 2NN molecule. Due to this feature, the $\rho' \rightarrow \rho$ transition can be characterized as a delocalized electronic transition, and the $\mathrm{S_{CT}}(\rho\pi^*) \rightarrow \mathrm{T_{CT}}(\rho'\pi^*)$ pathway is labeled accordingly as the delocalized-electronic (DE) pathway. For the DE pathway, SOCs are of the size of 10-20 cm^{-1}, which is smaller than the SOCs of the LE pathway (40 cm^{-1}), but larger than the SOCs of the CT pathway (8 cm^{-1}). The larger SOCs of the LE pathway were assumed to be due to the smaller charge redistribution necessary for the $\pi' \rightarrow n$ transition –compared to the redistribution in the $n \rightarrow \pi$ transition of the CT pathway – as both orbitals are located at the same site of the molecule. In line with this explanation, the SOCs of the DE pathway are of intermediate size for the $\rho' \rightarrow \rho$ transition. Although both orbitals are delocalized over the complete molecule, they show an important overlap which limits the amount of charge redistribution that is necessary to connect the $\mathrm{S_{CT}}(\rho\pi^*)$ and $\mathrm{T_{CT}}(\rho'\pi^*)$ states along the DE pathway.

For all five ensembles, the relative contributions of the LE pathway as well as the CT and DE pathways are shown in Figure 5.5(l). Note that only the sum of the contributions of the CT and DE pathway is given but not their individual contributions. This is because the singlet and triplet states involved in both ISC pathways possess similar transition-density properties such as CT numbers or exciton sizes. For this reason, it has proven to be difficult to distinguish between CT and DE transitions without manually inspecting the excited states involved at every ISC hop –a very tedious endeavor given the large number of trajectories for all ensembles. Such a manual inspection was done, however, for a small sample of ISC hopping events for all ensembles, and within this small sample, only for the W500 ensemble hops following the DE pathway were found in addition to hops of the LE and CT pathways. Thus, it could only be concluded that the DE pathway contributes in the excited-state dynamics of the W500 ensemble, while it likely plays only a minor role in the dynamics of the other ensembles.

As can be seen in Figure 5.5(l), the fraction of ISC occurring via the CT+DE pathway increases among the Wigner ensembles (W0 < W300 < W500) as well as among the MD ensembles (MD300 < MD300+) with the increasing vibrational energy that is available. The same dependence on the available vibrational energy has also been observed for the ISC rate of the five ensembles [Figure 5.5(j)]. The largest contribution of the CT+DE pathway is found for the W500 ensemble for which definite sign of ISC via the DE pathway was found the excited-state dynamics. Thus, at least part of the increased ISC rate for the W500 ensemble is due to the opening of the DE pathway. In contrast, for the W0/W300 and MD300/MD300+ ensembles, the increase in the ISC rate with larger vibrational energy may simply be due to the increased momenta that allow faster transitions through the LE and CT pathways, although some contributions from the DE pathway cannot be ruled out completely.

5.4 Studies of 1NN and 2M1NN

5.4.1 Absorption Spectra and Initially Excited States

Aimed with the insights gained in the study of 2NN, the excited-state dynamics of 1NN and 2M1NN, for which ultrafast ISC was also found in experiment, were simulated. For this, first, the absorption spectra of 1NN and 2M1NN were calculated at the PBE0/DZP level of theory for Wigner ensembles at a temperature of $T = 300$ K. As in the case of 2NN, PBE0/DZP also yields a good agreement between the calculated gas-phase absorption spectra and experimental absorption spectra of 1NN and 2M1NN in n-heptane, as shown in Figure 5.6(a/b). For 1NN, the maximum of the lowest-energy absorption band at 333 nm is red-shifted by 0.13 eV compared to experiment, whereas the maximum of the second absorption band is found at 237 nm where the experimental spectrum shows a distinct shoulder on the lower-energy side of a intense UVB absorption band. For 2M1NN, the calculated maxima of the lowest-energy absorption bands lie at 369 nm and 266 nm. The experimental absorption spectrum displays a clear maximum at 268 nm close to the second calculated absorption band maximum, while there is no pronounced maximum close to the energy of the first calculated absorption band. One can, however, estimate the position of the experimental first absorption band by considering the slope of the experimental intensity distribution, which is smallest around an energy of 355 nm. Taking this energy as the position of the maximum of the experimental absorption band would result in a 0.13 eV red-shift of the calculated first absorption band.

Motivated by the good agreement between experimental and computed absorption spectra, the excited-state dynamics of 1NN and 2M1NN were simulated using the SHARC method in combination with PBE0/DZP. For both 1NN and 2M1NN, 75 trajectories were propagated. All calculations were conducted in the gas phase. The dynamics simulations were started in the bright states of both molecules in an energy range of 0.5 eV around the maxima of their calculated lowest-energy absorption bands [gray areas in Figure 5.6(a/b)]. This resulted in trajectories starting in MCH states S_1-S_3, all of which, however, correspond to the same spectroscopic states, i.e., $S_{CT}(\pi\pi^*)$ states. This is shown in Figure 5.6(a/b), which displays the average hole-electron difference populations for all initially excited states of 1NN and 2M1NN.

5.4.2 Excited-State Dynamics

The time evolution of the MCH state populations of the excited-state dynamics of 1NN and 2M1NN are shown in Figures 5.6(c) and (d), respectively. The populations of the higher-lying singlet excited states (S_n, $n = 2$-3) and higher-lying triplet excited states (T_n, $n = 2$-6) have each been combined into one

(a/b) Absorption Spectra of Nitronaphthalene Derivatives

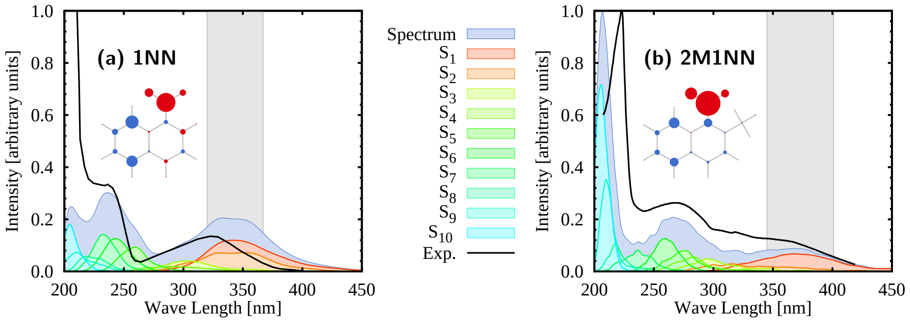

(c/d) Time Evolution of MCH Populations of Nitronaphthalene Derivatives

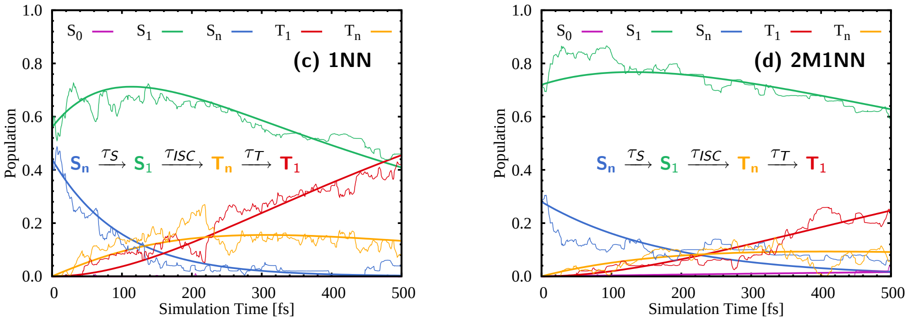

(e) Time Constants for Excited-State Dynamics of Nitronaphthalene Derivatives

Time Constants [fs]	τ_S	τ_{ISC}	τ_T	$\tau_{S'}$	$\tau_{ISC'}$
1NN	95 ± 16	562 ± 104	142 ± 20	61 ± 9	1014 ± 180
2M1NN	225 ± 81	955 ± 188	161 ± 29	–	1574 ± 320

(f) Natural Transition Orbitals in ISC Pathways of Nitronaphthalene Derivatives

Natural Transition Orbitals	1NN	2M1NN
LE Pathway $S_{LE}(n\pi^*) \rightarrow T_{LE}(\pi'\pi^*)$	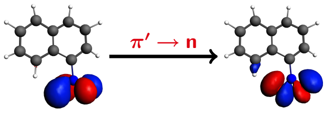	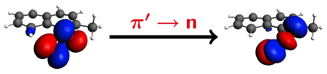
CT Pathway $S_{CT}(\pi\pi^*) \rightarrow T_{LE}(n\pi^*)$	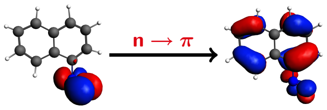	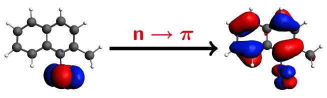

(g) Contributions, SOCs, and Nitro Group Torsion Angles of ISC Pathways

NN Derivative	C(LE)	SOC(LE)	γ(LE)	C(CT)	SOC(CT)	γ(CT)
1NN	86	40 ± 1	20 ± 1	14	22 ± 2	63 ± 5
2M1NN	41	40 ± 1	45 ± 3	59	26 ± 1	82 ± 2

Figure 5.6: (a/b) Calculated and experimental[148,248] absorption spectra of 1NN and 2M1NN. Gray areas denote excitation-energy range used in the dynamics. Molecules show the hole-electron difference populations of the initial states in the dynamics. (c/d) Time evolution of the MCH states. (e) Time constants of the excited-state dynamics. (f) Natural transition orbitals of ISC pathways in 1NN and 2M1NN. (g) Contributions C in percentage (%), SOCs in cm^{-1}, and nitro group torsion angles γ in degrees (°) of the ISC pathways.

function. This was done as, in the MCH representation, all trajectories first relax from any of the S_n states to the S_1 state where they either stay for the remainder of the simulation or undergo ISC to one of the T_n states. From the T_n states, the trajectories finally relax to the T_1 state. No ISC is found occurring directly either from the S_n states or directly to the T_1 state. Thus, the excited-state dynamics of 1NN and 2M1NN can be described similarly to the dynamics of 2NN with the simplified mechanism

$$S_n \xrightarrow{\tau_S} S_1 \xrightarrow{\tau_{ISC}} T_n \xrightarrow{\tau_T} T_1. \tag{5.3}$$

For this mechanism, fits for the MCH state populations are shown in Figure 5.6(c/d), and time constants obtained by a fit of 100 bootstrap copies[244] are reported in Figure 5.6(e). For each of the three processes in the mechanism, the time constants are of similar size for 1NN and 2M1NN as well as compared to the time constants of 2NN [Figure 5.2(b)]. For the dynamics in the singlet manifold τ_S is larger for both 1NN (98 ± 16 fs) and 2M1NN (225 ± 81 fs) than for 2NN (56 ± 8 fs). For the singlet-to-triplet ISC, τ_{ISC} of 2NN (710 ± 101 fs) lies in between the values of 1NN (562 ± 104 fs) and 2M1NN (955 ± 188 fs), whereas for the final relaxation within the triplet manifold, the time constants τ_T for all three NN derivatives are nearly the same (140-160 fs).

Following the discussion of 2NN, the slow ISC time constant τ_{ISC} and the fast time constant τ_T describing IC in the triplet manifold can be combined into an effective ISC time constant $\tau_{ISC'}$ according to eq. (5.2). These effective ISC times are 1014 ± 180 fs and 1574 ± 320 fs for 1NN and 2M1NN, respectively (2NN: $\tau_{ISC'} = 968 \pm 142$ fs). For 2NN, it was additionally shown that the initial dynamics in the singlet manifold before ISC were better described by the process $\mathrm{S}_{\mathrm{CT}}(\pi\pi^*) \xrightarrow{\tau_{S'}} \mathrm{S}_{\mathrm{LE}}(n\pi^*)$ than by MCH state process $\mathrm{S}_2 \xrightarrow{\tau_S} \mathrm{S}_1$. In the analysis of 2NN, the MCH state populations were attributed to either the $\mathrm{S}_{\mathrm{CT}}(\pi\pi^*)$ or the $\mathrm{S}_{\mathrm{LE}}(n\pi^*)$ state based on their dipole moment. For this assignment, the threshold $\mu = 8$ D was used, which lies between the dipole moments of both states at their respective minimum-energy geometries, i.e., $\mu[\mathrm{S}_{\mathrm{CT}}(\pi\pi^*)] = 12.9$ D and $\mu[\mathrm{S}_{\mathrm{LE}}(n\pi^*)] = 3.7$ D. For 1NN and 2M1NN, the corresponding analysis is more complicated. Also for these molecules, initially only a $\mathrm{S}_{\mathrm{CT}}(\pi\pi^*)$ state is populated, while ISC occurs from both a $\mathrm{S}_{\mathrm{CT}}(\pi\pi^*)$ and a $\mathrm{S}_{\mathrm{LE}}(n\pi^*)$ state, which requires that parts of the singlet populations must be transferred according to $\mathrm{S}_{\mathrm{CT}}(\pi\pi^*) \rightarrow \mathrm{S}_{\mathrm{LE}}(n\pi^*)$. However, distinguishing between both types of states based on their dipole moments is less straightforward due to the smaller difference between the dipole moments of both states. For the $\mathrm{S}_{\mathrm{LE}}(n\pi^*)$, the dipole moment at the minimum-energy geometry is ca. 3.3 D for both 1NN and 2M1NN, i.e., similar to that of the $\mathrm{S}_{\mathrm{LE}}(n\pi^*)$ state of 2NN. However, for the $\mathrm{S}_{\mathrm{CT}}(\pi\pi^*)$ state, the dipole moment is only ca. 8.8 D, i.e., much smaller than that of the $\mathrm{S}_{\mathrm{CT}}(\pi\pi^*)$ state in 2NN (12.9 D). The smaller dipole moment of the $\mathrm{S}_{\mathrm{CT}}(\pi\pi^*)$ state in 1NN and 2M1NN can be explained attending to their molecular structures. In these molecules, the nitro group is closer to the center of the aromatic ring system than in the case of 2NN, leading to a smaller dipole moment for the $\mathrm{S}_{\mathrm{CT}}(\pi\pi^*)$. The smaller difference between the dipole moments of $\mathrm{S}_{\mathrm{CT}}(\pi\pi^*)$-type and $\mathrm{S}_{\mathrm{LE}}(n\pi^*)$-type states makes distinguishing them along the dynamics more complicated. Distinguishing between the $\mathrm{S_{CT}}(\pi\pi^*)$ and $\mathrm{S_{LE}}(n\pi^*)$ states by a threshold of $\mu = 6$ D yielded a time constant $\tau_{S'} = 61 \pm 9$ fs for 1NN, however, for 2M1NN no meaningful fit function could be obtained that agreed reasonably with the time evolution of the excited-state populations of the dynamics –neither using this threshold nor any other similar value.

The time constants for the excited-state dynamics of 1NN and 2M1NN obtained from transient-absorption experiments in MeCN and cyclohexane[11,13] are shown in Figure 5.1. For 1NN, the two fastest time constants are $\tau_1 = 110 \pm 50$ fs and $\tau_2 = 2.3 \pm 0.2$ ps in the nonpolar solvent cyclohexane, and these values are slightly larger in acetonitrile. These time constants are of the same magnitude as $\tau_{S'} = 61 \pm 9$ fs and $\tau_{ISC'} = 1.0 \pm 0.2$ ps obtained in the calculations, thus, supporting the mechanism proposed in this work. For 2M1NN, a somewhat different situation is encountered. For τ_1 values of 370 ± 70 and 210 ± 50 fs were obtained from the experiments in cyclohexane and MeCN, respectively. Although no value for $\tau_{S'}$ could be obtained from the dynamics simulations to compare directly to τ_1, instead it can be noticed that $\tau_S = 225 \pm 81$ fs is very similar to τ_1. As this τ_S is also 2-4 times larger than the time constants τ_S of 2NN and 1NN, the larger value of $\tau_S = 225 \pm 81$ fs can be interpreted as a sign for slower dynamics in the singlet manifold in 2M1NN –not only in terms of MCH states, but also in terms of the different spectroscopic singlet states. For τ_2, experimental values of 0.6 ± 0.1 and 1.4 ± 0.3 ps were obtained in cyclohexane and MeCN, respectively. The difference between these two time constants is larger than compared to any other pair of time constants of 1NN, 2NN, and 2M1NN for the different solvents cyclohexane and acetonitrile, indicating some kind of solvent effect. Interestingly, the value of $\tau_2 = 1.4 \pm 0.3$ ps obtained in the nonpolar solvent cyclohexane agrees very well with the value of $\tau_{ISC'} = 1.6 \pm 0.3$ ps obtained from the gas-phase calculations. Following the previous arguments in the discussion of the results of 2NN and 1NN, however, this agreement must be seen as a fortuitous coincidence. For both, 2NN and 1NN, $\tau_{ISC'}$ underestimated τ_2 by a factor of 2, and consequently, the same behavior should be expected for 2M1NN. Furthermore, among the three NN derivatives, the computed $\tau_{ISC'}$ is the largest for 2M1NN, while the experimental τ_2 is the smallest for 2M1NN. Therefore, it is better to conclude that $\tau_{ISC'}$ of 2M1NN is also of the same order of magnitude as τ_2 rather than highlighting their close agreement. The third experimentally obtained time constants $\tau_3 = 6 - 11$ ps are too large to be reproduced in the 500 fs simulations of this work, and, thus, are again left out of the discussion.

5.4.3 Intersystem Crossing Pathways

Having established the general mechanism of the excited-state dynamics of 1NN and 2M1NN, the electronic structure of the singlet and triplet states at the ISC hopping geometries was analyzed in more detail. As for 2NN at $T = 300$ K, ISC is found to occur via the LE and CT pathways, whereas there was no evidence of the DE pathway which was direclty observed only for the $T = 500$ K ensemble of 2NN. For both, 1NN and 2M1NN, the NTOs describing the ISC transitions of both pathways are depicted in Figure 5.6(f). Furthermore, in

Figure 5.6(g), the contributions, average SOCs, and average nitro group torsion angles γ at the ISC hopping geometries of both pathways are shown. The NTOs in Figure 5.6(f) are taken from specific ISC hopping events, however, their geometries are representative for the geometries at the LE and CT pathways. For 1NN, ISC via the LE pathway [$\mathrm{S_{LE}}(n\pi^*) \rightarrow \mathrm{T_{LE}}(\pi'\pi^*)$] occurs at geometries with a nitro group torsion angle $\gamma = 20 \pm 1°$ that is slighty smaller than the average angle in the initial conditions of 1NN ($\gamma = 32°$). In contrast, ISC via the CT pathway [$\mathrm{S_{CT}}(\pi\pi^*) \rightarrow \mathrm{T_{LE}}(n\pi^*)$] occurs at geometries where the nitro group is displaced further out-of-plane with an average torsional angle of $\gamma = 63 \pm 5°$. For 2M1NN, the ISC transitions via the LE pathway occur at geometries with a torsional angle of $\gamma = 45 \pm 3°$, which is similar to the average angle in the initial conditions ($\gamma = 48°$), while ISC transitions via the CT pathway occur at geometries where the nitro group is almost perpendicular to the aromatic ring ($\gamma = 82 \pm 2°$).

The ISC contributions of both pathways for 1NN [Figure 5.6(g)] are similar to those in 2NN [Figure 5.3], as the majority of ISC occurs via the LE pathway (86 %), and only a small fraction of ISC occurs via the CT pathway (14 %). Furthermore, also the SOCs of the LE pathway are of similar size as in 2NN (40 cm^{-1}). The average SOCs of the CT pathway in 1NN, however, are much larger (22 cm^{-1}) than in 2NN (8 cm^{-1}). One may wonder whether the nitro group torsion is responsible for the larger SOCs in the CT pathway of 1NN, i.e., if by rotating the nitro group further out-of-plane, the interaction between the n orbital of the $\mathrm{T_{LE}}(n\pi^*)$ state at the nitro group and the π orbital of the $\mathrm{S_{CT}}(\pi\pi^*)$ state in the aromatic ring becomes more favorable. In consonance with this explanation, the SOCs increase even slightly further for the CT pathway of 2M1NN (26 cm^{-1}), where the $\mathrm{S_{CT}}(\pi\pi^*) \rightarrow \mathrm{T_{LE}}(n\pi^*)$ transition occurs at geometries in which the nitro group is almost perpendicular to the aromatic ring. Strangely, such a behavior may also be seen to go against El-Sayed's rules (see Section 2.3.6). By rotating the nitro group perpendicular to the aromatic ring, the n orbital at the nitro group assumes the same symmetry properties as the π orbitals in the aromatic ring, which should lead to smaller –not larger –SOCs. Clearly, this is an interesting observation that still lacks a satisfying explanation. Note that for the LE pathway, the nitro group torsion does not affect the size of the SOCs, since both the π' orbital of the $\mathrm{T_{LE}}(\pi'\pi^*)$ state as well as the n orbital of the $\mathrm{S_{LE}}(n\pi^*)$ state are localized at the nitro group, and, thus, the nitro group torsion does not change their relative positions.

Figure 5.6(g) also shows the ISC contributions for 2M1NN. In contrast to 2NN and 1NN, for 2M1NN, the majority of ISC occurs via the CT pathway (59 %), despite the corresponding SOCs being smaller than for the LE pathway. Given that out of the three NN derivatives, $\tau_{ISC/ISC'}$ is the largest for 2M1NN, the larger fraction of ISC occuring via the CT pathway can be attributed to a decreased efficiency of the LE pathway, rather than the CT pathway becoming more efficient in 2M1NN. As the SOCs of the LE pathway are the same size for 2M1NN and 2NN/1NN, the decreased efficiency of the LE pathway in 2M1NN suggests that the corresponding LE hopping geometries may not be as easily reached in 2M1NN as in the other NN derivatives.

5.5 Conclusions from the Dynamics Simulations

The excited-state dynamics of 2NN, 1NN, and 2M1NN have been simulated. All three NN derivatives displayed a similar relaxation mechanism: after excitation to the lowest-energy bright $S_{CT}(\pi\pi^*)$ state, the molecules initially undergo IC on a 100 fs time scale to a $S_{LE}(n\pi^*)$ state. The molecules then transfer via ISC to the triplet manifold on a 1 ps time scale, before they relax via IC to the lowest-lying triplet state on a IC-typical time scale of 100 fs. For all molecules, two ISC pathways were found to be operative at room and lower temperatures. In 2NN and 1NN, the vast majority of ISC events occured via $S_{LE}(n\pi^*) \rightarrow T_{LE}(\pi'\pi^*)$ transitions. A minor fraction of ISC occured from the initially excited $S_{CT}(\pi\pi^*)$ state to a $T_{LE}(n\pi^*)$ state. For 2M1NN, in contrast, the contributions of both ISC pathways are more balanced, with the $S_{CT}(\pi\pi^*) \rightarrow T_{LE}(n\pi^*)$ pathway being favored slightly.

Previous experimental studies also found two processes in the beginning of the excited-state dynamics of the NN derivatives and attributed these processes to singlet-to-triplet ISC (100 fs) and IC within the triplet manifold (1 ps). This assignment was likely based on the erroneous assumption that after excitation to the $S_{CT}(\pi\pi^*)$ state –which is also the S_1 state at the FC geometry –the molecules could not undergo further relaxation dynamics in the singlet manifold, and had to relax directly to the triplet states. In line with this view, ISC was considered only to occur via the $S_{CT}(\pi\pi^*) \rightarrow T_{LE}(n\pi^*)$ pathway. In view of the present results, the, at best, incomplete picture of the dynamics derived from the experimental results should be substituted by the mechanism proposed in this thesis which includes the initial singlet dynamics and multiple ISC pathways.

For 2NN, different initial conditions were tested and their effects on the excited-state dynamics were investigated. Thereby, it was found that the ISC rate increases when more vibrational energy is available in the initial conditions. The ISC rates were larger when the dynamics were started from Wigner ensembles than when they were started from MD ensembles, and the ISC rate increased further when the Wigner ensembles were sampled at higher temperatures. Furthermore, at $T = 500$ K, a third ISC pathway described by a $S_{CT}(\rho\pi^*) \rightarrow T_{CT}(\rho'\pi^*)$ transition was found to become operative.

Of the different ISC pathways, the $S_{LE}(n\pi^*) \rightarrow T_{LE}(\pi'\pi^*)$ channel possesses the largest SOCs of ca. 40 cm^{-1} found for all three NN derivatives. The large size of these SOCs was suggested to be due to the similar electronic charge distribution of the $S_{LE}(n\pi^*)$ and $T_{LE}(\pi'\pi^*)$ states. Comparing the NTOs of these states, their transition could be described by a simple one electron transfer from a π' orbital to an n orbital. Both, π' and n orbitals are antisymmetrical combinations of p orbitals located at the oxygen atoms of the nitro group, so that the $\pi' \rightarrow n$ transfer just corresponds to changing the angular momentum of one electron. Since this electronic transition takes place entirely in the nitro group, it is likely a general route of ISC in nitro compounds and it can be key to the ultrafast ISC observed in many NPAHs. Following this assumption, the photodynamics of NPAHs can be controlled by the population of the $S_{LE}(n\pi^*)$ state, from which ISC can proceed effortlessly. Clearly, it will be interesting to see if this model applies also in the study of further NPAH derivatives.

6 Summary

The experimental study of ultrafast electronic relaxation dynamics in the past few decades has revealed a number of classes of organic molecules exhibiting ultrafast ISC. To study the intriguing phenomenon of ultrafast ISC in organic molecules, this work set out to investigate the excited-state dynamics of molecules of one of the classes, i.e., nitro aromatic compounds. For this, non-adiabatic dynamics simulations were performed using the SHARC method for three nitronaphthalene derivatives. Indeed, ISC was found to be ultrafast in the simulations, however, not on a $\sim$ 100 fs time scale as previously proposed in experimental studies, but rather on the time scale of 1 ps. Instead, it could be demonstrated that the 100 fs fast dynamics correspond to IC dynamics within the singlet manifold. The dynamics simulations revealed that ISC in the nitronaphthalene derivatives proceeds mainly via two pathways. By starting the simulations with different initial conditions, it was shown that the contributions of the different ISC pathways to the total ISC rate are temperature dependent. The electronic transition of the ISC channel, that is the sole main pathway in 1NN and 2NN and an important one in 2M1NN, can be described by a $\pi \rightarrow n$ transition which is a charge redistribution localized completely at the nitro group. Due to the localization of this transition, the corresponding ISC channel may be a common feature found also in the excited-state dynamics of other nitro aromatic compounds and may explain the ultrafast character of the ISC observed in these compounds. In contrast, the electronic transition in the other channel is described by a $n \rightarrow \pi$ transition involving a charge redistribution from the nitro group to the aromatic ring system. If present also in other nitro aromatic compounds, the efficiency of this transition will depend more intimately on the aromatic ring system of the individual compounds.

The path of studying excited states of nitro aromatic compounds did pose quite a few challenges that had to be surmounted, bearing, however, the reward of learning valuable lessons at the end. Thus, in addition to the study of the excited-state dynamics of the nitronaphthalene derivatives, a second part of this thesis dealt with vibrational sampling and its effect on the character of electronically excited states. It was shown in the study of the absorption spectra of nitrobenzene in gas phase and water that neglecting the effects of vibrational motion yielded erroneous conclusions on the electronic character of lowest-energy absorption bands. The pronounced CT character that was found for the bright states at the FC geometry was quenched to a large extent in the bright states in the vibrational ensembles, totally changing the characterization of these states. Furthermore, the influence of vibrational sampling in the simulation of the absorption spectrum of 2NN in methanol was investigated, and the performance of different common vibrational sampling approaches, i.e., zero-temperature Wigner sampling and thermal sampling from MD trajectories, was evaluated. One main difference between both approaches is the vibrational energy that is available in the sampling, i.e., the ZPE in Wigner sampling and the high-temperature limit thermal-energy contribution in MD sampling. Neither approach really accounts for the correct total energy, that is in fact the sum of ZPE and the genuine thermal-energy contribution. This thermal-energy contribution, however, can easily be accounted for in Wigner sampling by extending the Wigner sampling to the finite-temperature formalism through considering the population of vibrationally excited states.

The third part of this thesis comprised the evaluation of the performance of the CASPT2 method in the description of excited states, and the effect that the IPEA shift can have on the energy of these states. The IPEA shift was originally introduced to CASPT2 to correct for errors found in calculations of dissociation energies. The errors were attributed to originate from a general underestimation of open-shell electronic states and were supposed to be present also in the calculation of excited states. This claim, however, could be rebuked by a large literature survey, FCI/CASPT2 benchmark calculations on di-/triatomic molecules, and extended CASPT2 benchmark calculations on the organic molecules of the Thiel set. While it was indeed found that CASPT2 underestimated the excitation energies of the di-/triatomic molecules as well as the organic molecules of the Thiel set with respect to their FCI results and to experimental reference data, respectively, this underestimation is smaller than that expected from the calculation of the dissociation energies. Inclusion of the IPEA shift leads to larger excitation energies with the size of the energy shift depending on the size of the system, which, for the organic molecules of the Thiel set, resulted in a considerable overestimation of the excitation energy. Furthermore, both the error of CASPT2 and the size of the energy correction of the IPEA shift were found to depend on the basis set employed in calculation, thus, calling for a different ideal IPEA shift value for each individual calculation. Clearly, this is an unconvenient result for the performance of a highly trusted ab initio method. To alleviate this problem at least for small and medium-sized organic molecules, the extended CASPT2 benchmark calculations in this thesis pragamtically suggest the usage of basis sets of double zeta quality while setting the IPEA shift to zero to profit from error cancellation.

In conclusion, the excited-state dynamics simulations for the nitronaphthalene derivatives provided a detailed picture of the mechanism of ultrafast ISC in these compounds. Clearly, it will be interesting to find out how well the insights gained in these simulations apply to the excited-state dynamics of further nitro aromatic compounds in future work, an effort that will greatly benefit from the understandings on vibrational sampling and the performance of CASPT2 established in this thesis.

Bibliography

[1] J. A. Warren and E. R. Bernstein. The $S_2 \leftarrow S_0$ laser photoexcitation spectrum and excited state dynamics of jet-cooled acetophenone. *J. Chem. Phys.*, 85:2365–2367, 1986.

[2] R. Morales-Cueto, M. Esquivelzeta-Rabell, J. Saucedo-Zugazagoitia, and J. Peon. Singlet excited-state dynamics of nitropolycyclic aromatic hydrocarbons: Direct measurements by femtosecond fluorescence up-conversion. *J. Phys. Chem. A*, 111:552–557, 2007.

[3] C. E. Crespo-Hernández, G. Burdzinski, and R. Arce. Environmental photochemistry of nitro-PAHs: Direct observation of ultrafast intersystem crossing in 1-nitropyrene. *J. Phys. Chem. A*, 112:6313–6319, 2008.

[4] J. S. Zugazagoitia, C. X. Almora-Díaz, and J. Peon. Ultrafast intersystem crossing in 1-nitronaphthalene. An experimental and computational study. *J. Phys. Chem. A*, 112:358–365, 2008.

[5] O. F. Mohammed and E. Vauthey. Excited-state dynamics of nitroperylene in solution: Solvent and excitation wavelength dependence. *J. Phys. Chem. A*, 112:3823–3830, 2008.

[6] J. S. Zugazagoitia, E. Collado-Fregoso, E. F. Plaza-Medina, and J. Peon. Relaxation in the triplet manifold of 1-nitronaphthalene observed by transient absorption spectroscopy. *J. Phys. Chem. A*, 113:805–810, 2009.

[7] C. Reichardt, R. A. Vogt, and C. E. Crespo-Hernández. On the origin of ultrafast nonradiative transitions in the nitro-polycyclic aromatic hydrocarbons: Excited-state dynamics in 1-nitronaphthalene. *J. Chem. Phys.*, 131:224518, 2009.

[8] E. Collado-Fregoso, J. S. Zugazagoitia, E. F. Plaza-Medina, and J. Peon. Excited-state dynamics of nitrated push-pull molecules: The importance of the relative energy of the singlet and triplet manifold. *J. Phys. Chem. A*, 113:13498–13508, 2009.

[9] E. F. Plaza-Medina, W. Rodríguez-Córdoba, and J. Peon. Role of upper triplet states on the photophysics of nitrated polyaromatic compounds: S_1 lifetimes of singly nitrated pyrenes. *J. Phys. Chem. A*, 115:9782–9789, 2011.

[10] S. Murudkar, A. K. Mora, P. K. Singh, and S. Nath. Origin of ultrafast excited state dynamics of 1-nitropyrene. *J. Phys. Chem. A*, 115:10762–10766, 2011.

[11] R. A. Vogt, C. Reichardt, and C. E. Crespo-Hernández. Excited-state dynamics in nitro-naphthalene derivatives: Intersystem crossing to the triplet manifold in hundreds of femtoseconds. *J. Phys. Chem. A*, 117:6580–6588, 2013.

[12] R. López-Arteaga, A. B. Stephansen, C. A. Guarin, T. I. Sølling, and J. Peon. The influence of push-pull states on the ultrafast intersystem crossing in nitroaromatics. *J. Phys. Chem. B*, 117:9947–9955, 2013.

[13] R. A. Vogt and C. E. Crespo-Hernández. Conformational control in the population of the triplet state and photoreactivity of nitronaphthalene derivatives. *J. Phys. Chem. A*, 117:14100–14108, 2013.

[14] R. W. Yip, D. K. Sharma, R. Giasson, and D. Gravel. Picosecond excited-state absorption of alkyl nitrobenzenes in solution. *J. Phys. Chem.*, 88:5770–5772, 1984.

[15] M. Takezaki, N. Hirota, and M. Terazima. Nonradiative relaxation processes and electronic excited states of nitrobenzene studied by picosecond time-resolved transient grating method. *J. Phys. Chem. A*, 101:3443–3448, 1997.

[16] M. Takezaki, N. Hirota, M. Terazima, H. Sato, T. Nakajima, and S. Kato. Geometries and energies of nitrobenzene studied by CAS-SCF calculations. *J. Phys. Chem. A*, 101:5190–5195, 1997.

[17] M. Takezaki, N. Hirota, and M. Terazima. Relaxation of nitrobenzene from the excited singlet state. *J. Chem. Phys.*, 108:4685–4686, 1998.

[18] C. L. Thomsen, J. Thøgersen, and S. R. Keiding. Ultrafast charge-transfer dynamics: Studies of *p*-nitroaniline in water and dioxane. *J. Phys. Chem. A*, 102:1062–1067, 1998.

[19] S. A. Kovalenko, R. Schanz, V. M. Farztdinov, H. Henning, and N. P. Ernsting. Femtosecond relaxation of photoexcited *para*-nitroaniline: Solvation, charge transfer, internal conversion and cooling. *Chem. Phys. Lett.*, 323:312–322, 2000.

[20] V. M. Farztdinov, R. Schanz, S. A. Kovalenko, and N. P. Ernsting. Relaxation of optically excited *p*-nitroaniline: Semiempirical quantum-chemical calculations compared to femtosecond experimental results. *J. Phys. Chem. A*, 104:11486–11496, 2000.

[21] B. Heinz, T. Schmierer, S. Laimgruber, and P. Gilch. Excited state processes of nitrobenzaldehydes probed by ultrafast fluorescence and absorption spectroscopy. *J. Photochem. Photobiol. A*, 199:274–281, 2008.

[22] S. Laimgruber, T. Schmierer, P. Gilch, K. Kiewisch, and J. Neugebauer. The ketene intermediate in the photochemistry of *ortho*-nitrobenzaldehyde. *Phys. Chem. Chem. Phys.*, 10:3872–3882, 2008.

[23] S. Cheng, P. Song, S. Yang, H. Yin, and K. Han. Fluorescence and solvent-dependent phosphorescence studies of *o*-nitrobenzaldehyde: A combined experimental and theoretical investigation. *Phys. Chem. Chem. Phys.*, 12:9067–9074, 2010.

[24] S. Rafiq, R. Yadav, and P. Sen. Femtosecond excited-state dynamics of 4-nitrophenyl pyrrolidinemethanol: Evidence of twisted intramolecular charge transfer and intersystem crossing involving the nitro group. *J. Phys. Chem. A*, 115:8335–8343, 2011.

[25] R. Ghosh and D. K. Palit. Ultrafast dynamics of the excited states of 1-(*p*-nitrophenyl)-2-(hydroxymethyl)pyrrolidine. *J. Phys. Chem. A*, 116:1993–2005, 2012.

[26] T. Schmierer, G. Ryseck, T. Villnow, N. Regner, and P. Gilch. Kasha or state selective behavior in the photochemistry of *ortho*-nitrobenzaldehyde? *Photochem. Photobiol. Sci.*, 11:1313–1321, 2012.

[27] H. A. Ernst, T. J. A. Wolf, O. Schalk, N. González-García, A. E. Boguslavskiy, A. Stolow, M. Olzmann, and A.-N. Unterreiner. Ultrafast dynamics of *o*-nitrophenol: An experimental and theoretical study. *J. Phys. Chem. A*, 119:9225–9235, 2015.

[28] S. Aloïse, C. Ruckebusch, L. Blanchet, J. Réhault, G. Buntinx, and J.-P. Huvenne. The benzophenone $S_1(n,\pi^*) \rightarrow T_1(n,\pi^*)$ states intersystem crossing reinvestigated by ultrafast absorption spectroscopy and multivariate curve resolution. *J. Phys. Chem. A*, 112:224–231, 2008.

[29] N. Tamai, T. Asahi, and H. Masuhara. Intersystem crossing of benzophenone by femtosecond transient grating spectroscopy. *Chem. Phys. Lett.*, 198:413–418, 1992.

[30] B. C. Shah, M. A. J. Rodgers, and D. C. Neckers. The $S_2 \rightarrow S_1$ internal conversion of benzophenone and *p*-iodobenzophenone. *J. Phys. Chem. A*, 108:6087–6089, 2004.

[31] Q. Li, A. Migani, and L. Blancafort. Irreversible phototautomerization of *o*-phthalaldehyde through electronic relocation. *Phys. Chem. Chem. Phys.*, 14:6561–6568, 2012.

[32] M.-D. Li, W. Li, J. Ma, T. Su, M. Liu, Y. Du, and D. L. Phillips. Femtosecond transient absorption, nanosecond time-resolved resonance Raman, and density functional theory study of fenofibric acid in acetonitrile and isopropyl alcohol solvents. *J. Phys. Chem. A*, 115:14168–14174, 2011.

[33] J. J. Cavaleri, K. Prater, and R. M. Bowman. An investigation of the solvent dependence on the ultrafast intersystem crossing kinetics of xanthone. *Chem. Phys. Lett.*, 259:495–502, 1996.

[34] Y. Ohshima, T. Fujii, T. Fujita, D. Inaba, and M. Baba. $S_1\ ^1A_2(n\pi^*)$ and $S_2\ ^1A_1(\pi\pi^*)$ states of jet-cooled xanthone. *J. Phys. Chem. A*, 107:8851–8855, 2003.

[35] H. Satzger, B. Schmidt, C. Root, W. Zinth, B. Fierz, F. Krieger, T. Kiefhaber, and P. Gilch. Ultrafast quenching of the xanthone triplet by energy transfer: New insight into the intersystem crossing kinetics. *J. Phys. Chem. A*, 108:10072–10079, 2004.

[36] T. J. A. Wolf, D. Voll, C. Barner-Kowollik, and A.-N. Unterreiner. Elucidating the early steps in photoinitiated radical polymerization via femtosecond pump-probe experiments and DFT calculations. *Macromolecules*, 45:2257–2266, 2012.

[37] C. Ma, Y. Du, W. M. Kwok, and D. L. Phillips. Femtosecond transient absorption and nanosecond time-resolved resonance Raman study of the solvet-dependent photo-deprotection reaction of benzoin diethyl phosphate. *Chem. Eur. J.*, 13:2290–2305, 2007.

[38] H. J. van Ramesdonk, B. H. Bakker, M. M. Groeneveld, J. W. Verhoeven, B. D. Allen, J. P. Rostron, and A. Harriman. Ultrafast intersystem crossing in 9,10-anthraquinones and intramolecular charge separation in an anthraquinone-based dyad. *J. Phys. Chem. A*, 110:13145–13150, 2006.

[39] C. Yang, H. Su, X. Sun, and M. W. George. Ultrafast formation of the benzoic acid triplet upon ultraviolet photolysis and its sequential photodissociation in solution. *J. Chem. Phys.*, 136:204507, 2012.

[40] O. Schalk, P. Lang, M. S. Schuurman, G. Wu, M. Bradler, E. Riedle, and A. Stolow. Internal conversion vs. intersystem crossing – what drives the dynamics of cyclic α,β-enones? *EPJ Web of Conferences*, 41:05029, 2013.

[41] Y. Wang, Z. Liu, Y. Xu, and B. Zhang. The geometrical change and intramolecular energy transfer upon $S_1 \leftarrow S_0$ excitation in cyclopentanone. *J. Chem. Phys,*, 143:064304, 2015.

[42] J. Cao and Z.-Z. Xie. Internal conversion and intersystem crossing in α, β-enones: a combination of electronic structure calculations and dynamics simulations. *Phys. Chem. Chem. Phys.*, 18:6931–6945, 2016.

[43] R. Mundt, T. Villnow, C. T. Ziegenbein, P. Gilch, C. M. Marian, and V. Rai-Constapel. Thioxanthone in apolar solvents: ultrafast internal conversion precedes fast intersystem crossing. *Phys. Chem. Chem. Phys.*, 18:6637–6647, 2016.

[44] H. Yin, H. Li, G. Xia, C. Ruan, Y. Shi, H. Wang, M. Jin, and D. Ding. A novel non-fluorescent excited state intromolecular proton transfer phenomenon induced by intramolecular hydrogen bonds: an experimental and theoretical investigation. *Scientific Reports*, 6:19774, 2016.

[45] A. Bhattacherjee, C. D. Pemmaraju, K. Schnorr, A. R. Attar, and S. R Leone. Ultrafast intersystem crossing in acetylacetone via femtosecond X-ray transient absorption at the carbon K-edge. *J. Am. Chem. Soc.*, 139:16576–16583, 2017.

[46] S. K. Rajagopal, A. R. Mallia, and M. Hariharan. Enhanced intersystem crossing in carbonylpyrenes. *Phys. Chem. Chem. Phys.*, 19:28225–28231, 2017.

[47] A. B. Stephansen and T. I. Sølling. Distortion dependent intersystem crossing: A femtosecond time-resolved photoelectron spectroscopy study of benzene, toluene, and p-xylene. *Struct. Dyn.*, 4:044008, 2017.

[48] Y. Liu, G. Knopp, P. Hemberger, Y. Sych, P. Radi, A. Bodi, and T. Gerber. Ultrafast imaging of electronic relaxation in *o*-xylene: a new competing intersystem crossing channel. *Phys. Chem. Chem. Phys.*, 15:18101–18107, 2013.

[49] D. S. N. Parker, R. S. Minns, T. J. Penfold, G. A. Worth, and H. H. Fielding. Ultrafast dynamics of the S_1 excited state of benzene. *Chem. Phys. Lett.*, 469:43–47, 2009.

[50] R. S. Minns, D. S. N. Parker, T. J. Penfold, G. A. Worth, and H. H. Fielding. Competing ultrafast intersystem crossing and internal conversion in the ”channel 3” region of of benzene. *Phys. Chem. Chem. Phys.*, 12:15607–15615, 2010.

[51] T. J. Penfold, R. Spesyvtsev, O. M. Kirkby, R. S. Minns, D. S. N. Parker, H. H. Fielding, and G. A. Worth. Quantum dynamics stury of the competing ultrafast intersystem crossing and internal conversion in the ”channel 3” region of benzene. *J. Chem. Phys.*, 137:204310, 2012.

[52] Y. Harada, C. Okabe, T. Kobayashi, T. Suzuki, T. Ichimura, N. Nishi, and Y.-Z. Xu. Ultrafast intersystem crossing of 4-thiothymidine in aqueous solution. *J. Phys. Chem. Lett.*, 1:480–484, 2010.

[53] C. Reichardt and C. E. Crespo-Hernández. Ultrafast spin-crossover in 4-thiothymidine in an ionic liquid. *Chem. Commun.*, 46:5963–5965, 2010.

[54] C. Reichardt and C. E. Crespo-Hernández. Room-temperature phosphorescence of the DNA monomer analogue 4-thiothymidine in aqueous solution after UVA excitation. *J. Phys. Chem. Lett.*, 1:2239–2243, 2010.

[55] C. Reichardt, C. Guo, and C. E. Crespo-Hernández. Excited-state dynamics in 6-thioguanosine from the femtosecond to microsecond time scale. *J. Phys. Chem. B*, 115:3263–3270, 2011.

[56] M. Pollum and C. E. Crespo-Hernández. Communication: The dark singlet state as a doorway state in the ultrafast and efficient intersystem crossing dynamics in 2-thiothymine and 2-thiouracil. *J. Chem. Phys.*, 140:071101, 2014.

[57] M. Pollum, S. Jokusch, and C. E. Crespo-Hernández. 2,4-dithiothymine as a potent UVA chemotherapeutic agent. *J. Am. Chem. Soc.*, 136:17930–17933, 2014.

[58] B. Ashwood, S. Jockusch, and C. E. Crespo-Hernández. Excited-state dynamics of the thiopurine prodrug 6-thioguanine: Can N9-glycolsylation affect its phototoxic activity? *Molecules*, 22:379, 2017.

[59] L. Martínez-Fernández, L. González, and I. Corral. An *ab initio* mechanism for efficient population of triplet states in cytotoxic sulfur substituted DNA bases: the case of 6-thioguanine. *Chem. Commun.*, 48:2134–2136, 2012.

[60] G. Cui and W.-H. Fang. State-specific heavy-atom effect on intersystem crossing processes in 2-thiothymine: A potential photodynamic therapy photosensitizer. *J. Chem. Phys.*, 138:044315, 2013.

[61] L. Martínez-Fernández, I. Corral, G. Grannuci, and M. Persico. Competing ultrafast intersystem crossing and internal conversion: A time resolved picture for the deactivation of 6-thioguanine. *Chem. Sci.*, 5:1336–1347, 2014.

[62] H. Yu. Environmental carcinogenic polycyclic aromatic hydrocarbons: Photochemistry and phototoxicity. *J. Environ. Sci. Health C*, 20:149–183, 2002.

[63] P. P. Fu, Q. Xia, X. Sun, and H. Yu. Phototoxicity and environmental tranformation of polycyclic aromatic hydrocarbons (PAHs) – Light-induced reactive oxygen species, lipid peroxidation, and DNA damage. *J. Environ. Sci. Health C*, 30:1–41, 2012.

[64] P. Boffetta, N. Jourenkova, and P. Gustavsson. Cancer risk from occupational and environmental exposure to polycyclic aromatic hydrocarbons. *Cancer Causes Control*, 8:444–472, 1997.

[65] Q. Xia, J. J. Yin, Y. Zhao, Y. S. Wu, Y. Q. Wang, L. Ma, S. Chen, X. Sun, P. P. Fu, and H. Yu. UVA photoirradiation of nitro-polycyclic aromatic hydrocarbons – Induction of reactive oxygen species and formation of lipid peroxides. *Int. J. Environ. Res. Public Health*, 10:1062–1084, 2013.

[66] A. H. Zewail. Femtochemistry: Atomic-scale dynamics of the chemical bond using ultrafast lasers (Nobel lecture). *Angew. Chem. Int. Ed.*, 39:2586–2631, 2000.

[67] M. Olivucci, editor. *Computational Photochemistry.* Number 16 in Theoretical and Computational Chemistry. Elsevier B.V., Amsterdam, 2005.

[68] J. C. Tully and R. K. Preston. Trajectory surface hopping approach to nonadiabatic molecular collisions: The reaction of H^+ with D_2. *J. Chem. Phys,*, 55:562–572, 1971.

[69] J. C. Tully. Molecular dynamics with electronic transitions. *J. Chem. Phys.*, 93:1061–1071, 1990.

[70] M. Barbatti. Nonadiacatic dynamics with trajectory surface hopping methods. *WIREs Comput. Mol. Sci.*, 1:620, 2011.

[71] M. Richter, P. Marquetand, J. González-Vázquez, I. Sola, and L. González. SHARC: *ab initio* molecular dynamics with surface hopping in the adiabatic representation including arbitrary couplings. *J. Chem. Theory Comput.*, 7:1253–1258, 2011.

[72] S. Mai, M. Richter, M. Ruckenbauer, M. Oppel, P. Marquetand, and L. González. SHARC: Surface hopping including arbitrary couplings – program package for non-adiabatic dynamics. sharc-md.org, 2014.

[73] F. Jensen. *Introduction to Computational Chemistry*. John Wiley & Sons, Ltd., 2007.

[74] A. Szabo and N. S. Ostlund. *Modern Quantum Chemistry*. Dover Publications, Inc. Mineola, New York, 1996.

[75] B. O. Roos. Multiconfigurational quantum chemistry for ground and excited states. In M. K. Shukla and J. Leszczynski, editors, *Radiation Induced Molecular Phenomena in Nucleic Acids*, pages 125–156. Springer, 2008.

[76] B. O. Roos, P. R. Taylor, and P. E. M. Siegbahn. A complete active space SCF method (CASSCF) using a density matrix formulated super-CI approach. *Chem. Phys.*, 48:157–173, 1980.

[77] K. Andersson, P.-Å. Malmqvist, B. J. Roos, A. J. Sadlej, and K. Wolinski. Second-order perturbation theory with a CASSCF reference function. *J. Phys. Chem.*, 94:5483–5488, 1990.

[78] K. Andersson, P.-Å. Malmqvist, and B. J. Roos. Second-order perturbation theory with a complete active space self-consistent field reference function. *J. Chem. Phys.*, 96:1218–1226, 1992.

[79] K. G. Dyall. The choice of a zeroth-order Hamiltonian for second-order perturbation theory with a complete active space self-consistent-field reference function. *J. Chem. Phys.*, 102:4909–4918, 1995.

[80] C. Angeli, R. Cimiraglia, and J.-P. Malrieu. On a mixed Møller-Plesset Epstein-Nesbet partition of the Hamiltonian to be used in multireference perturbation configuration interaction. *Chem. Phys. Lett.*, 317:472–480, 2000.

[81] C. Angeli, R. Cimiraglia, S. Evangelisti, T. Leininger, and J.-P. Malrieu. Introduction of the n-electron valence states for multireference perturbation theory. *J. Chem. Phys.*, 114:10252–10264, 2001.

[82] C. J. Cramer. *Essentials of Computational Chemistry: Theories and Models*. John Wiley & Sons, Ltd., 2004.

[83] M. E. Casida. Time-dependent density-functional theory for molecules and molecular solids. *J. Mol. Struct.: THEOCHEM*, 914:3–18, 2009.

[84] A. Dreuw and M. Head-Gordon. Single reference ab initio methods for the calculation of excited states of large molecules. *Chem. Rev.*, 105:4009–4037, 2005.

[85] E. K. U. Gross and N. T. Maitra. Introduction to TDDFT. In M. A. L. Marques, N. T. Maitra, F. M. S. Nogueira, E. K. U. Gross, and A. Rubio, editors, *Fundamentals of Time-Dependent Density Functional Theory*, chapter 13. Springer Verlag Berlin Heidelberg, 2012.

[86] S. Hirata and M. Head-Gordon. Time-dependent density functional theory within the Tamm-Dancoff approximation. *Chem. Phys. Lett.*, 314:291–299, 1999.

[87] F. Plasser and H. Lischka. Analysis of excitonic and charge transfer interactions from quantum chemical calculations. *J. Chem. Theory Comput.*, 8:2777–2789, 2012.

[88] F. Plasser, M. Wormit, and A. Dreuw. New tools for the systematic analysis and visualization of electronic excitations. I. Formalism. *J. Chem. Phys.*, 141:024106, 2014.

[89] S. A. Mewes, J.-M. Mewes, A. Dreuw, and F. Plasser. Excitons in poly(para phenylene vinylene): a quantum-chemical perspective based on high-level ab initio calculations. *Phys. Chem. Chem. Phys.*, 18:2548–2563, 2016.

[90] F. Plasser. TheoDORE 1.4: a package for theoretical density, orbital relaxation, and exciton analysis; available from `http://theodore-qc.sourceforge.net`.

[91] M. Reiher and A. Wolf. *Relativistic Quantum Chemistry*, chapter 16. Wiley VCH Verlag GmbH & Co. KGaA, Weinheim, 2009.

[92] C. M. Marian. Spin-orbit coupling in molecules. In K. B. Lipkowitz and D. B. Boyd, editors, *Reviews in Computational Chemistry*, volume 17. Wiley VCH New York, 2001.

[93] C. M. Marian. Spin-orbit coupling and intersystem crossing in molecules. *WIREs Comput. Mol. Sci.*, 2:187–203, 2012.

[94] M. A. El-Sayed. The triplet state: Its radiative and nonradiative properties. *Acc. Chem. Res.*, 1:8–16, 1968.

[95] H. M. Senn and W. Thiel. QM/MM methods for biomolecular systems. *Angew. Chem. Int. Ed.*, 48:1198–1229, 2009.

[96] S. Miertuš, E. Scrocco, and J. Tomasi. Electrostatic interaction of a solute with a continuum. A direct utilizaion of ab initio molecular potentials for the prevision of solvent effects. *Chem. Phys.*, 55:117–129, 1981.

[97] A. Klamt and G. Schüürmann. COSMO: a new approach to the dielectric screening in solvents with explicit expressions for the screening energy and its gradient. *J. Chem. Soc. Perkin Trans. 2*, pages 799–805, 1993.

[98] D. R. Yarkony. Conical intersections: Their description and consequences. In W. Domcke, D. R. Yarkony, and H. Köppel, editors, *Conical Intersections*, number 15 in Advanced Series in Physical Chemistry, chapter 2. World Scientific Publishing Co. Pte. Ltd., 2004.

[99] L. Verlet. Computer "experiments" on classical fluids. I. Thermodynamical properties of Lennard-Jones molecules. *Phys. Rev.*, 159:98–103, 1967.

[100] L. Verlet. Computer "experiments" on classical fluids. II. Equilibrium correlation functions. *Phys. Rev.*, 165:201–214, 1968.

[101] G. Granucci and M. Persico. Critical appraisal of the fewest-switches algorithm for surface hopping. *J. Chem. Phys,*, 126:134114, 2007.

[102] G. Granucci, M. Persico, and G. Spighi. Surface hopping trajectory simulations with spin-orbit and dynamical couplings. *J. Chem. Phys.*, 137:22A501, 2012.

[103] B. F. Habenicht and O. V. Prezhdo. Ab initio time-domain study of the triplet state in a semiconducting carbon nanotube: Intersystem crossing, phosphorescence time, and line width. *J. Am. Chem. Soc.*, 134:15648–15651, 2012.

[104] G. Cui and W. Thiel. Intersystem crossing enables 4-thiothymine to act as a photosensitizer in photodynamic therapy: An ab initio QM/MM study. *J. Phys. Chem. Lett.*, 5:2682–2687, 2014.

[105] F. F. de Carvalho and I. Tavernelli. Nonadiabatic dynamics with intersystem crossings: A time-dependent density functional theory implementation. *J. Chem. Phys,*, 143:224105, 2015.

[106] S. Mai, P. Marquetand, and L. González. A general method to describe intersystem crossing in trajectory surface hopping. *Int. J. Quant. Chem.*, 115:1215–1231, 2015.

[107] D. B. Galloway, J. A. Bartz, L. G. Huey, and F. F. Crim. Pathways and kinetic energy disposal in the photodissociation of nitrobenzene. *J. Chem. Phys.*, 98:2107, 1993.

[108] Y.-M. Li, J.-L. Sun, H.-M. Yin, K.-L. Han, and G.-Z. He. Photodissociation of nitrobenzene at 266 nm: Experimental and theoretical approach. *J. Chem. Phys.*, 118:6244, 2003.

[109] R. Yang, X. Jin, W. Wang, K Fan, and M. Zhou. Infrared spectra of phenyl nitrite and phenoxyl radical-nitric oxide complex in solid argon. *J. Phys. Chem. A*, 109:4261, 2005.

[110] X.-M. Zhu, S.-Q. Zhang, X. Zheng, and D. L. Phillips. Resonance raman study of short-time photodissociation dynamics of the charge-transfer band absorption of nitrobenzene in cyclohexane solution. *J. Phys. Chem. A*, 109:3086–3093, 2005.

[111] Y. He, A. Gahlmann, J. S. Feenstra, S. T. Park, and A. H. Zewail. Ultrafast electron diffraction: Structural dynamics of molecular rearrangement in the NO release from nitrobenzene. *Chem. Asian J.*, 1:56–63, 2006.

[112] M.-F. Lin, Y. T. Lee, C.-K. Ni, S. Xu, and M. C. Lin. Photodissociation dynamics of nitrobenzene and *o*-nitrotoluene. *J. Chem. Phys.*, 126:064310, 2007.

[113] M. L. Hause, N. Herath, R. Zhu, M. C. Lin, and A. G. Suits. Roaming-mediated isomerization in the photodissociation of nitrobenzene. *Nature Chemistry*, 3:932–937, 2011.

[114] S. H. Hastings and F. A. Matsen. The photodecompositon of nitrobenzene. *J. Am. Chem. Soc.*, 70:3514–3515, 1948.

[115] S. Nagakura, M. Kojima, and Y. Maruyama. Electronic spectra and electronic structures of nitrobenzene and nitromesitylene. *J. Mol. Spec.*, 13:174–192, 1964.

[116] B. Vidal and J. N. Murrell. The effect of solvent on the position of the first absorption band of nitrobenzene. *Chem. Phys. Lett.*, 31:46–47, 1975.

[117] H. K. Sinha and K. Yates. Ground- and excited-state dipole moments of some nitroaromatics: Evidence for extensive charge-transfer in twisted nitrobenzene systems. *J. Chem. Phys.*, 93:7085–7093, 1990.

[118] K. J. Castle, J. E. Abbott, X. Peng, and W. Kong. Direction of the transition dipole moment of nitrobenzene determined from oriented molecules in a uniform electric field. *J. Chem. Phys.*, 113:1415–1419, 2000.

[119] J. E. Abbott, X. Peng, and W. Kong. Symmetry properties of electronically excited states of nitroaromatic compounds. *J. Chem. Phys.*, 117:8670–8675, 2002.

[120] A. Kawski, B. Kukliński, and P. Bojarski. Excited S_1 state dipole moments of nitrobenzene and *p*-nitroaniline from thermochromic effect on electronic absorption spectra. *Chem. Phys.*, 330:307–312, 2006.

[121] O. Kröhl, K. Malsch, and P. Swiderek. The electronic states of nitrobenzene: electron-energy loss spectroscopy and CASPT2 calculations. *Phys. Chem. Chem. Phys.*, 2:947–953, 2000.

[122] J. Quenneville, M. Greenfield, D. S. Moore, S. D. McGrane, and R. J. Scharff. Quantum chemistry studies of electronically excited nitrobenzene, TNA, and TNT. *J. Phys. Chem. A*, 115:12286–12297, 2011.

[123] J.-M. Mewes, V. Jovanović, C. M. Marian, and A. Dreuw. On the molecular mechanism of non-radiative decay of nitrobenzene and the unforeseen challenges this simple molecule holds for electronic structure theory. *Phys. Chem. Chem. Phys.*, 16:12393–12406, 2014.

[124] K. Coutinho, S. Canuto, and M. C. Zerner. A Monte Carlo-quantum mechanics study of the solvatochromic shifts of the lowest transition of benzene. *J. Chem. Phys.*, 112:9874–9880, 2000.

[125] U. F. Röhrig, I. Frank, J. Hutter, A. Laio, J. van de Vondele, and U. Rothlisberger. QM/MM Car-Parrinello molecular dynamics study of the solvent effects on the ground state and on the first excited singlet state of acetone in water. *ChemPhysChem*, 4:1177–1182, 2003.

[126] N. A. Besley, M. T. Oakley, A. J. Cowan, and J. D. Hirst. A sequential molecular mechanics/quantum mechanics study of the electronic spectra of amides. *J. Am. Chem. Soc.*, 126:13502–13511, 2004.

[127] W. L. Jorgensen, J. Chandrasekhar, J. D. Madura, R. W. Impey, and M. L. Klein. Comparison of simple potential functions for simulationg liquid water. *J. Chem. Phys.*, 79:926–935, 1983.

[128] J. Wang, R. M. Wolf, J. W. Caldwell, P. A. Kollman, and D. A. Case. Development and testing of a general Amber force field. *J. Comput. Chem.*, 25:1157–1174, 2004.

[129] J. Finley, P.-Å. Malmqvist, B. J. Roos, and L. Serrano-Andrés. The multi-state CASPT2 method. *Chem. Phys. Lett.*, 288:299–306, 1998.

[130] P.-O. Widmark, P.-Å. Malmqvist, and B. J. Roos. Density matrix averaged atomic natural orbital (ANO) basis sets for correlated molecular wave functions. *Theor. Chim. Acta*, 77:291–306, 1990.

[131] J. P. Zobel, J. J. Nogueira, and L. González. Quenching of charge transfer in nitrobenzene induced by vibrational motion. *J. Phys. Chem. Lett.*, 6:3006–3011, 2015.

[132] S. A. Adcock and J. A. McCammon. Molecular dynamics: Survey of methods for simulating the activity of proteins. *Chem. Rev.*, 106:1589–1615, 2006.

[133] N. Metropolis, A. W. Rosenbluth, M. N. Rosenbluth, A. H. Teller, and E. Teller. Equation of state calculations by fast computing machines. *J. Chem. Phys.*, 21:1087–1092, 1953.

[134] M. Barbatti and K. Sen. Effects of different initial condition sampling on photodynamics and spectrum of pyrrole. *Int. J. Quant. Chem.*, 116:762–771, 2016.

[135] E. Wigner. On the quantum correction for thermodynamic equilibrium. *Phys. Rev.*, 40:749–759, 1932.

[136] T. L. Curtright, D. B. Fairlie, and C. K. Zachos. *A Concise Treatise on Quantum Mechanics in Phase Space*. World Scientific Publishing Co. Pte. Ltd., 2014.

[137] M. Ruckenbauer, M. Barbatti, T. Müller, and H. Lischka. Nonadiabatic excited-state dynamics with hybrid ab initio quantum-mechanical/molecular-mechanical methods: Solvation of the pentadieniminium cation in apolar media. *J. Phys. Chem. A*, 114:6757–6765, 2010.

[138] P. Gupta, W. P. Harger, and J. Arey. The contribution of nitro- and methylnitro-naphthalenes to the vapor-phase mutagenicity of ambient air samples. *Atmospheric Environment*, 30:3157–3166, 1996.

[139] C. E. Crespo-Hernández, R. A. Vogt, and B. Sealey. On the primary reaction pathway in the photochemistry of nitro-polycyclic aromatic hydrocarbons. *Mod. Chem. Appl.*, 1:1000106, 2013.

[140] J. P. Zobel, M. Heindl, J. J. Nogueira, and L. González. Vibrational sampling and solvent effects on the electronic structure of the absorption spectrum of 2-nitronaphthalene, submitted, 2018.

[141] J. W. Caldwell and P. A. Kollman. Structure and properties of neat liquids using nonadditive molecular dynamics: Water, methanol, and n-methylacetamide. *J. Phys. Chem.*, 99:6208–6219, 1995.

[142] A. D. Becke. Density-functional thermochemistry. III. The role of exact exchange. *J. Chem. Phys.*, 98:5648–5652, 1993.

[143] C. Lee, W. Yang, and R. G. Parr. Development of the Colle-Salvetti correlation-energy formula into a functional of the electron density. *Phys. Rev. B*, 37:785–789, 1988.

[144] S. H. Vosko, L. Wilk, and M. Nusair. Accurate spin-dependent electron liquid correlation energies for local spin density calculations: a critical analysis. *Can. J. Phys.*, 58:1200–1211, 1980.

[145] P. J. Stephens, F. J. Devlin, C. F. Chabalowski, and M. J. Frisch. Ab initio calculation of vibrational absorption and circular dichroism spectra using density functional force fields. *J. Phys. Chem.*, 98:11623–11627, 1994.

[146] F. Weigend and R. Ahlrichs. Balanced basis sets of split valence, triple zeta valence and quadruple zeta valence quality for H to Rn: Design and assessment of accuracy. *Phys. Chem. Chem. Phys.*, 7:3297–3305, 2005.

[147] C. Adamo and V. Barone. Toward reliable density functional methods without adjustable parameters: The PBE0 model. *J. Chem. Phys.*, 110:6158–6170, 1999.

[148] M. Kojima and S. Nagakura. Electronic spectra and electronic structures of α- and β-nitronaphthalenes and 1,8-dinitronapthalene. *Bull. Chem. Soc. Jpn.*, 39:1262–1269, 1966.

[149] V. Bonačić-Koutecký and R. Mitrić. Theoretical exploration of ultrafast dynamics in atomic clusters: Analysis and control. *Chem. Rev.*, 105:11–65, 2005.

[150] M. Barbatti, A. J. A. Aquino, and H. Lischka. The UV absorption spectrum of nucleobases: semi-classical ab initio spectra simulations. *Phys. Chem. Chem. Phys.*, 12:4959–4967, 2010.

[151] R. Crespo-Otero and M. Barbatti. Spectrum simulation and decomposition with nuclear ensemble: formal derivation and application to benzene, furan, and 2-phenylfuran. *Theor. Chem. Acc.*, 131:1237, 2012.

[152] L. Du and Z. Lan. An on-the-fly surface-hopping program JADE for nonadiabatic molecular dynamics of polyatomic systems: Implementation and applications. *J. Chem. Theory Comput.*, 11:1360–1374, 2015.

[153] R. Mitrić, Hartmann M., J. Pittner, and V. Bonačić-Koutecký. New strategy for optimal control of femtosecond pump-dump processes. *J. Phys. Chem. A*, 106:10477–10481, 2002.

[154] V. Bonačić-Koutecký, R. Mitrić, U. Werner, L. Wöste, and R. S. Berry. Ultrafast dynamics in atomic clusters: Analysis and control. *PNAS*, 103:10594–10599, 2006.

[155] R. Mitrić and J. Petersen. Electronic coherence wiwith the semiclassical field-induced surface hopping method: strong field control in K_2. *Phys. Chem. Chem. Phys.*, 14:8299–8306, 2012.

[156] J. Giegerich, J. Petersen, R. Mitrić, and I. Fischer. Photodissocation dynamics in propargylene, HCCCH. *Phys. Chem. Chem. Phys.*, 16:6294–6302, 2014.

[157] P. G. Lisinetskaya, C. Braun, S. Proch, Y. D. Kim, G. Ganteför, and R. Mitrić. Excited state nonadiabatic dynamics of bare and hydrated anion gold cluster $Au_3^-[H_2O]_n$ (n = 0-2). *Phys. Chem. Chem. Phys.*, 18:6411–6419, 2016.

[158] M. I. S. Röhr, R. Mitrić, and J. Petersen. Vibrationally resolved optical spectra and ultrafast electronic relaxation dynamics of diamantane. *Phys. Chem. Chem. Phys.*, 18:8701–8709, 2016.

[159] M. Hillery, R. F. O'Connell, M. O. Scully, and E. P. Wigner. Distribution functions in physics: Fundamentals. *Physics Reports*, 106:121–167, 1984.

[160] R. P. Feynman. Simulating physics with computers. *Int. J. Theor. Phys.*, 21:467–488, 1982.

[161] R. P. Feynman. Negative probability. In B. J. Hiley and F. D. Peat, editors, *Quantum Implications: Essays in Honour of David Bohm*, chapter 13. Routledge & Kegan Paul Ltd., 1987.

[162] D. Leibfried, T. Pfau, and C. Monroe. Shadows and mirrors: Reconstructing quantum states of atom motion. *Physics Today*, 51:22–28, 1998.

[163] M. Schreiber, M. R. Silva-Junior, S. P. A. Sauer, and W. Thiel. Benchmarks for electronically excited states: CASPT2, CC2, CCSD, and CC3. *J. Chem. Phys,*, 128:134110, 2008.

[164] M. J. Frisch, G. W. Trucks, H. B. Schlegel, G. E. Scuseria, M. A. Robb, J. R. Cheeseman, G. Scalmani, V. Barone, B. Mennucci, G. A. Petersson, H. Nakatsuji, M. Caricato, X. Li, H. P. Hratchian, A. F. Izmaylov, J. Bloino, G. Zheng, J. L. Sonnenberg, M. Hada, M. Ehara, K. Toyota, R. Fukuda, J. Hasegawa, M. Ishida, T. Nakajima, Y. Honda, O. Kitao, H. Nakai, T. Vreven, J. A. Montgomery Jr., J. E. Peralta, F. Ogliaro, M. Bearpark, J. J. Heyd, E. Brothers, K. N. Kudin, V. N. Staroverov, R. Kobayashi, J. Normand, K. Raghavachari, A. Rendell, J. C. Burant, S. S. Iyengar, J. Tomasi, M. Cossi, N. Rega, J. M. Millam, M. Klene, J. E. Knox, J. B. Cross, V. Bakken, C. Adamo, J. Jaramillo, R. Gomperts, R. E. Stratmann, O. Yazyev, A. J. Austin, R. Cammi, C. Pomelli, J. W. Ochterski, R. L. Martin, K. Morokuma, V. G. Zakrzewski, G. A. Voth, P. Salvador, J. J. Dannenberg, S. Dapprich, A. D. Daniels, Ö. Farkas, J. B. Foresman, J. V. Ortiz, J. Cioslowski, and D. J. Fox. Gaussian 09, Revision E.01, Gaussian, Inc., Wallingford CT, 2009.

[165] D. Roca-Sanjuán, F. Aquilante, and R. Lindh. Multiconfiguration second-order perturbation theory approach to strong electron correlation in chemistry and photochemistry. *WIREs Comput. Mol. Sci.*, 2:585–603, 2012.

[166] J. P. Zobel, J. J. Nogueira, and L. González. The IPEA dilemma in CASPT2. *Chem. Sci.*, 8:1482–1499, 2017.

[167] B. O. Roos, V. Veryazov, and P.-O. Widmark. Relativistic atomic natural orbital type basis sets for the alkaline and alkaline-earth atoms applied to the ground-state potentials for the corresponding dimers. *Theor. Chem. Acc.*, 111:345–351, 2004.

[168] G. Ghigo, B. O. Roos, and P.-Å. Malmqvist. A modified definition of the zeroth-order hamiltonian in multiconfigurational perturbation theory CASPT2. *Chem. Phys. Lett.*, 396:142–149, 2004.

[169] http://www.molcas.org/ano/indexc.html.

[170] K. Andersson and B. O. Roos. Multiconfigurational second-order perturbation theory: A test of geometries and binding energies. *Int. J. Quant. Chem.*, 45:591–607, 1993.

[171] K. Andersson. Different forms of the zeroth-order Hamiltonian in second-order perturbation theory with a complete actice space self-consistent field reference function. *Theor. Chim. Acta*, 91:31–46, 1995.

[172] M. Kepenekian, V. Robert, and B. Le Guennic. What zeroth-order Hamiltonian for CASPT2 adiabatic energetics of Fe(II)N_6 architectures? *J. Chem. Phys.*, 131:114702, 2009.

[173] M. P. Fülscher, K. Andersson, and B. O. Roos. Toward an accurate molecular orbital theory for excited states: The azabenzenes. *J. Phys. Chem.*, 96:9204–9212, 1992.

[174] L. Serrano-Andrés, M. Merchán, I. Nebot-Gil, B. O. Roos, and M. P. Fülscher. Theoretical study of the electronic spectra of cyclopentadiene, pyrrole, and furan. *J. Am. Chem. Soc.*, 115:6184–6197, 1993.

[175] L. Serrano-Andrés, R. Lindh, B. O. Roos, and M. Merchán. Theoretical study of the electronic spectrum of *all-trans*-1,3,5,7-octatetraene. *J. Phys. Chem.*, 97:9360–9368, 1993.

[176] M. Rubio, M. Merchán, E. Ortí, and B. O. Roos. A theoretical study of the electronic spectrum of naphthalene. *Chem. Phys*, 179:395–409, 1994.

[177] M. P. Fülscher and B. O. Roos. The excited states of pyrazine: A basis set study. *Theor. Chim. Acta*, 87:403–413, 1994.

[178] B. O. Roos, M. Merchán, R. McDiarmid, and X. Xing. Theoretical and experimental determination of the electronic spectrum of norbornadiene. *J. Am. Chem. Soc.*, 116:5927–5936, 1994.

[179] J. Lorentzon, P.-Å. Malmqvist, M. P. Fülscher, and B. O. Roos. A CASPT2 study of the valence and lowest Rydberg electronic states of benzene and phenol. *Theor. Chim. Acta*, 91:91–108, 1995.

[180] P. Borowski, M. P. Fülscher, P.-Å. Malmqvist, and B. O. Roos. A theoretical study of the low-lying excited states of ozone. *Chem. Phys. Lett.*, 237:195–203, 1995.

[181] M. Merchán and B. O. Roos. A theoretical determination of the electronic spectrum of formaldehyde. *Theor. Chim. Acta*, 92:227–239, 1995.

[182] B. O. Roos, K. Andersson, M. P. Fülscher, L. Serrano-Andrés, K. Pierloot, M. Merchán, and V. Molina. Applications of level shift corrected perturbation theory in eletronic spectroscopy. *J. Mol. Struct. (THEOCHEM)*, 388:257–276, 1996.

[183] L. Serrano-Andrés and M. P. Fülscher. Theoretical study of the electronic spectroscopy of peptides. 2. Glycine and *N*-acetylglycine. *J. Am. Chem. Soc.*, 118:12200–12206, 1996.

[184] L. Serrano-Andrés, M. P. Fülscher, B. O. Roos, and M. Merchán. Theoretical study of the electronic spectrum of imidazole. *J. Phys. Chem.*, 100:6484–6491, 1996.

[185] L. Serrano-Andrés and B. O. Roos. Theoretical study of the absorption and emission spectra of indole in the gas phase and in a solvent. *J. Am. Chem. Soc.*, 118:185–195, 1996.

[186] M. E. Beck, R. Rebentisch, G. Hohlneicher, M. P. Fülscher, L. Serrano-Andrés, and B. O. Roos. Vertical and adiabatic electronic excitations in biphenylene: A theoretical study. *J. Chem. Phys.*, 107:9464–9474, 1997.

[187] V. Molina, M. Merchán, and B. O. Roos. Theoretical study of the electronic spectrum of *trans*-stilbene. *J. Phys. Chem. A*, 101:3478–3487, 1997.

[188] L. Serrano-Andrés, M. P. Fülscher, and G. Karlström. Solvent effects on electronic spectra studies by multiconfigurational perturbation theory. *Int. J. Quant. Chem.*, 65:167–181, 1997.

[189] M. P. Fülscher, L. Serrano-Andrés, and B. O. Roos. A theoretical study of the electronic spectra of adenine and guanine. *J. Am. Chem. Soc.*, 119:6168–6176, 1997.

[190] K. Malsch, R. Rebentisch, P. Swiderek, and G. Hohlneicher. Excited states of acetylene: a CASPT2 study. *Theor. Chem. Acc.*, 100:171–182, 1998.

[191] L. Serrano-Andrés, M. Merchán, M. Rubio, and B. O. Roos. Interpretation of the electronic absorption spectrum of free base porphin by using multiconfigurational second-order perturbation theory. *Chem. Phys. Lett.*, 295:195–203, 1995.

[192] V. Molina, M. Merchán, and B. O. Roos. A theoretical study of the electronic spectrum of *cis*-stilbene. *Spectrochim. Acta, Part A*, 55:433–446, 1999.

[193] M. Rubio and B. O. Roos. A theoretical study of the electronic spectrum of *s*-tetrazine. *Mol. Phys.*, 96:603–615, 1999.

[194] V. Molina, B. R. Smith, and M. Merchán. A theoretical study of the electronic spectrum of styrene. *Chem. Phys. Lett.*, 309:486–494, 1999.

[195] R. González-Luque, M. Merchán, and B. O. Roos. Multiconfigurational perturbation theory CASPT2 applied to the study of the low-lying singlet and triplet states of cyclopropene. *Z. Phys. D*, 36:311–316, 1996.

[196] A. C. Borin and L. Serrano-Andrés. An ab initio study of the low-lying ^{1}A' electronic states of indene. *J. Mol. Struct. (THEOCHEM)*, 464:121–128, 1999.

[197] M. Merchán, L. Serrano-Andrés, L. S. Slater, B. O. Roos, R. McDiarmid, and X. Xing. Electronic spectra of 1,4-cyclohexadiene and 1,3-cyclohexadiene: A combined experimental and theoretical investigation. *J. Phys. Chem. A*, 103:5468–5476, 1999.

[198] Z.-L. Cai and J. R. Reimers. The low-lying excited states of pyridine. *J. Phys. Chem. A*, 104:8389–8408, 2000.

[199] A. C. Borin and L. Serrano-Andrés. A theoretical study if the absorption spectra of indole and its analogs: indene, benzimidazole, and 7-azaindole. *Chem. Phys.*, 262:253–265, 2000.

[200] V. Molina and M. Merchán. Theoretical analysis of the electronic spectra of benzaldehyde. *J. Phys. Chem. A*, 105:3745–3751, 2001.

[201] B. O. Roos, P.-Å. Malmqvist, V. Molina, L. Serrano-Andrés, and M. Merchán. Theoretical characterization of the lowest-energy absorption band of pyrrole. *J. Chem. Phys.*, 116:7526–7535, 2002.

[202] L. Serrano-Andrés, R. Pou-Amérigo, M. P. Fülscher, and A. C. Borin. Electronic excited states of conjugated cyclic ketones and thioketones: A theoretical study. *J. Chem. Phys.*, 117:1649–1659, 2002.

[203] J. Weber, K. Malsch, and G. Hohlneicher. Excited electronic states of *p*-benzoquinone. *Chem. Phys.*, 264:275–318, 2001.

[204] T. Climent, R. González-Luque, and M. Merchán. Theoretical analysis of the excited states of maleimide. *J. Phys. Chem. A*, 107:6995–7003, 2003.

[205] A. C. Borin, L. Serrano-Andrés, V. Ludwig, and S. Canuto. Theoretical absorption and emission spectra of $1H$- and $2H$-benzotriazole. *Phys. Chem. Chem. Phys.*, 5:5001–5009, 2003.

[206] F. Aquilante, M. Cossi, O. Crescenzi, G. Scalmani, and V. Barone. Computation of the acetone ultraviolet spectrum in gas phase and in aqueous solution by a mixes discrete/continuum model. *Mol. Phys.*, 101:1945–1953, 2003.

[207] A. Murakami, T. Kobayashi, A. Goldberg, and S. Nakamura. CASSCF and CASPT2 studies of the structures, transition energies, and dipole moments of ground and excited states for azulene. *J. Chem. Phys.*, 120:1245–1252, 2004.

[208] M. Rubio, M. Merchán, R. Pou-Amérigo, and E. Ortí. The low-lying excited states of 2,2'-bithiophene: A theoretical analysis. *ChemPhysChem*, 4:1308–1315, 2003.

[209] F. Aquilante, V. Barone, and B. O. Roos. A theoretical investigation of valence and rydberg electronic states of acrolein. *J. Chem. Phys.*, 119:12323–12334, 2003.

[210] D. Guillaumont, C. Daniel, and A. Vlček Jr. Electronic structure of the lowest excited states of $Cr(CO)_4$(2,2'-bipyridine): A CASSCF/CASPT2 analysis. *Inorg. Chem.*, 36:1684–1688, 1997.

[211] M. Geleijns, C. de Graaf, R. Broer, and W. C. Nieuwpoort. Theoretical study of local electronic ttransition in the NiO(100) surface. *Surf. Sci.*, 421:106–115, 1999.

[212] C. de Graaf, R. Broer, and W. C. Nieuwpoort. Electron correlation effects in the d-d excitations in NiO. *Chem. Phys.*, 208:35–43, 1996.

[213] J. Bossert, N. Ben Amor, A. Strich, and C. Daniel. Electronic spectroscopy of HRe$(CO)_5$: a CASSCF/CASPT2 and TD-DFT study. *Chem. Phys. Lett.*, 342:617–624, 2001.

[214] M. R. J. Hachey and C. Daniel. The spectroscopy of HMn$(CO)_5$: A CASSCF/MRCI and CASPT2 ab initio study. *Inorg. Chem.*, 37:1387–1391, 1998.

[215] M. F. A. Hendrickx, L. F. Chibotaru, and A. Ceulemans. The electronic structure and spectrum of $\mathrm{Mo(CN)}_8^{3-}$. *Inorg. Chem.*, 42:590–597, 2003.

[216] M. F. A. Hendrickx, V. S. Mironov, L. F. Chibotaru, and A. Ceulemans. Assignment of the electronic spectra of $[\mathrm{Mo(CN)}_8]^{4-}$ and $[\mathrm{W(CN)}_8]^{4-}$ by ab initio calculations. *Inorg. Chem.*, 43:3142–3150, 2004.

[217] M. F. A. Hendrickx, V. S. Mironov, L. F. Chibotaru, and A. Ceulemans. An ab initio study of the ligand field and charge-transfer transition of $\mathrm{Cr(CN)}_6^{3-}$ and $\mathrm{Mo(CN)}_6^{3-}$. *J. Am. Chem. Soc.*, 125:3694–3695, 2003.

[218] O. Kühn, M. R. J. Hachey, M. M. Rohmer, and C. Daniel. A CASSCF/CASPT2 study of the low-lying excited states of $\mathrm{Mn_2(CO)_{10}}$. *Chem. Phys. Lett.*, 322:199–206, 2000.

[219] K. Pierloot, E. Van Praet, L. G. Vanquickenborne, and B. O. Roos. Systematic ab initio study of the ligand field spectra of hexacyanometalate complexes. *J. Phys. Chem.*, 97:12220–12228, 1993.

[220] K. Pierloot, E. Tsokos, and L. G. Vanquickenborne. Optical spectra of $\mathrm{Ni(CO)_4}$ and $\mathrm{Cr(CO)_6}$ revisited. *J. Phys. Chem.*, 100:16545–16550, 1996.

[221] C. Ribbing, B. Gilliams, K. Pierloot, B. O. Roos, and G. Karlström. The optical absorption spectrum of the octahedral RhCl_6^{3-} complex: *Ab Initio* calculations of excitation energies and the effect of spin-orbit coupling. *J. Chem. Phys.*, 109:3145–3151, 1998.

[222] S. Záliš, A. Vlček Jr., and C. Daniel. The character of low-lying excited states of mixed-ligand metal carbonyls. TD-DFT and CASSCF/CASPT2 study of $[\mathrm{W(CO)_4L}]$ (L = ethylenediamine, *N,N'*-dialkyl-1,4-diazabutadiene) and $[\mathrm{W(CO)_5L}]$ (L = pyridine, 4-cyanopyridine). *Collect. Czech. Chem. Commun.*, 68:89–104, 2003.

[223] W. J. Hehre, R. Ditchfield, and J. A. Pople. Self-consistend molecular orbital methods. XII. Further extensions of Gaussian-type basis sets for use in molecular orbital studies of organic molecules. *J. Chem. Phys.*, 56:2257–2261, 1972.

[224] R. Krishnan, J. S. Binkley, R. Seeger, and J. A. Pople. Self-consistent molecular orbital methods. XX. A basis set for correlated wave functions. *J. Chem. Phys.*, 72:650–654, 1980.

[225] A. Schäfer, C. Huber, and R. Ahlrichs. Fully optimized contracted Gaussian basis sets of triple zeta valence quality for atoms Li to Kr. *J. Chem. Phys.*, 100:5829–5853, 1994.

[226] I. Schapiro, K. Sivalingam, and F. Neese. Assessment of n-electron valence state perturbation theory for vertical excitation energies. *J. Chem. Theory Comput.*, 9:3567–3580, 2013.

[227] P. H. P. Harbach, M. Wormit, and A. Dreuw. The third-order algebraic diagrammatic contruction method (ADC(3)) for the polarization propagator for closed-shell molecules: Efficient implementation and benchmarking. *J. Chem. Phys.*, 141:064113, 2014.

[228] M. R. Silva-Junior, M. Schreiber, S. P. A. Sauer, and W. Thiel. Benchmarks for electronically excited states: Time-dependent density functional theory and density functional theory based multireference configuration interaction. *J. Chem. Phys.*, 129:104103, 2008.

[229] K. Pierloot and S. Vancoillie. Relative energy of the high-($^5T_{2g}$) and low-($^1A_{1g}$) spin states of $[Fe(H_2O)_6]^{2+}$, $[Fe(NH_3)_6]^{2+}$, and $[Fe(bpy)_3]^{2+}$: CASPT2 versus density functional theory. *J. Chem. Phys.*, 125:124303, 2006.

[230] K. Pierloot and S. Vancoillie. Relative energy of the high-($^5T_{2g}$) and low-($^1A_{1g}$) spin states of the ferrous complexes $[Fe(L)(NHS)_4]$: CASPT2 versus density functional theory. *J. Chem. Phys.*, 128:034104, 2008.

[231] M. Kepenekian, V. Robert, B. Le Guennic, and C. de Graaf. Energetics of $[Fe(NHC)_6]^{2+}$ via CASPT2 calculations: A spin-crossover perspective. *J. Comput. Chem.*, 30:2327–2333, 2009.

[232] A. Rudavskyi, C. Sousa, C. de Graaf, R. W. A. Havenith, and R. Broer. Computational approach to the study of thermal spin crossover phenomena. *J. Chem. Phys.*, 140:184318, 2014.

[233] N. Suaud, M.-L. Bonnet, C. Boilleau, P. Labèguerie, and N. Guihéry. Light-induced excited spin state trapping: Ab initio study of the physics at the molecular level. *J. Am. Chem. Soc.*, 131:715–722, 2009.

[234] L. M. Lawson Daku, F. Aquilante, T. W. Robinson, and A. Hauser. Accurate spin-state energetics of transition metal complexes. 1. CCSD(T), CASPT2, and DFT study of $[M(NCH)_6]^{2+}$ (M = Fe, Co). *J. Chem. Theory Comput.*, 8:4216–4231, 2012.

[235] S. Vela, M. Fumanal, J. Ribas-Ariño, and V. Robert. On the zeroth-order Hamiltonian for CASPT2 calculations of spin crossover compounds. *J. Comput. Chem.*, 37:947–953, 2016.

[236] J. J. Mikula, R. W. Anderson, L. E. Harris, and E. W. Stuebing. Electronic spectra and intramolecular energy transfer in 1-nitronaphthalene. *J. Mol. Spec.*, 42:350–369, 1972.

[237] Y. Orozco-Gonzalez, K. Coutinho, J. Peon, and S. Canuto. Theoretical study of the absorption and nonradiative deactivation of 1-nitronaphthalene in the low-lying singlet and triplet excited states including methanol and ethanol solvent effects. *J. Chem. Phys.*, 137:054307, 2012.

[238] A. Giussani. Toward the understanding of the photophysics and photochemistry of 1-nitronaphthalene under solar radiation: The first theoretical evidence of a photodegradation intramolecular rearrangement mechanism involving the triplet states. *J. Chem. Theory Comput.*, 10:3987–3995, 2014.

[239] M. Ernzerhof and G. E. Scuseria. Assessment of the Perdew-Burke-Ernzerhof exchange-correlation functional. *J. Chem. Phys.*, 110:5029–5036, 1999.

[240] D. P. Chong, E. van Lenthe, S. van Gisbergen, and E. J. Bearends. Even-tempered Slater-type orbitals revisited: From hydrogen to krypton. *J. Comput. Chem.*, 25:1030–1036, 2004.

[241] E. J. Baerends, T. Ziegler, A. J. Atkins, J. Autschbach, D. Bashford, A. Bérces, F. M. Bickelhaupt, C. Bo, P. M. Boerrigter, L. Cavallo, D. P. Chong, D. V. Chulhai, L. Deng, R. M. Dickson, J. M. Dieterich, D. E. Ellis, M. van Faassen, L. Fan, T. H. Fischer, C. Fonseca Guerra, M. Franchini, A. Ghysels, A. Giammona, S. J. A. van Gisbergen, A. W. Götz, J. A. Groeneveld, O. V. Gritsenko, M. Grüning, M. S. Gusarov, F.E. Harris, P. van den Hoek, C.R. Jacob, H. Jacobsen, L. Jensen, J. W. Kaminski, G. van Kessel, F. Kootstra, A. Kovalenko, M. V. Krykunov, E. van Lenthe, D. A. McCormack, A. Michalak, M. Mitoraj, S. M. Morton, J. Neugebauer, V. P. Nicu, L. Noodleman, V. P. Osinga, S. Patchkovskii, M. Pavanello, C. A. Peeples, P. H. T. Philipsen, D. Post, C. C. Pye, W. Ravenek, J. I. Rodríguez, P. Ros, R. Rüger, P. R. T. Schipper, H. van Schoot, G. Schreckenbach, J. S. Seldenthuis, M. Seth, J. G. Snijders, M. Solà, M. Swart, D. Swerhone, G. te Velde, P. Vernooijs, L. Versluis, L. Visscher, O. Visser, F. Wang, T. A. Wesolowski, E. M. van Wezenbeek, G. Wiesenekker, S. K . Wolff, T. K. Woo, and A. L. Yakovlev. ADF2016, SCM, Theoretical Chemistry, Vrije Universiteit, Amsterdam, The Netherlands, http://www.scm.com, 2016.

[242] M. Barbatti, G. Grannuci, M. Persico, M. Ruckenbauer, M. Vazdar, M. Eckert-Maksić, and H. Lischka. The on-the-fly surface-hopping program system NEWTON-X: Application to ab initio simulation of the nonadiabatic photodynamics of benchmark systems. *J. Photochem. Photobiol. A*, 190:228–240, 2007.

[243] J. P. Zobel, J. J. Nogueira, and L. González. The mechanism of ultrafast intersystem crossing in 2-nitronaphthalene. *Chem. Eur. J.*, 24:5379–5387, 2018.

[244] S. Nangia, A. W. Jasper, T. F. Miller III, and D. G. Truhlar. Army ants algorithm for rare event sampling of delocalized nonadiabatic transitions by trajectory surface hopping and the estimation of sampling errors by the bootstrap method. *J. Chem. Phys.*, 120:3586–3597, 2004.

[245] K. Kurtz, A. Hofmann, and R. de Vivie-Riedle. Ground state normal mode analysis: Linking excited state dynamics and experimental observables. *J. Chem. Phys.*, 114:6151–6159, 2001.

[246] F. Plasser, M. Barbatti, A. J. A. Aquino, and H. Lischka. Excited-state diproton transfer in [2,2'-bipyridyl]-3,3'-diol: the mechanism is sequential, not concerted. *J. Phys. Chem. A*, 113:8490–8499, 2009.

[247] T. H. Dunning Jr. Gaussian basis sets for use in correlated molecular calculations. I. The atoms boron through neon and hydrogen. *J. Chem. Phys.*, 90:1007–1023, 1989.

[248] L. Lang, editor. *Absorption Spectra in the Ultraviolet and Visible Region*, volume 8, page 151. Akademiai Kiado, 1967. Retrieved from `https://webbook.nist.gov/cgi/inchi?ID=C881038&Mask=400`.

List of Publications

Parts of the results included in this thesis have been published in the articles

1. J. Patrick Zobel, Juan J. Nogueira, and Leticia González.
   Quenching of Charge Transfer in Nitrobenzene Induced by Vibrational Motion.
   J. Phys. Chem. Lett., **6**, 3006–3001 (2015).
   `http://dx.doi.org/10.1021/acs.jpclett5b00990`

2. J. Patrick Zobel, Juan J. Nogueira, and Leticia González.
   The IPEA Dilemma in CASPT2.
   Chem. Sci., **8**, 1482–1499 (2017).
   `http://dx.doi.org/10.1039/c6sc03759c`

3. J. Patrick Zobel, Juan J. Nogueira, and Leticia González.
   The Mechanism of Ultrafast Intersystem Crossing in 2-Nitronaphthalene.
   Chem. Eur. J., accepted for publication (2018).
   `http://dx.doi.org/10.1002/chem.201705854`

For further results, three manuscripts are submitted/in preparation

- J. Patrick Zobel, Moritz Heindl, Juan J. Nogueira, and Leticia González.
  Vibrational Sampling and Solvent Effects on the Electronic Structure of the Absorption Spectrum of 2-Nitronaphthalene.
  Manuscript in revision in *J. Chem. Theory Comput.* (2018).

- J. Patrick Zobel, Juan J. Nogueira, and Leticia González.
  Finite Temperature Wigner Phase Space Sampling and Temperature Effects on the Excited-State Dynamics of 2-Nitronaphthalene.
  Manuscript in preparation (2018).

- J. Patrick Zobel, Juan J. Nogueira, and Leticia González.
  Ultrafast Intersystem Crossing Dynamics of Nitronaphthalene Derivatives.
  Manuscript in preparation (2018).

Acknowledgements

Although only one name graces the front page of this thesis, this work could not have been so successful without the help and support of many people. My deep gratitude goes to Prof. Leticia González and Dr. Juan José Nogueira for being my mentors and co-workers during the last four years. To Juanjo, I say “thank you” especially for the countless hours of discussions and your patient help whenever I got stuck in my work and for the even larger number of coffees and beers during and after the work (respectively) that we shared as such good friends. To Leti, I say “thank you” especially for teaching me the rules of the game in science, your patience while I was learning them, and for giving me your support whenever I was in need of it.

I am very grateful to Dr. Sebastian Mai, Dr. Andrew Atkins, and Dr. Felix Plasser for your help and teachings on SHARC, ADF, and TheoDORE, tools on which rests at least half of this thesis. I thank Dr. Markus Oppel, Jackie Klaura, Markus Hickel, and Dimitri Robl for taking care of our cluster and all my computer issues, which made my work much smoother and more efficient, and I thank Nicole Irmler, Irina Stumpf, and Monika Schett for all your help with my bureaucra(z)y, so that I could focus more on research.

Furthermore, I thank all other members of the González group: Davide Avagliano, Gustavo Cardenas, Dr. David Ferro, Dr. Leon Freitag, Dr. Michael Gastegger, Sandra Gómez, Moritz Heindl, Lea Ibele, Dr. Vera Krewald, Dr. Federico Latorre, Dr. Philipp Marquetand, Dr. Boris Maryasin, Maximilian Meixner, Maximilian Menger, Prof. Antonio Mota, Dr. Aurora Muñoz-Losa, Dr. Nicolas Ramos, Dr. Clemens Rauer, Dr. Martin Richter, Trini Romay-Piñeiro, Dr. Stefan Ruider, Dr. Matthias Ruckenbauer, Dr. Pedro Sánchez-Murcia, Isolde Sandler, Francesco Talotta, Martina De Vetta, and Julia Westermayr as well as numerous short-time students, guests, and extended members of the group during the last years. Each of you added parts to this thesis –some smaller, some larger –in too many ways to account here, and I am thankful for all of them.

I am also grateful to the Austrian Academy of Sciences for your support of my work through a DOC fellowship, the COST Action CM1405 for funding my short-term scientific mission in Santiago and Prof. Emilio Martínez-Núñez for your hospitality during my stay there, and to the Faculty of Chemistry of the University of Vienna for further financial support.

Finally, I thank my family –Eric, Heide, Kim, Yannik, Nils, Ylvi, and Oma –for providing me a home, a place that I always like to come back to, and for all your love and support so far. Simply knowing that you will continue to do so gives me more than enough confidence to further go my way.

Selbstständigkeitserklärung

Hiermit erkläre ich, dass ich die vorliegende Arbeit selbstständig und ohne Zuhilfenahme weiterer als der aufgeführten Quellen angefertigt habe. Alle wörtlich oder sinngemäß übernommenen Textstellen anderer Verfasser wurden als solche gekennzeichnet.

Wien, 2018

Curriculum Vitae

J. Patrick Zobel

Education

since 2014	PhD Studies in Chemistry, University of Vienna, Austria. Topic: 'Ultrafast Intersystem Crossing Dynamics in Organic Molecules', under the supervision of Univ-Prof. Dr. Leticia González, Institute of Theoretical Chemistry.
2011–2013	MSc in Chemistry (4 semesters), University of Heidelberg, Germany. Grade: 1,1. Distinction: "very good" (sehr gut), class rank 1 of 13.
2008–2011	BSc in Chemistry (6 semesters), University of Heidelberg, Germany. Grade: 1,4. Distinction: "very good" (sehr gut), class rank 2 of 15.
1998–2007	General Qualification for University Entrance (Abitur, 9 years), Lichtenbergschule Gymnasium Darmstadt, Germany. Grade: 1,4. Distinction "very good" (sehr gut).

Research Interests and Expertise

- Single- and multiconfigurational ab initio electronic structure methods (CASPT2, DFT, propagators, . . .).
- Nonadiabatic dynamics of organic molecules.
- Vibrational sampling techniques.
- Electronic decay processes in strongly relativistic systems.

Undergraduate Research Activities (Extracurricular)

2013-2014	Student research assistant in the group of Markus Pernpointner, Institute of Physical Chemistry, University of Heidelberg (10/2013-03/2014).
2012-2013	Student research assistant in the group of Peter Hofmann, Institute of Organic Chemistry, University of Heidelberg (10/2012-01/2013).
2011-2012	Student research assistant in the group of Markus Pernpointner, Institute of Physical Chemistry, University of Heidelberg (09/2011-05/2012).

Awards

2017	Selected as Young Researcher to Participate in the 67th Lindau Nobel Laureate Meeting.
2016	Short Term Scientific Mission (STSM) Grant of the COST Action CM1405 funded by the European Union.
2014	Doctoral Fellowship Program of the Austrian Academy of Sciences (DOC-Stipendium der ÖAW).
2013	Dr. Sophie Bernthsen Award of the University of Heidelberg for excellent performance in the study of chemistry.
2012	BASF scholarship of the 'Excellence in Molecular Chemistry' program funded by the Institutes of Inorganic and Organic Chemistry of the University of Heidelberg.

Publications

2018	6. J. P. Zobel, J. J. Nogueira and L. González, The Mechanism of Ultrafast Intersystem Crossing in 2-Nitronaphthalene. *Chem. Eur. J.*, **24**, 5379-5387 (2018).
2017	5. J. P. Zobel, J. J. Nogueira and L. González: The IPEA Dilemma in CASPT2. *Chem. Sci.*, **8**, 1482–1499 (2017).
2015	4. J. P. Zobel, J. J. Nogueira and L. González: Quenching of Charge Transfer in Nitrobenzene Induced by Nuclear Motion. *J. Phys. Chem. Lett.*, **6**, 3006–3001 (2015).
2014	3. J. P. Zobel, N. V. Kryzhevoi, and M. Pernpointner: Communication: Electron Transfer Mediated Decay Enabled by Spin-Orbit Interaction in Small Krypton/Xenon Clusters. *J. Chem. Phys.*, **140**, 161103 (2014).
2012	2. M. Pernpointner, J. P. Zobel, E. Faßhauer, and A. N. Sil: Spin-Orbit Effects, Electronic Decay and Breakdown Phenomena in the Photoelectron Spectra of Iodomethane. *Chem. Phys.*, **407**, 39-45 (2012)
	1. M. Pernpointner, J. P. Zobel, and N. V. Kryzhevoi: Strong Configuration Interaction in the Double Ionization Spectra of Noble Gases Studied by the Relativistic Propagator Method. *Phys. Rev. A*, **85**, 012505 (2012).

Teaching Experience

2017	Laboratory course on "Theoretical Chemistry"/Computer exercises (by C. Schröder, University of Vienna)
2016	Tutorial for lecture course "Theoretical Chemistry" (by L. González, University of Vienna).
2013	Tutorial for lecture course "Theoretical Chemistry" (by M. Pernpointner, University of Heidelberg).

Conferences & Workshops

2017	13. 11th Triennial Congress of the World Association of Theoretical and Computational Chemists, August 27-September 1, 2017, in Munich, Germany. Poster: It's Getting Hot: Temperature-Dependent Wigner Sampling and Excited-State Dynamics of 2-Nitronaphthalene.
	12. 67th Lindau Nobel Laureate Meeting, June 25-30, 2017, in Lindau, Germany. Attendance.
2016	11. SHARC Workshop, October 3-7, 2016, in Vienna, Austria. Attendence.
	10. CiQUS Seminar, September 7, 2016, in Santiago de Compostela, Spain. Talk: Effects of Vibrational Motion on the Excited States of Nitrobenzene.
	9. Gordon Research Seminar & Gordon Research Conference on Molecular Interactions and Dynamics, July 9-15, 2016, in Easton, USA. Poster: Nuclear Motion Affects Charge Transfer in Excited Nitrobenzene.
	8. 8th Molecular Quantum Mechanics Conference, June 26-July 1, 2016, in Uppsala, Sweden. Poster: The IPEA Dilemma in CASPT2.
	7. 4th MOLCAS Developers' Workshop, March 30-April 1, 2016 in Vienna, Austria. Scientific Report: CASPT2 – The IPEA Dilemma.
2015	6. 4th Workshop on Theoretical Chemistry and Computational Modeling (TCCM), October 5-6, 2015 in Madrid, Spain. Oral Communication: Effects of Vibrational Motion on the Excited States of Nitrobenzene
	5. 51st Symposium on Theoretical Chemistry 2015 (STC2015), September 20-24, 2015 in Potsdam, Germany. Poster: Quenching of Charge Transfer in Nitrobenzene Induced by Nuclear Motion.
	4. EMTCCM/XLIC School on Molecular Excited States, March 9-13, 2015 in Zaragoza, Spain. Attendance.
	3. CECAM Tutorial on Hybrid Quantum Mechanics / Molecular Mechanics (QM/MM) Approaches to Biochemistry and Beyond, February 9-13, 2015 in Lausanne, Switzerland. Attendance.
2014	2. 50th Symposium on Theoretical Chemistry 2014 (STC2014), September 14-18, 2014 in Vienna, Austria. Co-organization. Poster: The Effects of Solvation on the Absorption Spectrum and Excited Charge-Transfer State of Nitrobenzene.
2013	1. Excited States and Complex Environments (ESCE) Conference, October 8-11, 2013 in Münster, Germany. Poster: Calculation of Electronic Excitations Using the Relativistic Polarization Propagator.

Language Skills

German	Mother tongue
English	Fluently
Spanish	Basic

References

- Univ-Prof. Dr. Leticia González
  Institute of Theoretical Chemistry, University of Vienna
  Währinger Straße, A-1090 Vienna, Austria
  Phone: +43-1-4277-52750
  E-mail: leticia.gonzalez@univie.ac.at
- PD Dr. Markus Pernpointner
  Institute of Physical Chemistry, University of Heidelberg
  Im Neuenheimer Feld 229, D-69120 Heidelberg, Germany
  Phone: +49 6221 54 52 08
  E-mail: markus.pernpointner@pci.uni-heidelberg.de